Small Particle Transport in Fibrin Gels and High Throughput Clot Characterization

by
Richard Chasen Spero

A dissertation submitted to the faculty of the University of North Carolina at Chapel Hill in partial fulfillment of the requirements for the degree of Doctor of Philosophy in the Department of Physics and Astronomy.

Chapel Hill
2010

Approved by:

Richard Superfine, Advisor

Michael R. Falvo, Reader

M. Gregory Forest, Reader

Leandra Vicci, Reader

Sean Washburn, Reader

Alisa S. Wolberg, Reader

This dissertation is dedicated to my father
without whom I certainly would
not have pursued this degree,
for better or worse.

It could have been, I am sure, much worse.

ABSTRACT

RICHARD CHASEN SPERO: Small Particle Transport in Fibrin Gels
and
High Throughput Clot Characterization.
(Under the direction of Richard Superfine.)

The formation, function, and lysis of blood clots is largely governed by the transport of nano- and micro-scale particles. Yet there is not fully established physics that relates clot structure to transport phenomena such as fluid permeation and particle diffusion. This dissertation explores small particle transport in fibrin. I report on the size-dependence of particle mobility in fibrin, and discuss the implications of these results for fibrinolytic drug design. I measure the relationship between fibrin permeability and diffusion of 0.2–2.8 micron particles in fibrin gels, then determine the time and length scales at which small particle diffusion is directly related to bulk gel permeability. This result implies that one could develop a high throughput clot characterization assay that provides more detail than turbidity, the predominant high throughput measurement. I also present my work designing and developing systems to perform these and other experiments in high throughput, which include novel technologies for optical microscopy and magnetic force application.

ACKNOWLEDGMENTS

Graduate work is professional training, so my thanks are due first to the trainers. In particular, Rich Superfine, Leandra Vicci, and Russ Taylor have packed the last five years with endless lessons—intentional and accidental, direct and indirect—in the proper conduct and professional execution of science, engineering, and management. I have learned a broader swath of these arts over these years than I can imagine having equaled by any other endeavor, and for that privilege I am most grateful.

Graduate study is work, and other hands' fingerprints cover too much in this dissertation to thank them all here; I have noted their contributions throughout the text. But I must thank especially the relentlessly productive David Bober and the endlessly resilient Rachel Sircar, both of whom were always paddling whether or not I had my senses at the till. There is also NSRG's Matlab master, the goop king Jeremy Cribb, whose handiwork was never far below the surface of mine, and on whose shoulders I have spent much of my time attempting to perch.

Then there is what graduate school was not: it was not more than the hours I spent at it, not more than the education and opportunities and friends I gained, not my whole life. That is the purview of my best friend, my wife, my best reason for doing anything worth doing. Julie, I love you.

Contents

List of Figures

Chapter 1

Introduction

The formation, function, and lysis of blood clots is largely governed by the transport of nano- and micro-scale particles. A physiological clot's environment includes blood, pathogens, cells, and drugs, which move through a fibrin scaffolding by various mechanisms, including diffusion, advection, and active motility. The nature of clot formation and lysis is a product of clot structure, fluid permeation, and particle transport. Yet the physics relating these transport phenomena are not well understood. It is not known, for example, what physical theory governs the diffusion of a small particle through a clot, nor how that diffusion might be related to the bulk permeability of the material. This dissertation will address these issues by determining the timescale- and size-dependence of micro- and nano-particle diffusion in clots.

This work also has a context in soft matter physics. A wide range of scientists and engineers studying everything from biological tissues to novel materials to gas filters are concerned simultaneously with fluid permeation and particle transport through a medium. This dissertation evaluates when permeation and particle diffusion are quantitatively related. I show that the timescale of the diffusion measurement is critical in establishing this relationship, and thereby explain why prior work attempting to verify the effective medium theory showed poor agreement with experiment. Validating the effective medium theory establishes fibrin as a useful model material for studying particle diffusion over specific time- and length-scale regimes that are difficult to measure in other materials.

Like most of biology, coagulation is a phenomenon of many input parameters, including fibrinogen and thrombin concentration, calcium concentration, ionic strength, pH, crowding agent concentrations, and genotype. With the advent of siRNA libraries, one can imagine triggering clotting over a cell culture substrate, systematically knocking down each of the more than 21,000 human genes to see whether clot structure above the substrate is affected. Such an experiment would provide an unprecedented panorama of the genes involved in thrombin generation. Unfortunately, assays that provide detailed characterization of clots are typically low-throughput and labor-intensive. The techniques of this dissertation promise to provide high throughput characterization of clot structure, fluid permeation, and particle transport. I report on high throughput instrumentation that I have designed and developed to enable my experiments. These systems include an automated microscope built with components that may be tiled up to 12 times below a conventional microplate, and a multiforce high throughput system (MHTS) for force application in biophysical experiments. In this dissertation I report on the design and qualification of these technologies.

This high throughput technology has applications that range far beyond clot characterization. High throughput screening is increasingly critical in cell microscopy, but existing systems suffer from slow 3D imaging, low-bandwidth in time-lapse experiments, and incompatibility with force application or other mechanical measurements. The high throughput technology I present in this dissertation addresses these issues.

1.1 Coagulation and Transport

Fibrin is the polymer scaffolding of a blood clot (Weisel, 2005). Damage to the vascular endothelium[1] reveals tissue factor, which triggers a cascade of reactions culminating in the conversion of prothrombin to thrombin. Thrombin activates fibrinogen, a 340kDa glycoprotein that is always present in healthy blood. An activated fibrinogen molecule is called a fibrin monomer, which in sufficient concentration self-assembles into a fibrous gel. Physiologically, fibrin gels nucleate from activated platelets or the endothelium, ultimately sealing vascular breaches and restoring haemostasis. Clots are broken down when tissue Plasminogen activator (tPA) converts plasminogen—another protein endemic to blood—to plasmin, the factor that begins fibrinolysis (fibrin digestion) and therefore limits clot lifetime within the vasculature.

When it functions properly, therefore, clotting is essential to health. Yet because pathological clotting is the central risk of cardiovascular disease, it is also the top contributor to the global burden of disease (WHO, 2004), whether through an occlusive thrombus[2] triggering myocardial infarction[3], or a deep vein thrombus that dislodges

---

[1] vascular endothelium: the cells of the blood vessel wall

[2] thrombus: clot formation within the vasculature

[3] mycardial infarction: heart attack

and results in pulmonary embolism[4]. These conditions arise from unwanted clotting; failure to clot is similarly dangerous, as in hemophilia (Rodriguez-Merchan et al., 2000).

One might separate the requirements for clotting—both hemostatic (good) and pathological (bad)—into the biochemical and the physical. The biochemical requirement is simply that to achieve coagulation there must be thrombin to activate fibrinogen, and that for lysis there must be plasmin to cleave fibrin. Hemophilia is an example of a clotting pathology that is biochemical: this genetic disorder results in low expression of Factors VIII or IX, both of which are involved in thrombin generation.

The physical requirement is that the factors must be at the sample location for sufficient time to allow the reactions to occur. For example, thrombin is created when freely circulating prothrombin is activated, near cells or platelets, by a complex of factors Va and Xa. To achieve clotting, therefore, fibrinogen must come to these locations, or thrombin must move away from them. Not surprisingly, then, the geometry of thrombin generation has an impact on gel structure (Wolberg and Campbell, 2008). Similarly, to achieve clot lysis, plasminogen must encounter tPA to become plasmin, and must then destroy the clot from the outside in, or travel into it; hence, the ability of a clot to allow transport has an effect on the time required to dismantle it (Veklich et al., 1998). Heart disease has been correlated to tight and rigid clots (Fatah et al., 1996), so clot geometry is intimately tied with the difficulty in treating patients suffering myocardial infarction due to thrombosis.

The physics of clotting includes kinetic considerations. The faster blood flows,

---

[4] pulmonary embolism: a thrombus that breaks free from a vessel wall and lodges in the lung

the less conducive the environment is to clotting. This is demonstrated at formation, where poor circulation is a risk factor for deep vein thrombosis, and at lysis, where forced perfusion is a common (and painful) treatment (Wicky, 2009). This treatment is used because increasing gel perfusion accelerates clot destruction (Diamond and Anand, 1993).

The coincidence of clotting agents and the time that they have to interact are determined by transport of blood and the biochemical factors therein. Transport is therefore a key issue in clotting pathology and treatment, including transport of coagulation factors, which must be present only in the locations where clotting is desired, and also transport of blood itself, which must stay contained, yet circulate freely, within the vasculature.

1.1.1 Studying clot transport

Clot transport *in vivo* is the product of five (often simultaneous) phenomena: diffusion, advection, steric hinderance, hydrodynamics, and chemical interaction. All objects in solution are subject to thermal diffusion, the random motion of particles due to the non-zero net impulse of many random collisions with solvent molecules. Because blood is pumped by the heart, objects in clots also experience advection, the transport of a particle being carried by local solvent flow. The presence of solid barriers, including the endothelium and the fibrin mesh, hinder objects' transport by steric interaction, the physical exclusion of a particle from space filled with other solid matter. These solid barriers place boundary conditions on the solvent, so objects may experience an altered hydrodynamic environment. Finally, fibrin is not chemically inert, so objects stick to the clot scaffolding, suppressing their transport. With enzymes that affect clot structure—namely thrombin and plasmin—chemical interaction feeds back into the other transport mechanisms, as formation or destruction of the clot may affect the conditions that determine diffusion, flow, or collisions.

These are the relevant mechanisms determining transport in clots. However, they are not always the properties measured in studies of clot formation, function, and lysis. Today, research of transport in clots typically involves at least one measurement among permeation, imaging, or turbidity. Permeability is an explicit metric of hemostasis and of fluid transport through the clot, and it has been correlated with diabetes (Dunn et al., 2005) and heart disease (Fatah et al., 1992; Fatah et al., 1996). Permeability is blind to microscopic details of particle transport, and is a low-throughput technique. Yet the physiological relevance of the measurement cannot be ignored, so a permeability assay that could reveal microscopic aspects of clot structure and scale to high throughput format would be an important contribution to the field. I show in Chapter 3 that at the appropriate time and length scales, nanoparticle diffusion can serve as this assay.

Imaging—primarily confocal and electron microscopy—has been used to measure clots' formation and microscopic structure (Blombäck et al., 1994; Blombäck et al., 1989). Microscopy makes no explicit transport measurement, although recent efforts have extracted clot porosity from clot images (Collet et al., 2003; Mickel et al., 2008), which in turn may help predict transport. The more commonly calculated parameters (branchpoint density, fiber length, and diameter) are notoriously labor-intensive to extract, and imaging techniques have inherent errors in measuring fiber size. This begs the question of whether a non-imaging measurement could provide implicit structural information about the gel. Based on theories that I introduce in Chapter 2, I show in Chapter 3 that a combination of permeability and diffusion measurements can provide quantitative insight into the structure of fibrous gels.

Turbidity, a measurement of bulk optical transmission, is of particular interest because it is inexpensive, can be performed in high throughput (Wolberg et al., 2002), and is used as an indirect measurement of fiber diameter and fiber protein density (Carr and Hermans, 1978). Turbidity probes bulk-averaged structure of the clot, so one might imagine that it would be sufficient to predict bulk-averaged resistance to fluid flow (permeability). Indeed, experts in the field have developed a rich intuition for interpreting turbidity curves. However, as I explain in Section 2.3.4, turbidity cannot be used to predict gel permeability.

Of these three methods, none offers direct measurement of particle transport in clots. Given the relevance of particle transport to clot formation and lysis, such an assay would be of scientific, and potentially clinical, value. A particle transport assay's usefulness would be determined by (1) its sensitivity to relevant clot properties, (2) a known relationship to the other commonly studied parameters of permeability, imaging, and turbidity, and (3) instrumentation that is well qualified to be deployed and used outside of our research group. In this work, I present a diffusion-based clot assay and address all three of these considerations.

1.2 Scope of this Research

The prior work discussed above has highlighted conditions where diffusion is a key phenomenon in clot formation and lysis, including the impact of thrombin concentration gradients on clot structure and the speed of clot lysis on permeant velocity. But the actual behavior of diffusing particles in clots is not well established, beyond the fact that particle surface chemistry affects mobility (Valentine et al., 2004) and that fiber stiffness can be measured by diffusion of stuck particles (Jahnel et al., 2008). It has not been established how a particle's diffusion scales with its size.

More broadly, the work reviewed in Section 1.1 has highlighted the involvement of specific transport phenomena, but it has not explored their governing physics. Without identifying the relevant theory, predictive models of clot formation, haemostasis, and lysis will remain elusive. These models would help clarify clot biology, and could potentially assist in designing drugs, stents, and other biomedical devices.

From a physical perspective, fibrin also provides a model system for understanding physical properties of highly elastic, low volume fraction, fibrous media. Specifically, it is unknown whether the bulk properties of fibrin gel relate to micro-scale properties, including whether the behavior of micron-sized probes carries information about the bulk viscoelasticity of the gel, about its bulk permeability, or about its structure.

This dissertation addresses these questions. In Chapter 3 I report on experiments with passively diffusing nano-particles. Particle diffusion in fibrin is indeed dependent on particle size, and the timescale over which the particle diffuses. I focus on the hundreds-of-nm regime, using 500 nm particles for many experiments, and ranging in size from 200 nm to 2.8 μm. The 500 nm particles are half to a tenth the size of platelets or cells that might perfuse a clot; they are ten to 100 times the size of ambient proteins or drugs. Comparing directly with these physiological agents is not necessarily fruitful—platelets, cells, enzymes, and drugs can all interact biochemically with fibrin. However, chemically inert probes at this length scale are in a physically intriguing regime: they are small enough to diffuse through the fibrin matrix, but big enough that they seem likely to collide with it. I show the sensitivity of particle transport to particle size, and based on these results I propose a drug design to maximize lysis of occlusive thrombi while minimizing the risk of hemorrhage.

In Chapter 3 I also demonstrate that at short timescales ($\tau < 1$ s), and for small ($d \leq 500$ nm), chemically inert particles, diffusion and permeability are intimately related, and that one can actually predict the other through the effective medium theory. I explain that therefore hydrodynamic, rather than steric, effects dominate diffusion at the micro-scale. Larger particles are more likely to become lodged in the gel, and 1 μm particles are found to always be stuck. At longer timescales, I report on evidence that steric effects may be affecting particle diffusion.

Chapter 3 answers questions about the nature of stuck particles. In Chapter 4 I show that micron-scale particles in fibrin—which do not freely diffusion—are not strongly adhered to the gel. By applying forces on the order of those found in arterial flow, micron-scale particles will move long distances (> 100 μm), suggesting that such particles may be useful as drug delivery vectors for fibrinolytic treatments. In addition, I show that for particles at least 2.8 μm and smaller, driven micro-rheology measures a local mechanical property of the clot, rather than the bulk viscoelastic properties of the gel, and that it can measure time-dependent stiffening of fibrin during clot formation.

In addition to my scientific work focused on fibrin and other fibrous gels, I have helped to design, build, and qualify systems for high throughput microscopy, manipulation, and rheology that are designed to address the needs of these and other experiments. They are core technologies for a microrheology and cell screening system that is presently under development. These systems and my contributions to their realization are the subject of Chapter 5.

Chapter 2

Transport in Fibrin: Theory

When particles move in clots, what phenomena are at play? The physical environment for diffusing particles, and the fluidic environment during permeation, are not well understood in clots. In this Chapter, I begin with the impact a gel is expected to have on a diffusing particle and on a permeating fluid. The presence of a gel will impose boundary conditions on the fluid, as well as on the particle motion. I determine the relevant length and timescales for these effects.

In the remainder of this Chapter I explore the relationship of gel structure to transport. Imaging has been used to extract gel structure, including fiber density (Campbell et al., 2008), branchpoint density (Ryan et al., 1999), and gel porosity (Mickel et al., 2008). However, this information has not been used to test the quantitative theories that use these structural parameters to predict particle diffusion or fluid permeation. Therefore, I will spend some pages looking in detail at the theoretical relationships among structure, permeation, and particle transport. The goal of this Chapter is to clarify what theories exist, which might be relevant in fibrin modeling, and how using one theory might help validate or invalidate the applicability of others.

2.1 Expectations for particle motion in fibrin

2.1.1 Single Particle Diffusion

In classical physics, diffusion was understood through the lens of Fick's laws, which described the phenomenon in terms of concentration gradients (Cussler, 1997). It was Einstein who provided the physical explanation for single particle diffusion (Einstein, 1905), often called Brownian motion. This explanation is captured in the Stokes-Einstein relation, which states that for a sphere of diameter d in a fluid of viscosity η,

$$D = \frac{k_\mathrm{B}T}{f} = \frac{k_\mathrm{B}T}{3\pi\eta d}, \tag{2.1}$$

where k_B and T are Boltzmann's constant and absolute temperature, respectively. D is the diffusion coefficient of the material. For aspherical solutes, the denominator f may be replaced by the Stokes drag formula (Happel and Brenner, 1983) for that geometry. Einstein noted that D determines the time-averaged position of the particle

$$\langle r^2 \rangle = 4D\tau, \tag{2.2}$$

where $\langle r^2 \rangle$ is mean squared displacement, and τ is the time between position measurements during which the particle diffuses. Einstein also explained that the D of Equation 2.1 can explain the bulk diffusion of Fick's Laws, provided that material is homogeneous and invariant in time.

While for many natural and engineered systems homogeneity and stasis are appropriate assumptions, for biological systems it is rarely appropriate to apply either. First, polymers are typically viscoelastic—namely, under stress they exhibit frequency-dependent frictional loss and elastic energy storage (Ferry, 1980). Polymer solutions are spatially heterogeneous on certain length scales, and the interaction of polymer chains with suspended particles depends on the size of the particles, the physical parameters of the chain (chain length and flexibility), and the nature of the solution (the quality of the solvent and the concentration of polymer) (Rubinstein and Colby, 2003). Biological materials can be even more heterogeneous; for example, mucus comprises pathogens and particulates suspended amidst a solution of polydisperse mucins (Thornton et al., 2008). Fibrin is viscoelastic (Roberts et al., 1974); it also exhibits temporal heterogeneity during clot formation and lysis, and spatial heterogeneity on length scales at or below the mesh size of the gel.

Measurements of single-particle diffusion, made possible by advances in microscopy and single-particle tracking, reveal some of these complexities. In homogenous but viscoelastic materials, it has been observed that diffusion of particles is suppressed on certain timescales such that

$$\langle r^2 \rangle \propto \tau^\alpha \tag{2.3}$$

where $0 < \alpha < 1$ (Wong et al., 2004). The powerlaw α may not be constant over all timescales. However, for any range of τ over which $\alpha = 1$, the average motion is Brownian. (There are instances where the average motion is Brownian but the step size distribution is non-gaussian (Wang et al., 2009); in this dissertation, I have seen no evidence of such an effect.) In such cases it is useful to generalize Equation 2.2 by taking $D \rightarrow D_{\text{eff}}$, with the "effective" subscript capturing the concept that the material appears purely viscous, although no aspect of the particle-polymer-solvent system can be said truly to have a viscosity corresponding to D_{eff}.

For homogeneous media, variations in α can be explained as the result of frequency-dependent elastic storage and viscous losses. Mason and Weitz have explained that the complex modulus $G^*(\omega)$ of a bulk material may therefore be extracted from $r(t)$ (Mason and Weitz, 1995). This approach has since become a key technique in the larger field of microrheology (Waigh, 2005; Cicuta and Donald, 2007; Kimura, 2009).

Fibrin, however, is not homogeneous on the micron length scale. Therefore, much of microrheology is not expected to be relevant in this material. To develop a sound model of transport, we need to be clear about valid assumptions one can make about the gel.

2.1.2 Assumptions for fibrin modeling

The coagulation community has a language for describing fibrin gel phenotypes. Clots are often described as coarse (few thick fibers, low volume fraction) or fine (many thin fibers, high volume fraction), but the terms are not always clearly defined. I have summarized the definition of these qualitative terms in Figure 2.1.

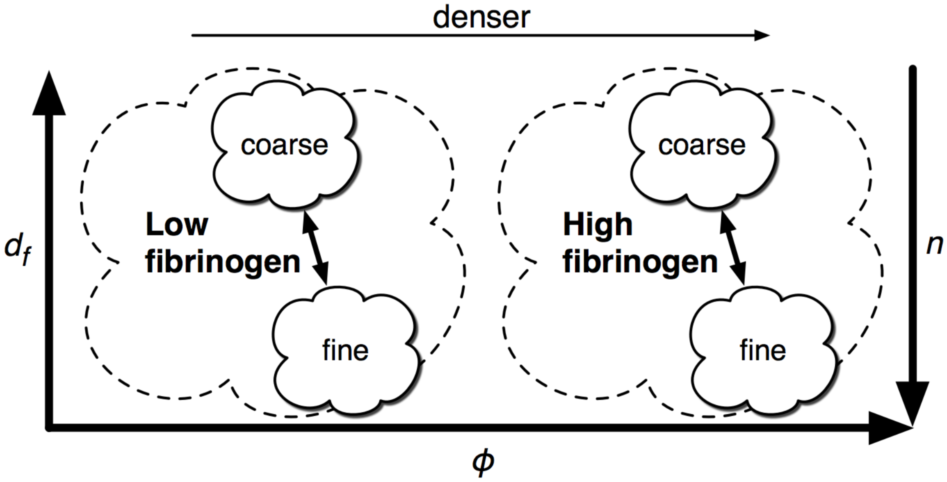

Figure 2.1: Clots at a given fibrinogen concentration have a range of phenotypes, from "fine" to "coarse," depending on the polymerization conditions. This cartoon defines these terms relative to the physical parameters of fiber diameter (d_f) and volume fraction (ϕ), which are useful in quantitatively describing clot structure. For a clot of fixed fibrinogen concentration, a clot becomes finer when the same fibrin is distributed over more fibers, increasing fiber number density n but decreasing d_f. To first order, volume fraction ϕ should remain the same, but there are indications that thicker fibers pack fibrinogen more densely than thin fibers (Guthold et al., 2007), meaning volume fraction would also increase as clots become finer. Clot coarseness is typically inversely proportional to polymerization rate—for example, high thrombin concentration leads to finer clots. Clot density increases with rising fibrinogen concentration.

Platelet-poor plasma (PPP) and purified fibrin clots are fibrous gels. The material is heterogenous on the nanometer-to-micron length scale, as is clear from the microscopy of Figure 2.2, which shows representative images of all the clot types studied in the present work. In the absence of external stress, the fiber segments are straight and can be considered rigid rods, as recent work has identified the persistence length l_p of fibrin fibers in a clot to be $\sim$ 10 cm (Jahnel et al., 2008).

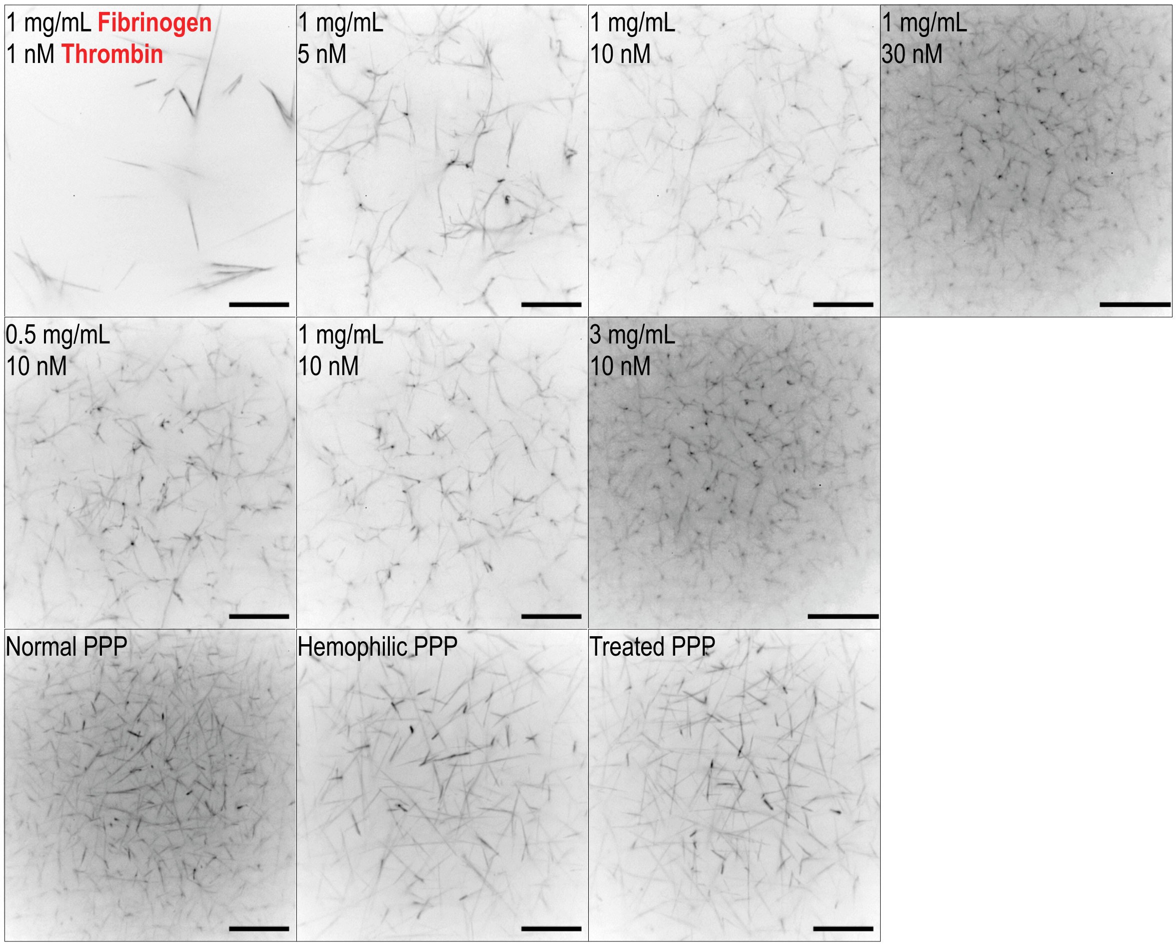

Figure 2.2: Confocal microscopy of the clot types studied in this work. As has been well established in prior work, clot coarseness decreases with thrombin concentration (first row) and fibrinogen concentration (middle row). Platelet-poor plasma (PPP) clot structure also varies with pathology. In this case, hemophilic clots are coarser than normal clots, and rFVII can restore some of the lost density (last row). Scale bar is 20 μm

On the second to week-long timescales, the gel may be considered invariant in time. After gel formation, and in the absence of any fibrinolytic agent, fibrin structure apparently does not change unless dehydration or contaminating bacteria damage the scaffolding. On minute and second timescales, the gel does not move under confocal microscopy. From day to day, confocal images of the gel do not change in any discernible way.

In fibrin networks there is little space that actually contains fibrin, a quality captured in the gel's volume fraction, ϕ. For compacted clots, the densest of the physiological gels, $\phi < 0.25$, while for non-compacted clots, including arterial thrombi, $\phi < 0.1$ (Diamond, 1999). Clots can be coarse, with few thick ($\sim$ 500 nm) fibers separated by large ($\sim$ 20 μm) distances, or fine, with many thin ($\sim$ 100 nm) fibers separated by short ($\sim$ 1 μm) distances. Figure 2.2 indicates that the distance between fibers can be $\sim 0.1 - 10\mu$m.

In spite of this open space, non-specific chemical adhesion of probes to fibrin prevents long-distance transport of even nanometer-scale probes. Fibrin is notoriously sticky. It is used as a tissue adhesive (Saxena et al., 2003), and shows non-specific adhesion to everything from pipette tips to nanoparticles with carboxylate surface chemistry. Polyethylene glycol (PEG) has been used to reduce, but not eliminate, the likelihood of nanoparticle adhesion to fibrin (Valentine et al., 2004). Particles (including enzymes and drugs) diffusing in a physiological clot typically would interact chemically with fibrin; free diffusion of chemically active particles could be modeled as an equilibrium between binding and unbinding events. In addition, enzymes such as thrombin and plasmin are known alter the gel's structure. In order to focus on the physical interactions at play in nanoparticle diffusion, this dissertation will focus on the motion of PEG-coated probes that neither stick to nor alter the gel.

In summary, for a static flow environment we can reasonably model fibrin as a random array of rigid rods. This allows me to provide some estimate of how a diffusing particle will interact with the gel.

2.1.3 Steric diffusion suppression

I will begin with steric interactions. These events occur when the diffusing particle "bumps" into the gel. How often will this occur? More precisely, how long will we have to watch a diffusing particle before it collides with a fiber?

Consider a diffusing particle and the nearest fiber, shown in Figure 2.3. We can ignore all but the nearest fiber because when the bead does collide with a fiber it will, by definition, be the closest fiber. If the fiber is a distance R from the particle, then the time required to travel the distance to the fiber is simply the first passage time in 3-space,

$$\tau_R = \frac{R^2}{6D_{\text{eff}}}, \tag{2.4}$$

where I have used the generalized diffusion coefficient D_{eff}, because the particle's diffusion will be determined not by the bulk diffusion from Fick's laws, but by the viscosity of fluid in which the particle is diffusing. However, we certainly do not expect that the particle will always diffuse toward the fiber; in fact, it will diffuse randomly to the edge of a shell with radius R. After diffusing for a time τ_R, the probability P_R that the particle will collide with the fiber is the fraction of the shell's surface occupied by the nearest patch of fiber,

$$P_R = \frac{d_f^2}{4\pi R^2}, \tag{2.5}$$

where d_f is the fiber diameter. If, after τ_R, the particle has not hit a fiber, then it will have another shot during the following τ_R. The probability that it will hit a fiber after n attempts is unity minus the probability that it never hits, or

$$P_n = 1 - (1 - P_R)^n = 1 - (1 - P_R)^{\tau/\tau_R} \tag{2.6}$$

$$= 1 - \left(1 - \frac{d_f^2}{4\pi R^2}\right)^{\frac{6\tau D_{\text{eff}}}{R^2}} = P(\tau), \tag{2.7}$$

recognizing that the number of attempts $n = \tau/\tau_R$.

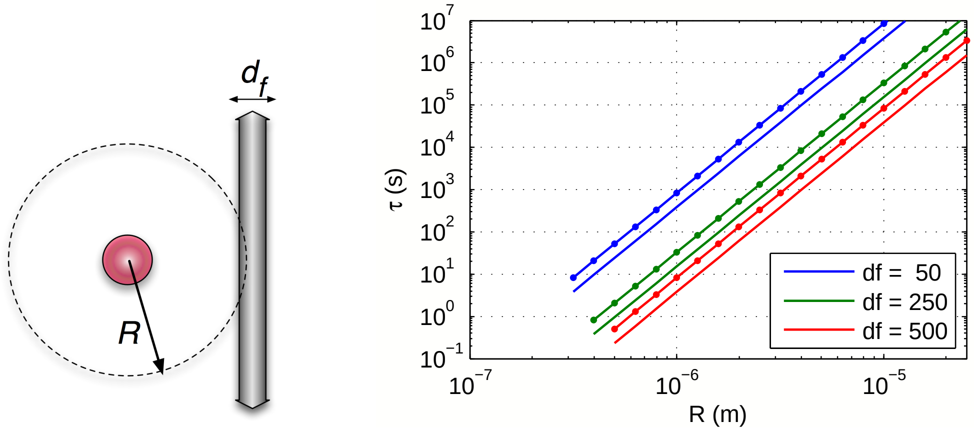

Figure 2.3: Left: A cartoon of the steric diffusion problem. Right: The startup τ (plain lines) and steric τ (dot-lines) for clots of three fiber diameters (d_f = 50, 250, and 500 nm). The collision probability P was calculated from Equation 2.7 for a 500 nm particle in water, and plotted against the average distance to the fibers R. The lines truncate at the left because the separation between the particle and the fiber $R - {}^{(d_f + d)}/_{2} \leq 0$. Typically, $d_f \sim$ 100–250 nm and $R \sim$ 0.5–5 μm, though extreme conditions may place clots out of this range.

Solving for τ gives the time required to see a collision with probability P:

$$\tau(P) = \frac{R^2}{6D_{\text{eff}}} \, \frac{ln(l-P)}{ln(1-\frac{d_f^2}{4\pi R^2})}$$

To estimate the timescale over which a collision will occur, I can solve Equation 2.7 for $P = {}^{1}\!/_{e}$ and $1 - {}^{1}\!/_{e}$,

$$\tau_{\text{steric}} = \frac{-1}{\ln(1-\frac{d_f^2}{4\pi R^2})} \frac{R^2}{6D_{\text{eff}}} \tag{2.8}$$

$$\tau_{\text{startup}} = 0.46 \; \tau_{\text{steric}}. \tag{2.9}$$

I will call these cases the "startup τ" and the "steric τ", because these are the timescales at which a steric effect will begin to manifest, and when it will consistently contribute, respectively.

For 500 nm particles, then, the startup and steric τ are plotted in Figure 2.3 as a function of nearest average distance to a fiber R, for several fiber diameters, d_f. The plot reveals several key elements of steric diffusion suppression. First, the steric τ is a very steep function of R, so small changes in clot density are likely to have a dramatic impact on whether steric diffusion suppression occurs. Second, the transition region—the difference between the startup τ and steric τ—is not large; it is apparently less than a decade. Finally, in all but the most dense clots—say, $R < 600$ nm and $d_f > 250$ nm—steric effects should not be expected to manifest on timescales $\tau < 1$ s.

2.1.4 Hydrodynamic diffusion suppression

How far must a particle be from a fiber before it starts to feel diffusion suppression? Specifically, how does the drag on a particle increase as it approaches the fiber boundary? The ideal toy problem to address this question would be a solution for the Stokes drag on a particle near a cylindrical boundary. The case of a particle inside a cylinder has been addressed (Happel and Brenner, 1983; Lee and Ladd, 2005), but I am not aware of a solution for the rod-sphere case[1]. However, the bracketing cases of a particle near a plane and a sphere have been treated; these provide a lower and upper bound, respectively, on the expected diffusion coefficient for a particle near a cylinder. The geometry of these cases is summarized in Figure 2.4.

It has been verified experimentally (Kihm et al., 2004; Choi et al., 2007) that a sphere diffusing near a plane shows hindered diffusion, such that

$$\begin{aligned}
D_{\text{wall}} &= \lambda_{\text{wall}} D_0 = D_0 \frac{2\lambda_{||} + \lambda_{\perp}}{3} \\
\lambda_{||} &= 1 - \frac{9}{16}\frac{d}{2z} + \frac{1}{8}\left(\frac{d}{2z}\right)^3 - \frac{45}{256}\left(\frac{d}{2z}\right)^4 - \frac{1}{16}\left(\frac{d}{2z}\right)^5 \\
\lambda_{\perp} &= \left(\frac{4}{3}\sinh\alpha \sum_{n=1}^{\infty} \frac{n(n+1)}{(2n-1)(2n+3)}\left[\frac{2\sinh\beta\alpha + \beta\sinh 2\alpha}{4\sinh^2\frac{\beta}{2}\alpha - \beta^2\sinh^2\alpha} - 1\right]\right)^{-1} \\
&\quad \text{where} \quad \alpha = \cosh^{-1}\frac{2z}{d} \text{ and } \beta = 2n+1. \qquad (2.10)
\end{aligned}$$

The two-sphere case has been treated for constant-velocity particles (Happel and Brenner, 1983), but the friction coefficient found there (Equation 6–3.51) applies equally

---

[1] I am indebted to Greg Forest, Peter Mucha, and Roberto Camassa for their help in the literature review

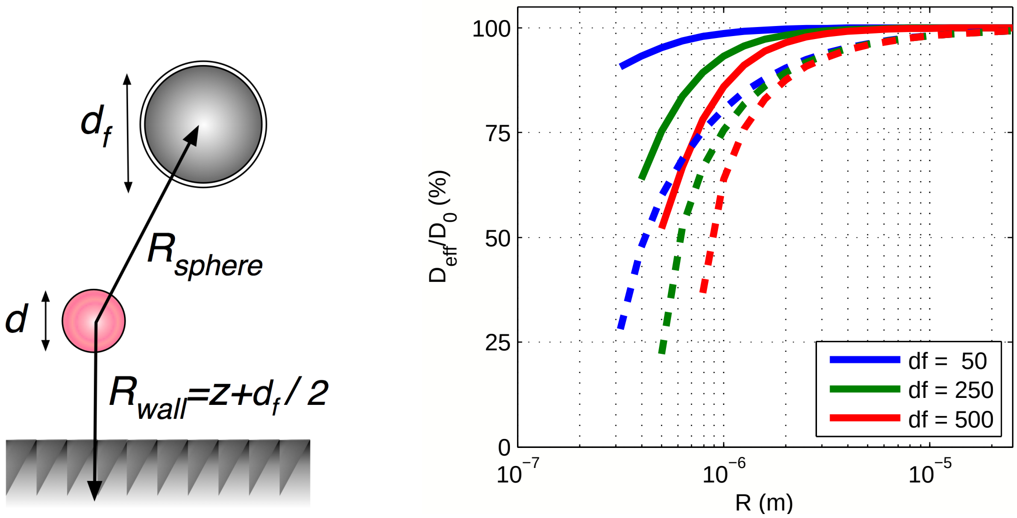

Figure 2.4: Left: Cartoon summarizing the terms used in the two-sphere and sphere-plane solutions for diffusion suppression. Right: Diffusion suppression of a 500 nm particle as a function of distance from a boundary, for three fiber diameters (d_f = 50, 250, and 500 nm). Plotted are $^{D_{\text{wall}}}/_{D_0}$ from Equation 2.10 (dashed lines) and $^{D_{\text{sphere}}}/_{D_0}$ from Equation 2.11 (solid lines). The lines truncate at the left because the separation between the particle and the boundary ($z \leq 0$ for the plane and $R - {}^{(d_f+d)}/_2 \leq 0$ for the sphere) goes to zero. Typically, $d_f \sim$ 100–250 nm and $R \sim$ 0.5–5 μm, though extreme conditions may place clots out of this range.

well in this case, because of the low Reynolds number assumptions. Setting the velocity of the second sphere to zero (recognizing that the fiber is static relative to the diffusing particle) and inserting d_f for the diameter of the second sphere, we find,

$$D_{\text{sphere}} = \lambda_{\text{sphere}} D_0 = \frac{D_0}{1 + \frac{9}{16}\frac{dd_f}{R^2} + \frac{3}{64}\left(3\frac{dd_f^3}{R^4} + \frac{27}{4}\frac{d^2d_f^2}{R^4} - 2\frac{d^3d_f}{R^4}\right)} \tag{2.11}$$

The relative suppression, $^{D_{\text{eff}}}/_{D_0}$, is plotted in Figure 2.4. As expected, the suppression from the particle-plane case is greater than that from the two-particle case; the particle-cylinder case should be somewhere in between these two cases. The absolute lowest bound is provided by the two-sphere case and the smallest d_f, 50 nm, which shows that at larger values of R—say, above 1 μm, little hydrodynamic effect should be visible. While this plot cannot truly predict the diffusion of particles in fibrin, it does suggest that some level of hydrodynamic diffusion suppression should be expected in most clots, for four reasons. First, the actual hydrodynamic effect will be more severe than the two-sphere case. Second, clots typically have fibers thicker than 50 nm. Third, even in clots where R can be very large—say, 10 μm—the particle will spend some time closer to the fibers, and the diffusion suppresses rapidly as the particle moves closer to the boundary. Fourth, the hydrodynamic effect—unlike the steric effect—is additive, meaning that every fiber contributes to the particle's friction coefficient, not just the nearest one.

One final comment on the hydrodynamic effect: while the amount of diffusion suppression a particle will experience changes as a function of the particle's position, it will manifest, on average, at *all* τ. This is in contrast to the steric effect, which will occur only at and above the timescale over which a particle travels from fiber to fiber. Therefore, on timescales $\tau < 1$ s I expect we will see only hydrodynamic diffusion suppression.

2.1.5 Expectations for data

Figure 2.5 shows what I expect my data to look like, when both the hydrodynamic and steric effects are taken together. The hydrodynamic effect occurs at all timescales, while the steric effect only manifests above the startup-τ.

The $\langle r^2 \rangle$ at which the steric effect begins to manifest must also provide some insight

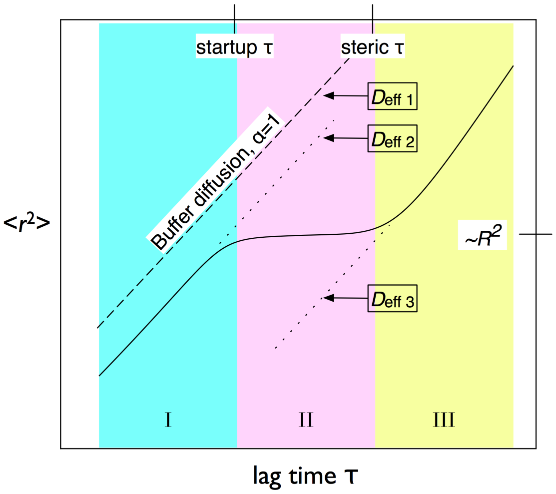

Figure 2.5: Cartoon of a theoretical $\langle r^2 \rangle$. The diffusion coefficient is defined for parts of the curve that have a slope $\alpha = 1$ (regions I and III). The higher the intercept of the line, the greater the diffusion coefficient. As discussed in Section 2.1, at short timescales (region I) the particle interacts only with the local fluid, but D_{eff} is lower than it would be in free buffer (dotted line) because of the presence of the gel. After a transition region (region II), steric effects begin to manifest at longer timescales (region III), resulting in a lower D_{eff} than at short timescales.

into the fiber density. Conceptually, the range of the $\langle r^2 \rangle$ at the startup and steric τ should be related to the distance to the nearest fiber $\langle r^2 \rangle \sim R^2$, as noted in Figure 2.5.

I have used arguments about the way diffusion is determined by gel structure to motivate Figure 2.5. Gel structure, however, determines more than just diffusion. It also determines gel permeability. A gel resists fluid flow because of friction between the fluid and fiber surfaces. These boundary conditions are precisely the ones responsible the hydrodynamic effect described in Section 2.1.4. Therefore, I hypothesize that if there is a relationship between gel permeability and particle diffusion, that it will exist only on timescales where the hydrodynamic effect solely determines D_{eff}, below the startup-τ, in region I of Figure 2.5.

2.2 Fibrin Structure and Particle Diffusion

We now have a broad picture of what physical phenomena govern particle diffusion in clots, and the timescales on which they are relevant. In this section I expand on the toy problems of Section 2.1 by highlighting specific models of particle motion in models of fibrous materials.

2.2.1 Ogston Model: diffusion with steric hinderance

Consider fibrin to be a simple porous network, invariant in time, with a rigid scaffolding submerged in a background fluid, in which solute particles can move. Ogston considered solute diffusion in a matrix of randomly oriented rods (Ogston et al., 1973). He presented a stochastic argument, closely following Einstein's 1905 approach. In Ogston's treatment, however, the presence of the rods sometimes prevent the particle from translating. The result is that the particle moves less:

$$\frac{D_{\text{eff}}}{D_0} = \exp\left[-\phi\frac{d}{d_f}\right] = e^{-\phi/\lambda}, \tag{2.12}$$

where D_0 is the diffusion coefficient of the particle in pure background fluid, ϕ is the volume fraction of the gel, and d_f is the diameter of the rods that form the matrix. The predicted quantity, D_{eff}, is the particle's actual diffusion coefficient, which the theory indicates will be below D_0 due to the presence of the gel; this is shown in Figure 2.6. Note that moving to coarser clots—increasing d_f at constant ϕ—*restores* the effective diffusion coefficient closer to D_0. This is because if the fibers get thicker while the volume fraction remains steady, then the number of fibers must be decreasing; this in turn, corresponds to an increase in the size of the open spaces (captured by the quantity R in Section 2.1).

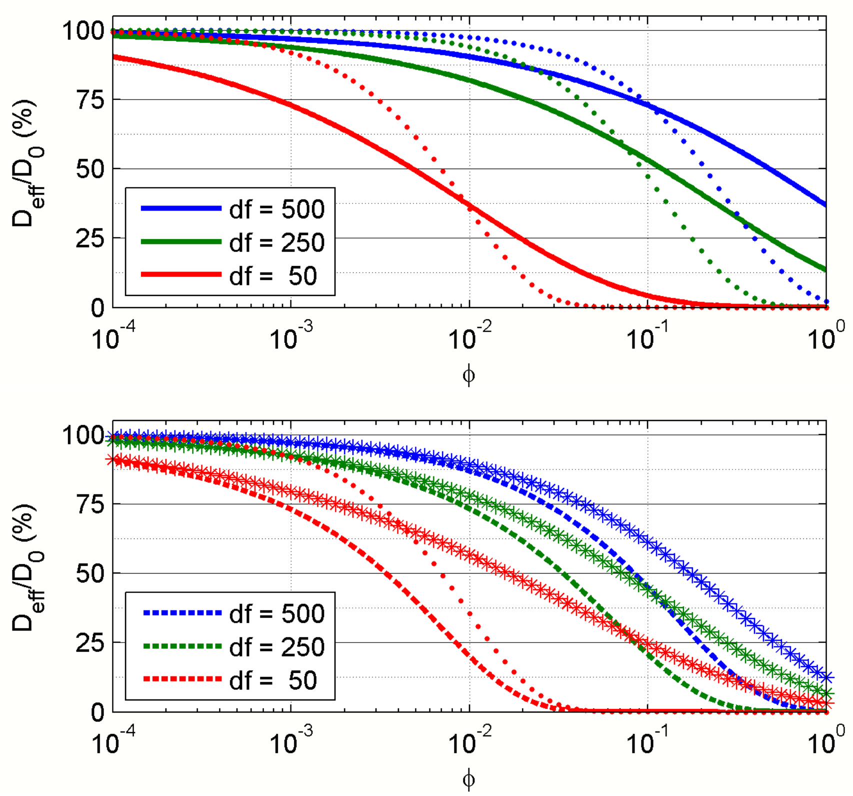

Figure 2.6: Two models of diffusion suppression for a 500 nm particle in a gel of varying fiber diameter ($d_f = 50$, 250, and 500 nm) as a function of volume fraction. The range $0.01 < \phi < 0.2$, is typical for fibrin gels. Top: The Ogston model (Equation 2.12) (solid line), plotted with the steric-only term of the Phillips Model $S(f)$ (dots). The numerical solution in $S(f)$ does not agree with the Ogston model, but the reason for the disagreement is not well-explained in the literature. Bottom: The Phillips Model (Equation 2.13) (dashed line), plotted with its hydrodynamic-only term F (stars). Also plotted is the $d_f = 50$ nm case for $S(f)$ (dots). Comparing $S(f)$ and F shows that at low volume fraction, the diffusion suppression is primarily hydrodynamic, but as the gel becomes more dense, the steric effect comes to dominate the supression.

At the time, Ogston showed that this theory explained experimental data of particle sedimentation in hyaluronic acid, in a system where $d/d_f \approx 1.4$. It has been revisited regularly—recently, see (Johnson et al., 1996; Williams et al., 1998)—but I am not aware of research testing its relevance in fibrin diffusion. The Ogston model accounts only for steric interactions, and ignores any hydrodynamic effect that the gel might have on the background fluid. Yet Figure 2.5 explains that we expect the hydrodynamic effect to be present at all timescales. In Chapter 3 I show that the Ogston Model is not consistent with my data, as expected.

2.2.2 Phillips Model: a numerical solution

More recently, Phillips provided a simple formulation for diffusion suppression that accounted for both hydrodynamic and steric interactions with the gel (Phillips, 2000). Phillips used his prior work simulating the hydrodynamic effect for particle diffusion in a liquid-filled, three-dimensional medium of randomly placed cylindrical fibers (Clague and Phillips, 1996), and combined it with the results of a simulation of the steric effect in rigid-strand polymer solutions (Johansson and Lofroth, 1993). The result is the relation

$$\begin{aligned}
\frac{D_{\text{eff}}}{D_0} &= FS(f) \\
F &= e^{-a\phi^b},\ S(f) = e^{-0.84f^{1.09}} \\
a &= 3.727 - 2.460\lambda + 0.822\lambda^2 \\
b &= 0.358 + 0.366\lambda - 0.0939\lambda^2
\end{aligned} \tag{2.13}$$

where F is a term that captures hydrodynamic diffusion suppression, $S(f)$ captures the steric diffusion suppression, $f = \phi(1 + \frac{1}{\lambda})^2$, and $\lambda = {}^{d_f}/_{d}$.

We can apply this model to fibrin diffusion data whether hydrodynamic or steric effects are responsible. As with the Ogston Model, the Phillips model has not been tested against diffusion and structural data from fibrin gels. Because of the inherent challenges of determining clot structure from microscopy, the validation of this theory in fibrin is outside the scope of this dissertation. However, in Section 3.3.1 I show that the Phillips model can be inverted, along with the Carman-Kozeny and Jackson-James theories (see Section 2.3), to provide a reasonable prediction of clot structure.

The Phillips model, along with its constituent terms, $S(f)$ and F, is plotted in Figure 2.6. Except for the limiting cases of $\phi \to 0$ and $\phi \to 1$, $S(f)$ does not agree with the Ogston model as one might expect; unfortunately, this issue is not explained in the literature. At low ϕ, the hydrodynamic term F is the one that dominates the diffusion suppression; the steric term $S(f)$ matches (then overtakes) the hydrodynamic suppression at volume fractions of $\phi = 0.005$–0.2, depending on d_f. Fibrin volume fractions are within this range, so Figure 2.6 suggests that steric diffusion suppression should be a factor in fibrin, but *only if the transport is above the steric-*τ.

2.3 Fibrin Structure and Hydraulic Permeability

2.3.1 Darcy Theory

Gels and porous media resist, but do not fully arrest, the flow of fluid. In 1856, Henry Darcy published a treatise on the public fountains of Dijon, France, which included exploration of how a filtration system (sand, in the case of his experimental design) resisted the flow of fluid (Darcy, 1856). The observations of Darcy's original experiments can be generalized for permeants of arbitrary viscosity η and for permeation driven by forces other than gravity (Bear, 1988) to state:

$$\dot{Q} = \kappa \frac{A \Delta P}{\eta L}, \tag{2.14}$$

where $\dot{Q}$ is the volumetric flow rate, A and L are the cross section and length of the filter, and ΔP is the pressure drop across the filter. The coefficient κ has units of area and is called the hydraulic conductivity, or Darcy constant; I will use these terms interchangeably with "permeability". The permeability of a classical porous medium is invariant with the other parameters in Equation 2.14. If, for example, ΔP were increased across a gel, then $\dot{Q}$ would increase in direct proportion, such that the calculated κ would not change.

Blomback and Okada were among the first to recognize the potential value of measuring permeability of fibrin (Blombäck and Okada, 1982). Since that time, the correlations of clot permeability with disease have established permeability as a critical measurement, as discussed in Section 1.1.

The Darcy equation, though a powerful tool, is wholly phenomenological. In the century and a half since his observations were published, much effort has been devoted to predicting κ using information about the material's structure. Initial work in the late 19^{th} and early 20^{th} centuries considered a porous medium to be a collection of capillaries. Intuitively, the volume fraction of the medium could be accounted for by the effective diameter of the capillaries relative to the cross-section of the medium, and the tortuosity of the flow through the medium could be accounted for by the effective length of the capillaries relative to the length of the medium.

2.3.2 Carman-Kozeny relation

The history and usage of the capillary model is described concisely by Carman (Carman, 1937), who provided a simple expression for the Darcy constant κ as a function of S, the surface area per unit volume presented to the fluid, and a Kozeny factor k that captures the structure of the medium. The so-called Carman-Kozeny relation is

$$\kappa = \frac{(1-\phi)^3}{kS^2} = \frac{d_f^2(1-\phi)^3}{16k\phi^2}; \tag{2.15}$$

in his work, Carman explained the relationship between S and d_f. The task, then, is to predict k. For fibrous gels, a Kozeny factor may be assembled after determining the factor for rods parallel ($k_{\|}$) and perpendicular ($k_{\perp}$) to the flow (Happel and Brenner, 1983):

$$k_{\text{rand}} = \frac{2k_{\perp} + k_{\|}}{3} = \frac{1}{3}\left(\frac{4(1-\phi)^3}{\phi(\ln\frac{1}{\phi} - \frac{1-\phi^2}{1+\phi^2})} + \frac{2(1-\phi)^3}{\phi(2\ln\frac{1}{\phi} - 3 + 4\phi - \phi^2)}\right). \tag{2.16}$$

Combining Equations 2.15 and 2.16 gives κ as a function of volume fraction ϕ, shown in Figure 2.7.

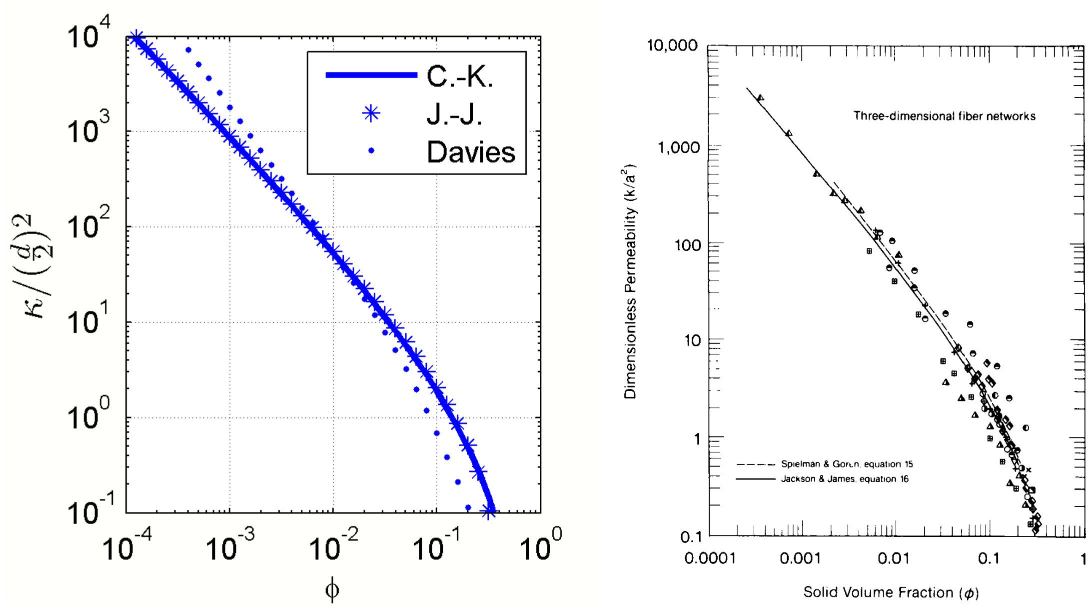

Figure 2.7: Left: $\kappa(\phi)$, according to the Carman-Kozeny (solid), Jackson-James (stars) and Davies (dots) relations. The theories are easier to compare by normalizing away the fiber diameter. None of these equations has been convincingly demonstrated to predict fibrin permeability. Right: The Jackson-James equations has been validated in other fibrous materials over a wide range of ϕ. Critically, over the relevant range of ϕ for clots—say, 10^{-3}–10^{-1}—all three theories are essentially within the scatter of the data used by Jackson and James.

This theory has been validated in fibrous gas filters (Fowler and Hertel, 1940) and beds of aligned cylinders (Astrom et al., 1992). It remains in regular use, including in agarose gels (Pluen et al., 1999) and extra-cellular matrix (Pedersen et al., 2007), and collagen (Ramanujan et al., 2008). However, it has not been validated in fibrin;

because of the inherent challenges of determining clot structure from microscopy, the validation of this theory in fibrin is outside the scope of this dissertation. However, in Section 3.3.1 I show that the Carman-Kozeny theory can be inverted, along with the Phillips Model, to provide a reasonable prediction of clot structure.

2.3.3 Fibrous media: Jackson-James and Davies equations

In an effort to find a solution specific to fibrous media, Jackson and James (Jackson and James, 1986) offered another theoretical solution. They constructed a model using prior theories of flow parallel (Sangani and Acrivos, 1982) (numerical) and perpendicular (Drummond and Tahir, 1984) (analytical) to rigid rods in a square lattice. They applied their equation to data on a wide variety of fibrous networks, including steel wire crimps, wool, yarn, filters, acrylamide gel, collagen, and hyaluronic acid polymer. The volume fractions ranged from $0.0003 < \phi < 0.3$. While fibrin were not included in the fit, the wide variety of fibrous materials used to create the equation suggests it may be broadly relevant for low-volume fraction gels. Their final result was

$$\kappa = \frac{-3}{80}\frac{d_f^2}{\phi}(\ln\phi + 0.931). \tag{2.17}$$

Figure 2.7 shows that the Jackson-James equation shows good agreement with the Carman-Kozeny theory for random arrays of rods.

I have found one example in the literature where fibrin has been tested against a theory of $\kappa(\phi)$. Diamond and Anand compared fibrin permeability for several types of fibrin clots to an empirical equation developed by Davies (Diamond and Anand, 1993),

$$\kappa = \frac{d_f^2}{70\phi^{3/2}(1 + 52\phi^{3/2})}, \tag{2.18}$$

concluding that this equation "accurately correlated" data that they had extracted from earlier published results on fibrin permeability and imaging. However, neither the data nor the method used to extract them were reported, so I cannot say to what precision the Davies equation has been validated. Even more alarming, their citation leads to an equation 4.1.8 in a text (Dullien, 1992) where the coefficients differ from those of Equations 2.18, and the citation is an article I have not been able to find to resolve the discrepancy. Because of its prior use in fibrin, I will bring Equation 2.18 through my discussion in Chapter 3. However, as theoretical rather than empirical models, the Jackson-James and Carman-Kozeny theories are ultimately more satisfying.

The ultimate question, however, is which equation is correct; therefore I stress that the Davies, Jackson-James, and Carman-Kozeny equations, all plotted in Figure 2.7, do not disagree dramatically over the relevant range of fibrin volume fractions ($\phi = 0.001$–0.1). In this range, the theories all appear to lie within the scatter of the data used to determine the Jackson-James equation.

I must also stress that direct validation of any $\kappa(\phi, d_f)$ theories is challenging, because measuring fibrin fiber diameter and volume fraction is notoriously difficult. Optical microscopy can image fibrin without drying, but it loses reliability for size detection below the diffraction limit. Electron microscopy can easily resolve specimens of that size, but the fibers must be dried before they can be imaged, in which case they shrink and frequently collapse. Therefore, as an alternative to imaging based methods, I show in Chapter 3 that by inverting these theories, measurements of diffusion and permeability can provide insight into clot structure (d_f and ϕ).

2.3.4 Permeability and turbidity

I am discussing theories that predict $\kappa(\phi, d_f)$. As explained in Section 1.1, turbidity has been mentioned as a high-throughput measurement of clot structure. Could turbidity therefore be used to find permeability?

The early work on light transmission through fibrin was traditional angle-dependent light scattering (Carr et al., 2004). This work did indeed reveal fiber lengths and diameters, but not all the fibrin studied were polymerized gels.

Carr and Hermans introduced fibrin turbidity shortly after, presumably because it is simpler to perform than angle-dependent light scattering. Turbidity of a solution is the decrease in transmitted light intensity due to scattering and can be calculated by integration of the scattered intensity over all directions (Carr and Hermans, 1978):

$$T = \frac{44}{15} \frac{\pi K \rho_0 \lambda \mu}{T_i} \tag{2.19}$$

where T_i is the turbidity at the start time, ρ_0 is the fibrinogen concentration, λ is the incident wavelength, μ is the linear mass density of the fiber (sometimes called "mass-length ratio"), and K is a constant that captures the refractive index n of the material,

$$K = \frac{2\pi^2 n^2}{N_A \lambda^4} \left(\frac{\mathrm{d}n}{\mathrm{d}\rho_0} \right)^2 ,$$

where N_A is Avogadro's number.

The angular integration that makes turbidity so convenient as a methodology ruins its potential as a complete probe of gel structure—namely, of ϕ and d_f. Consider the definition of volume fraction,

$$\phi = \frac{\pi}{4} n_f d_f^2 L_f \tag{2.20}$$

where n_f is the number density of fibers and L_f is the length of an average fiber. The problem is already apparent: Equation 2.20 has three inputs, but turbidity provides only two quantities related to structure, μ and ρ_0. In detail, we would begin by using $V_f = (\pi/4) d_f^2 L_f$ to write

$$L_f = \frac{m_f}{\mu} = \frac{mN}{\mu} \tag{2.21}$$

$$n_f = \frac{n}{N} = \frac{\rho_0}{mN}, \tag{2.22}$$

where V_f is the volume of the fiber, m_f is the average fiber mass, m is the mass of a fibrin monomer, and N is the average number of fibrin monomers in a fiber. Eliminating

N, we find,

$$L_f = \frac{\rho_0}{\mu n_f}, \qquad \text{so} \qquad \phi = \frac{\pi}{4}\frac{\rho_0}{\mu} d_f^2, \tag{2.23}$$

and we are left without d_f. Recognizing $m_f = \rho V_f$, we can write

$$d_f = 2\sqrt{\frac{V_f}{\pi L_f}} = 2\sqrt{\frac{\mu}{\pi \rho}}, \tag{2.24}$$

where ρ is the density of monomers in the fiber. This last quantity, ρ, is essentially the packing of fibrin monomers in a fiber, and it is unknown. Fibrin fibers are under tension, and that tension may increase as fiber diameter increases (Weisel, 2004), which would cause ρ to scale with N. Studies with AFM of dried fibrin fibers have indicated that the fiber density varies with the radial distance from the axis of the fiber (Guthold et al., 2007). For these reasons, we cannot assume that ρ is constant. Thus, turbidity cannot provide sufficient information to extract gel structure.

The coagulation community relies heavily on turbidity for understanding of clot structure, and has built an intuition of how turbidity and permeability are related[2]. I will linger on this topic to highlight a potential hazard in the way the measurement is presently used. For two clots with the same polymerization rate, but different final transmission, there is ambiguity in the clot structure, highlighted in Figure 2.8. The lower final turbidity could be due either to a lower clot volume fraction at a constant fiber diameter, or to a smaller fiber diameter at a constant volume fraction. The first

---

[2] My thanks to Alisa Wolberg for helpful conversations on this topic.

case is achieved by reducing the number density of fibers; this would result in a higher permeability. The second case is achieved by increasing the number density of fibers; this would result in a lower permeability.

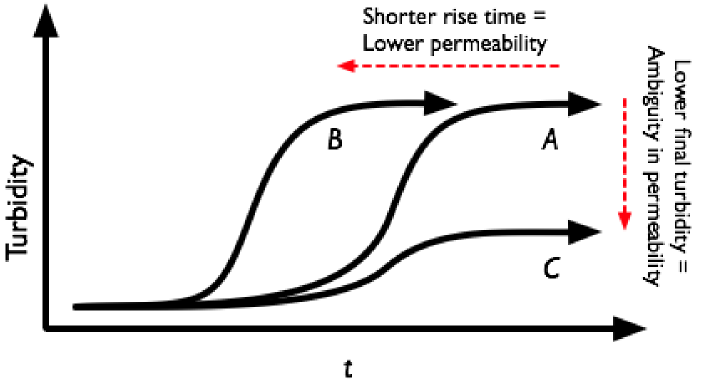

Figure 2.8: Turbidity provides a glimpse into gel structure. Compared with some reference clot (curve A), faster polymerization (indicated by faster rise times, curve B), implies a finer clot. A lower final turbidity (curve C) could be due to lower ϕ (lower fibrin concentration), which would correspond to a clot with greater permeability than the reference clot. However, lower final turbidity could also be due to smaller fiber diameter (higher thrombin concentration), and this type of clot would be expected to have a lower permeability.

The ambiguity becomes particularly treacherous as more biochemical factors are introduced. Consider, for example, the relationship between turbidity and permeability for clots formed in the presence of aspirin (Ajjan et al., 2009). Electron microscopy shows that clots formed in the presence of aspirin have a coarser structure with thicker fiber diameters, which is similar to the changes in clot structure achieved by decreasing thrombin concentration, but without the change in clotting time. Aspirin does not change clotting rate, but it increases the final turbidity. Is this because aspirin promotes lateral aggregation, decreasing number density of fibers and increasing permeability? Or is it because aspirin alters lateral aggregation in some fashion, causing fibers to swell without changing their number density, causing no affect or a small decrease in permeability? The complexity of the system leaves open questions which turbidity alone cannot answer.

2.4 Diffusion and Permeability

A wide range of scientists and engineers are concerned simultaneously with fluid permeation and particle transport through a medium. The filtration community is concerned less with particle diffusion than with the rejection rate of particles moving through a barrier (Zamani and Maini, 2009), and therefore pore sizes in the filter are typically designed to be smaller than the particles expected to be passing through, hydrodynamic effects are typically ignored, and electrostatic effects are considered in detail (Wijmans and Baker, 1995; Szymczyk and Fievet, 2005). Geological sciences consider gas perfusion through soil and rock (Hamamoto et al., 2009), but pressure-driven advection make dispersion, or mixing, a more relevant phenomenon than in gels studied *in vitro*. Novel device research can present an interesting area of overlap, as some research considers how adding nano-devices to bulk material can enhance particle diffusion or modify bulk permeability (Zhong et al., 2003; Srebnik and Sheintuch, 2009).

There is great interest in these two measurements in polymer gels community. Collagen, extracellular matrix, and agarose have all been studied for this relationship (Ramanujan et al., 2008; Pedersen et al., 2007; Pluen et al., 1999; Levick, 1987). In these experiments, the question is typically whether particle diffusion can be predicted from permeability; the latter being a bulk measurement that requires no specialized equipment. However, absent from the discussion about the relationship between the two phenomena is the time- and length-scale dependence over which diffusion occurs will have a dramatic impact.

Consider an effort to predict the speed of inter-cellular communication for cells embedded in extracellular matrix. The distances are short—perhaps just tens of nanometers—so steric effects between the diffusing molecule and the gel may not be relevant, producing faster diffusion and therefore faster communication. Hydrodynamic effects would still be present. Permeability is also a hydrodynamic effect. An equation that linked hydrodynamic diffusion suppression with permeability could predict the speed of this communication by measuring bulk gel permeability, which might be easier than a nanometer-resolution, high-bandwidth measurement of diffusion.

Fibrin presents a convenient system to confirm such a theory, because the inter-fiber distance is measured in hundreds of nanometers or more, where for some polymer gels the distances can be tens of nanometers or smaller.

Furthermore, a relationship between permeability and diffusion would be especially useful for coagulation science, because it presents the possibility that clot permeability could be measured in high throughput. There is indeed a theory that relates D_{eff} and κ. In addition to establishing a relationship between these quantities, it can also help isolate whether hydrodynamic or steric effects are dominating particle diffusion.

2.4.1 Effective medium theory

In 1949, Brinkman presented an "effective medium" theory to determine the force on a granule suspended in a fluid-filled porous medium (Brinkman, 1949). He assumed nothing about the medium except that it had a permeability κ. In his treatment, the continuity condition on the fluid velocity at the edge of the pocket in which the granule was located increased the friction on the granule—in short, it was a model for the hydrodynamic effect discussed in Section 2.1.4. The theory is valid in the regime $\phi < 0.6$, which comfortably encompasses the full range of fibrin and plasma clots, and many whole blood clots.

Is the hydrodynamic effect modeled in the effective medium theory valid for a diffusing particle? This was the supposition of Phillips (Phillips et al., 1989), who presented a relationship between κ and D_{eff}:

$$\frac{D_{\text{eff}}}{D_0} = (1 + \sqrt{\frac{d^2}{4\kappa}} + \frac{d^2}{3\kappa})^{-1}, \tag{2.25}$$

where D_0 is the diffusion coefficient of the particle in solvent, d is the particle diameter, and κ is the Darcy coefficient of the gel.

Equation 2.25 is essentially phenomenological. The equation has no fundamental gel structure (*e.g.* ϕ or d_f), only the empirical quantity κ. I discuss this theory because permeability is a well-established measurement in clots, so the effective medium theory will be straightforward to test. By contrast, there is no validated technique for measuring ϕ in clots, and techniques for measuring d_f are questionable, perhaps to within a factor of two, due to the potential effects of drying (electron microscopy) or deconvolution (confocal microscopy). These experimental challenges present limitations on the accuracy with which the above theories of $D_{\text{eff}}(\phi, d_f)$ and $\kappa(\phi, d_f)$ could be tested directly.

Because the effective medium theory only models hydrodynamic diffusion suppression, its validity would show that hydrodynamic, rather than steric effects, were determining particle diffusion. This result would be an important first step toward identifying which of the $D_{\text{eff}}(\phi, d_f)$ and $\kappa(\phi, d_f)$ were relevant.

It has been suggested, but not demonstrated, that effective medium theory applies to nanoparticle diffusion in fibrin (Diamond, 1999). The effective medium theory has been tested in agarose, where it was found to overestimate ${}^{D_{\text{eff}}}/_{D_0}$ (Johnson et al., 1996). The issue in agarose appeared to be that steric effects were ignored. Using Equation 2.25 as F from Equation 2.13 improved agreement. In Chapter 3, I explain that this prior work was observing diffusion at timescales longer than the steric-τ. In my work, I use a higher-bandwidth single-particle tracking technique, which measures D_{eff} over sub-micron distances. I show that the data appear to be within the startup-τ, and show that the effective medium theory therefore holds in fibrin gels.

2.5 Conclusion

For a fibrin gel, which may plausibly be modeled as a low-volume fraction, rigid rod matrix, I have discussed the theoretical landscape connecting structure, diffusion, and permeation. The relevant models are summarized in Figure 2.9. The Ogston and Phillips models both predict diffusion suppression as a function of gel structure. However, the Ogston model accounts only for steric supression, where the Phillips model accounts for both steric and hydrodynamic interaction.

Model	**Output**	**Input**	**Validated in fibrin**	**Foundation**	**Phenomena treated**
Ogston	D_{eff} / D_0	ϕ, d_f	no	Stochastic physical model	Steric effects
Phillips	D_{eff} / D_0	ϕ, d_f	no	Numerical physical model	Steric and hydrodynamic effects
Carman-Kozeny	κ	ϕ, d_f	no	Analytical physical model	Steric and hydrodynamic effects
Jackson-James	κ	ϕ, d_f	other fibrous materials	Empirical fit to regular rigid rod lattice model	N/A
Davies	κ	ϕ, d_f	some fibrin clots	Empirical fit	N/A
Effective Medium	D_{eff} / D_0	κ	no	Semi-empirical model	Hydrodynamic effects

Figure 2.9: Summary of the models under consideration.

The effective medium model is a semi-empirical equation that connects diffusion and permeability. It accounts only for hydrodynamic suppression of the diffusion coefficient. It is useful because well-established methods exist for measuring fibrin permeability, and it should be straightforward to test this theory's validity. If the effective medium theory applies, we should ignore the (wholly steric) Ogston model in favor of the Phillips model.

After measuring diffusion and permeability, it should be possible to use appropriate equations for ${}^{D_{\text{eff}}}/_{D_0}$ and κ to estimate ϕ and d_f. In Chapter 3, I will measure fibrin permeability, structure, and diffusion, and in this manner establish the relevance of the theories above to fibrin gels.

Chapter 3

Transport in Fibrin: Experiments

To evaluate the relevance of the theories in Chapter 2, I have measured the diffusion coefficient D_{eff} and permeability κ in the clots of Figure 2.2. In this Chapter I test the relevance of the effective medium theory, then apply the Phillips and Davies models to extract the clots' structure. I demonstrate that, as expected the effective medium theory can be applied to measure clot permeability in high throughput. I explore how diffusion can be used to reveal information about gel structure. Finally, I discuss the implications of my results on drug design and delivery.

Diffusion will prove useful as a clot characterization assay only insofar as it is sensitive to relevant clot properties. In this chapter I demonstrate that with the correct probe size, D_{eff} varies across concentrations of fibrinogen (0.5–3 mg/mL) and thrombin (1–10 nM). As Figure 2.2 shows, clots formed under these conditions span a wide range in gel structure. I also measure diffusion in platelet-poor plasma (PPP), which bolsters this assay's physiological relevance and broadens the usefulness of the assay for coagulation science, as PPP is easier and cheaper to prepare than purified fibrinogen.

The PPP gels I study are prepared from plasmas collected from normal individuals and hemophilic patients. Hemophilia is a genetic disorder that manifests as hypocoagulability due to a deficiency of either FVIII or FIX. (This specimens in this study suffer from FVII deficiency.) It can be treated by the addition of activated recombinant FVII (rFVIIa), which should restore clotting function. The phenotype of the disorder and of the treatment were shown in Figure 2.2: the normal clots are finer than the hemophilic clots, and rFVIIa partially restores some of the normal clot structure. The specimens in this study were acquired from A. Wolberg and prepared with the help of R. Campbell.

3.1 Measuring nanoparticle diffusion

In an effort to separate physical from chemical interactions, I employed nanoparticles with polyethylene glycol (PEG) surface treatment, which have been shown to reduce particle-protein affinity (Valentine et al., 2004). Reagent handling, specimen preparation and experimental setup is explained in Appendix A, and summarized in Figure 3.1[1]. Briefly, purified fibrinogen, human α-thrombin (Enzyme Research Laboratories, South Bend IN), and nanoparticles (Invitrogen, Carlsbad CA) with PEG surface chemistry are diluted in HEPES-buffered saline (HBS: 20 mM HEPES, pH 7.4, 150 mM NaCL), and mixed to trigger fibrin gel formation. Gels are prepared in a 96-well, optical-bottom microplate (Matrical, Spokane WA), and allowed to polymerize

---

[1] I am greatly indebted to Rachel Sircar for her tireless work PEGylating particles, tracking particles, and most importantly, refining the diffusion protocols described in this chapter.

for 2 hours. The microplate is placed on an inverted widefield fluorescence microscope, where videos of particle diffusion are acquired from five fields of view for 60 s each. Particle trajectories are automatically tracked with CISMM Video Spot Tracker, then filtered for tracks that last less than 2 s. The quantity $\langle r^2 \rangle$ is calculated for a range of lag times ranging from about 1 ms–10 s.

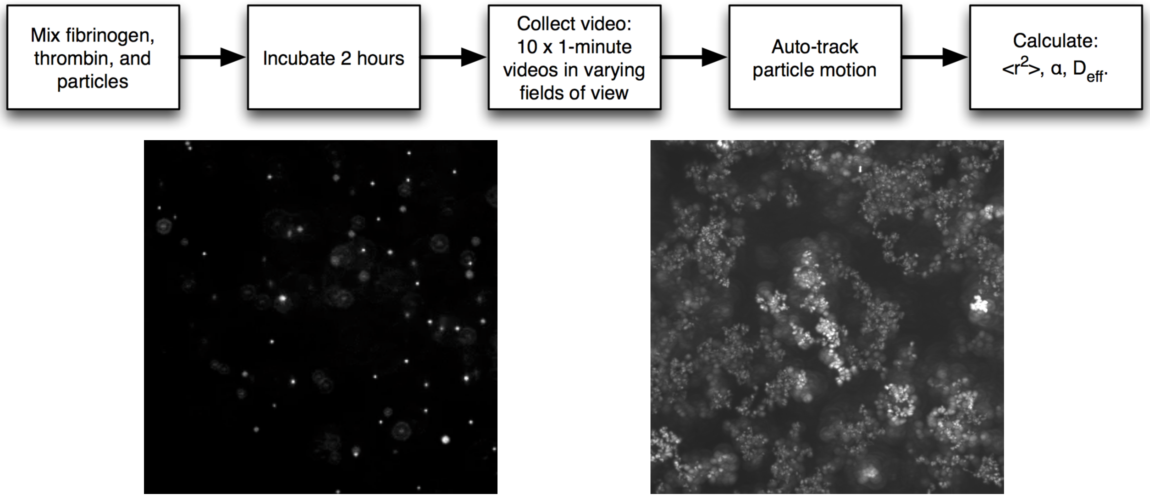

Figure 3.1: Top: Experimental pipieline for diffusion experiments. To simplify mixing and data collection, clots are prepared in a 96-well microplate. Bottom left: a typical frame out of a video of diffusing 500 nm particles. Bottom right: a maximum intensity projection, showing how diffusing particles sweep out some area over a period of time. Each image is 140 μm on a side. Dots are brighter when the particle is more in focus, so the dimming and blurring that produce the sense of perspective are not wholly misleading.

Video capture and automatic single-particle tracking generates thousands of particle paths. Typical particle paths and the resulting plot of $\langle r^2 \rangle(\tau)$, shown in Figure 3.2, reveals the heterogeneity of the particles' environment, as well as highlighting errors of the auto-tracking algorithm. Issues with auto-tracking, and other subtleties of transitioning to high-throughput diffusion measurements, are discussed in Chapter 5.

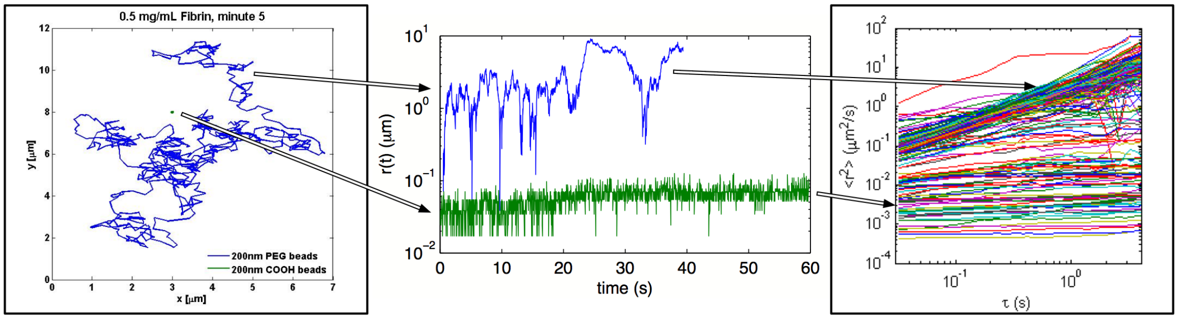

Figure 3.2: Overview of the data analysis pipeline, showing how stuck and freely diffusing particles are represented at various stages of the analysis. Left: Typical particle paths for particles with and without PEG surface chemistry. Middle: Particle trajectory $r(t)$ for a freely diffusing and a stuck particle. The freely diffusing particles move farther from their original location ($r = 0$) and are usually tracked for shorter periods of time, because they diffuse out of plane. Right: Mean squared displacement $\langle r^2 \rangle$ from a typical specimen of 500 nm PEG particles in 1 mg/mL fibrinogen and 10 nM thrombin. To improve legibility, only 20% of tracks are plotted. There are two core populations: freely diffusing ($\alpha \to 1$) and stuck ($\alpha \to 0$) tracks. Errors of the auto-tracking algorithm produce outlier tracks, discussed further in Section 5.2.1. The noise floor for this measurement is $\sim 10^{-3} \mu\text{m}^2$ at all $\tau < 1$ s, representing particle motion of 32 nm.

3.1.1 Diffusion in fibrin is size-dependent and bimodal

Figure 3.3 indicates that the diffusion of particles in fibrin is bimodal. The majority of particles diffuse freely ($\alpha \to 1$). This behavior is statistically equivalent to particles diffusing in a purely viscous fluid. The remaining particles have a dramatically lower powerlaw dependence ($\alpha \to 0$), indicative of a “stuck” particle.

Nanoparticle diffusion varies when the particle size is changed from 200 nm to 1 μm, as shown in Figure 3.4. The percentage of stuck beads is typically larger in finer clots, or with increasing fibrin concentration. However, the relative size of the free and stuck populations is not stable. Occasionally I observe clots with a high percentage ($> 50\%$) of stuck particles when there was no apparent difference in the preparation or structure

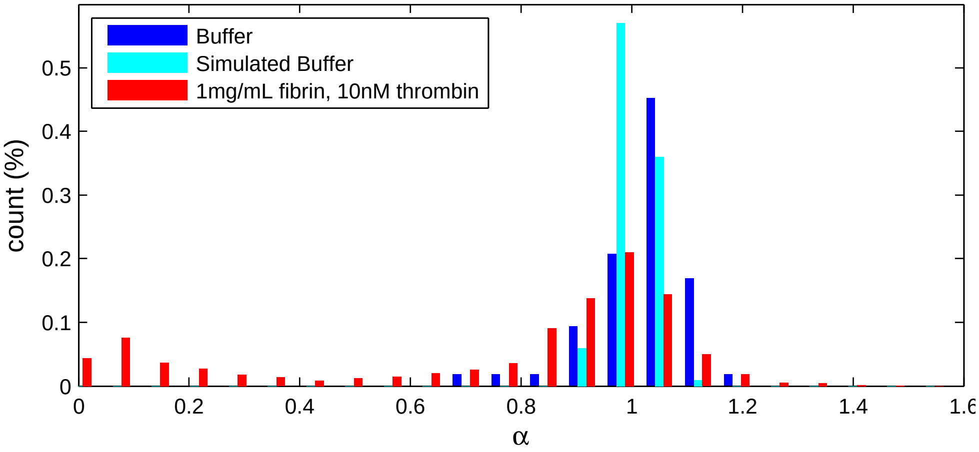

Figure 3.3: The behavior of diffusing beads in fibrin (red bars) is bimodal. $\alpha \to 1$ for most particle traces, and a distinct population shows sub-diffusive behavior. "Freely diffusing" particles are defined as those with $0.8 < \alpha < 1.2$. Diffusing particles in buffer (blue bars) and random-walk simulations (cyan bars) have no stuck population. The buffer data is centered slightly above $\alpha = 1$ due to small amounts of drift generated by the fluorescence illumination.

of the clots themselves. Such results were more common in platelet-poor plasma (PPP) clots than in purified fibrin clots.

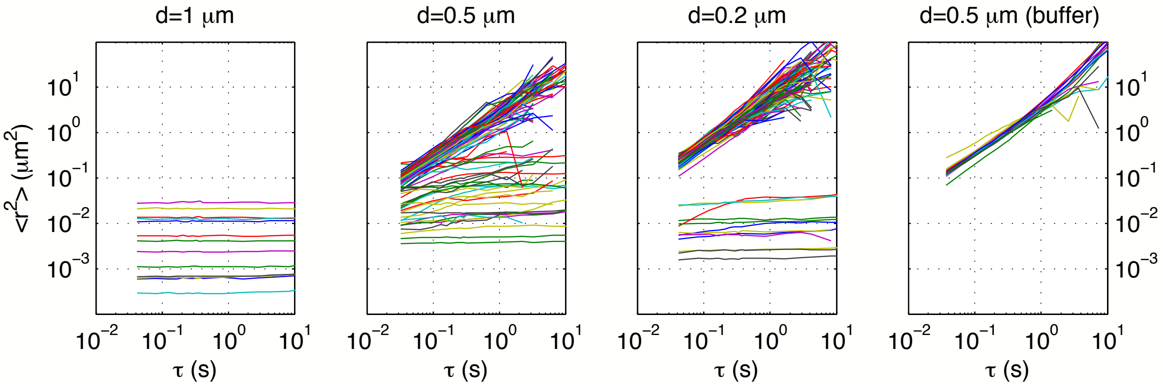

Figure 3.4: $\langle r^2 \rangle$ for particles from 0.2–1 μm. As particle size decreases, so does the percentage of stuck tracks. Stuck tracks are identified by a lower powerlaw (slope), α. Also, the distance the particles diffuse (vertical position of lines) increases.

We verified that free diffusion on the micron scale can produce long-distance transport. We prepared clots where the particles were not present during gel formation. Clot formation was measured using turbidity, shown in Figure 3.5, which showed that all clots types reached final absorbance after 2 hours; in this and all subsequent experiments, 2 hours was taken to be the incubation time for clot formation. After clot formation, 500 nm particles were placed above the clot. The clots were $\sim$ 1 mm in height, determined by using a long working distance objective to find particles at the top of the clot. Particles first became visible at the other side of the clot ($< 100\ \mu$m from the coverglass) at about 24 hours. The concentration of particles near the coverglass stabilized after $\sim$ 72 hours. implying a bulk diffusion coefficient $D_{\text{bulk}} = x^2/\tau \ \sim\ 1\ \mu\text{m}^2/s$, where x and τ are the first passage distance and first passage time, respectively.

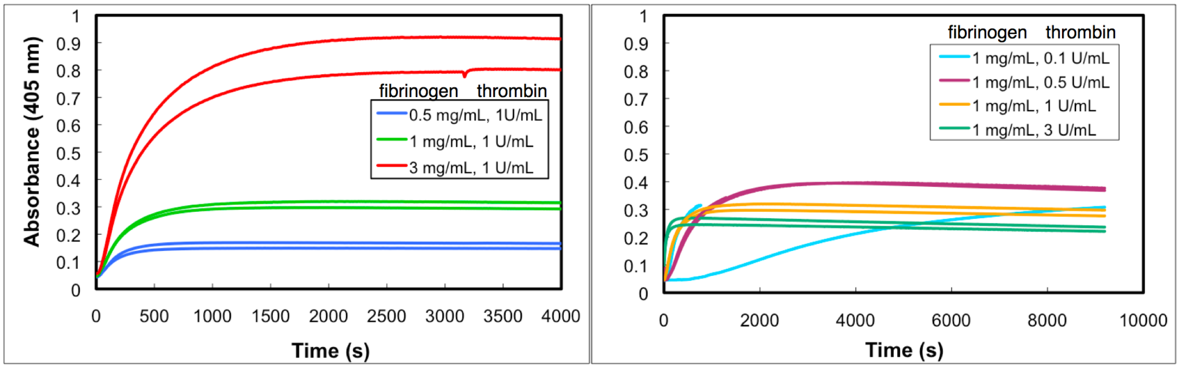

Figure 3.5: Turbidity is a common measurement of gel formation. The higher the final absorbance, the thicker the fibers. When the fibers are finished aggregating, the absorbance stops increasing, creating the plateaus seen in these plots. Formation of the 1 mg/mL fibrinogen, 1 nm thrombin clot (teal, right-hand plot) took two hours, which determined the incubation time for gel formation.

3.1.2 Sensitivity to clot structure

We measured nanoparticle diffusion in a range of purified gel types, from low to high thrombin concentration (1–30 nM) and low to high fibrinogen concentration (0.5–3 mg/mL), with the two particle sizes ($d = 260$ and 500 nm) that have populations where $\alpha \to 1$. For these freely diffusing particle traces, we calculated D_{eff} from Equation 2.2. Although $\langle r^2 \rangle \propto \tau^1$ is indicative of free diffusion, the fibrin gel apparently suppresses the particles' motion: where $D_0 = 0.94 \pm 0.02 \mu\text{m}^2/s$ for 500 nm particles in water, D_{eff} drops with decreasing clot coarseness, reaching 75% of D_0 in 1 mg/mL fibrin and 30 nM thrombin and 58% of D_0 3 mg/mL fibrinogen, 10 nM Thrombin.

In a purely viscous fluid, $D = \frac{k_B T}{3\pi\eta d}$, where k_B, T, and η are Boltzmann's constant, absolute temperature, and the dynamic viscosity, respectively. Therefore, the product dD_{eff} is a function exclusively of specimen parameters, and any variation with particle size could be interpreted as a variation in the effective viscosity or temperature of the particle's environment. Results for dD_{eff} of 500 and 260 nm particles are shown in Figure 3.6. In coarser clots (namely, 1 mg/mL fibrinogen with 0–5 nM thrombin, and 0–0.5 mg/mL fibrinogen with 1 mg/mL thrombin), particles of both sizes experience a similar environment that is effectively more viscous than pure buffer. As the clots grow finer, the diffusion of 500 nm particles drops faster than that of 260 nm particles.

Nanoparticle diffusion in platelet-poor plasma (PPP) clots is also sensitive to structure. We measured D_{eff} for normal ($0.51 \pm 0.005\ \mu\text{m}^2/s$), hemophilic ($0.58 \pm 0.007\ \mu\text{m}^2/s$), and recombinant factor VIIa (rFVIIa)-treated hemophilic ($0.57 \pm 0.005\ \mu\text{m}^2/s$) clots. In agreement with the correlation seen in purified fibrinogen gels, the diffusion is greater in

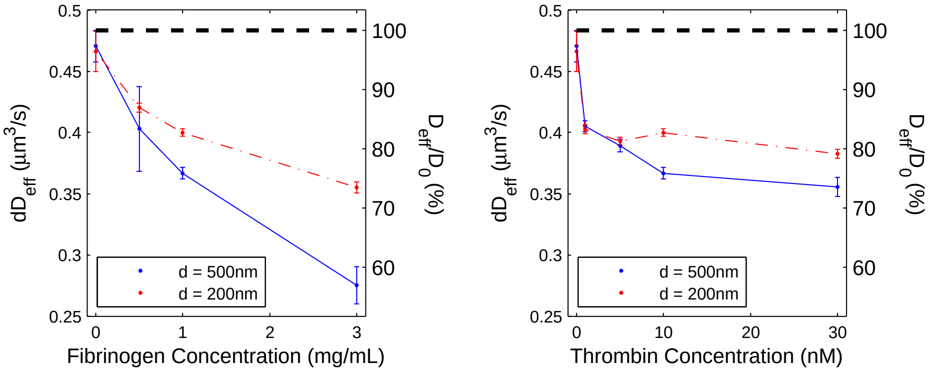

Figure 3.6: D_{eff} of freely diffusing ($\alpha = 1$) nanoparticles is sensitive to clot structure. Left: Diffusion under varying fibrinogen concentration (thrombin concentration 10 nM). D_{eff} of 500 nm particles (solid), diverges from buffer value (0 mg/mL fibrinogen) with increasing thrombin concentration. 260 nm particle diffusion (dash-dot) is also suppressed by the gel, but the particles are less sensitive to the changes in gel structure. Right: A similar effect occurs with 260 nm and 500 nm particles under varying thrombin concentration (fibrinogen concentration 1 mg/mL). In both graphs, the dashed line is the theoretical prediction of dD_{eff} for a sphere diffusing in water. In a homogeneous material, the quantity dD_{eff} for two particles of different sizes is expected to be invariant. As this is not the case, nanoparticles of different sizes effectively experience different surroundings. Number of trackers $N > 500$ for each data point; bars show 95% confidence intervals.

the coarser hemophilic clots as compared with the finer normal clots. rFVIIa has been shown to partially restore the clot structure and stability that is lost in hemophilic clots (Wolberg et al., 2005), and we observe that the rFVIIa treatment also partly restores diffusion to its normal value.

There is a possibility that the presence of particles during gel formation might alter the kinetics of gelation. I tested clots both with particles diffusing into the clot from above, and with particles present from the start of polymerization. Figure 3.7 shows that the presence of nanoparticles during polymerization does not substantially affect the measurement.

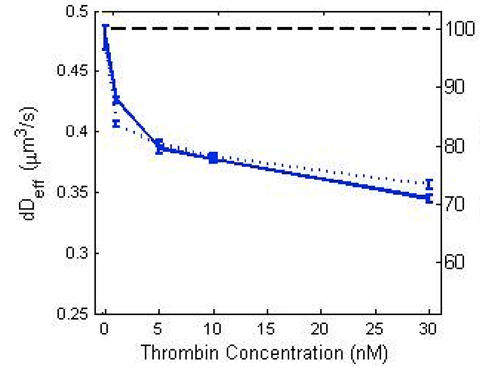

Figure 3.7: Results for D_{eff} are similar whether particles diffuse into a fully formed clot (solid line), or are present during gel formation (dotted line). Particles are 500 nm. The dashed line is the theoretical value for diffusion in buffer. Number of trackers $N > 500$ for each data point; bars show standard error.

3.1.2.1 Statistical Significance

The short time over which I can track the particles (typically 2–5 s) results in a naturally large standard deviation σ_d behind each datapoint in Figure 3.6; it is often more than twice the differences in mean diffusion coefficient that these measurements reveal. However, the large sample population (> 500 trackers for each clot type) allows a high-confidence measurement. In my analysis, I calculate the standard error σ_e, defined as standard deviation divided by the square of the population size. The standard error is the standard deviation expected in the mean in the event that I repeatedly performed the same measurement on an identical specimen. The 95% confidence interval (equivalent to a p-value of 0.05) of a normal distribution is 1.96 standard deviations. Therefore, the 95% confidence interval for the diffusion coefficient is

$$\sigma_{95} = 1.96\sigma_e = \frac{1.96}{\sqrt{N}}\sigma_d = \frac{1.96}{\sqrt{N}}\sqrt{\bar{D_i^2} - \bar{D_i}^2}, \tag{3.1}$$

where D_i is the D_{eff} calculated for each tracker. It is this 95% confidence interval that is plotted as error bars in Figure 3.6.

3.1.3 Long-time diffusion

Particles are typically tracked for less than 5 seconds, because the depth of field is about 4 μm and $D_{\text{eff}} \sim 1$ μm^2/s. Tracking particles for longer requires dynamically adjusting the imaging plane. I am indebted to R. Schubert's efforts in creating Z-Chaser, a software algorithm that accomplishes this task using a three-axis piezoelectric stage. We have used Z-Chaser to track particle motion[2] for up to 10 min. Clots were prepared, video was acquired and tracked, and data were analyzed as described above. The resulting $\langle r^2 \rangle(\tau)$ is plotted in Figure 3.8.

At short timescales (< 1 s), the particles of Figure 3.8 have a slope $\alpha = 1$, similar to the particles tracked in Figure 3.4. Unlike those experiments, however, these particles generally maintain a stable α for $\tau < 80$ s, where the particles tracked for short times (fixed focal plane) show scatter in α around $\tau > 1$ s. This disparity is due to the shorter observation time, which leads to more random $\langle r^2 \rangle$ measurements near the long-τ end of these plots.

Interestingly, two particles in the densest clots show a downward concavity that begins above 10–20 s. One possible explanation is that the particles have moved far enough (1–10μm, according to Figure 3.8) to collide with the fiber mesh; these steric interactions would manifest as timescale-dependent collisions, causing suppression in

---

[2] I am indebted to Elizabeth Littauer for her work collecting fibrin diffusion data using Z-Chaser

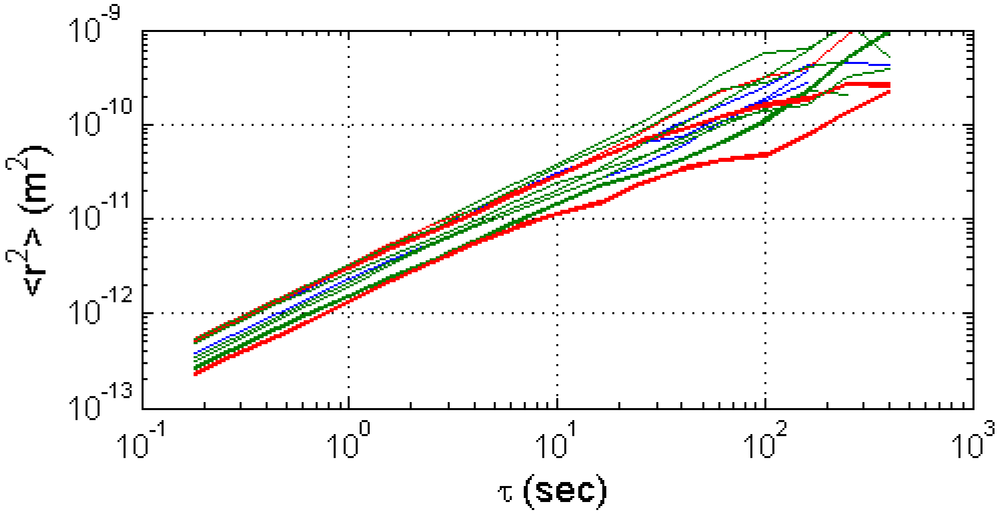

Figure 3.8: $\langle r^2 \rangle$ for particles tracked for longer than 1 min. Clots were 10 nM thrombin with 0.5 mg/mL (blue), 1 mg/mL (green), or 3 mg/mL (red) fibrinogen. Most tracks show no meaningful deviation from the short-time diffusion statistics. However, two particles in the densest clots (bold red lines) show a downward concavity that begins above 10–20 s. This change in α may represent steric diffusion suppression.

$\langle r^2 \rangle$.

3.2 Clot permeability

Clot permeability was measured[3] using a simple constant-pressure design, as shown in Figure 3.9.

Clot permeabilities were in the expected range for purified clots—for example, see (Blombäck and Okada, 1982). As expected, the permeability dropped as the number density of fibers increased (*i.e.*, finer clots), as measured at a range of thrombin and fibrinogen concentrations. The permeabilities measured are summarized in Figure 3.10.

---

[3] I am indebted to Joseph Sircar for his work refining this permeability protocol and collecting the data presented here.

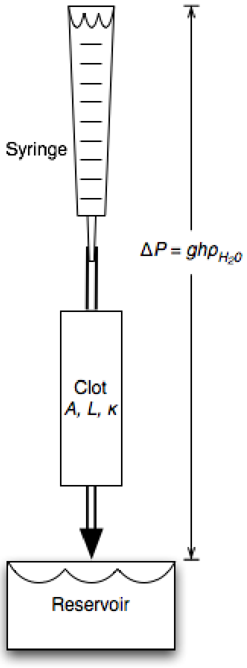

Figure 3.9: Experimental apparatus for permeability experiments. The column height h is adjustable, to provide permeability measurements at a range of head pressures. Permeability is calculated according to Equation 2.14, where $\dot{Q}$ is measured as volume change in the syringe over time.

Fibrinogen (mg/mL)	Thrombin (nM)	κ (μm²)	Std Dev. (%)
1	5	3.31	68
1	10	0.96	21
1	30	0.34	24
3	10	0.12	31

Figure 3.10: Summary of permeability measurements. The permeability could not be determined for the coarsest clots (1 mg/mL fibrinogen, 10 nM thrombin and 0.5 mg/mL, 1 nM thrombin), because clots were not stable under the lowest head pressures (2.7 kPa), which corresponds to a column height $h = 27$ cm.

3.2.1 Applicability of effective medium theory

In Section 2.4.1 I explained that effective medium theory is useful because (1) it can be easily tested and (2) it accounts only for hydrodynamic diffusion suppression. If it applies, it helps clarify the relevant phenomena governing nanoparticle transport in fibrin. Figure 3.11 shows that the data are in agreement with the effective medium theory, which predicts D_{eff} as a function of a medium's Darcy constant κ and a particle diameter d. Note that this agreement does not rely on fitting parameters: κ, D_{eff}, and d were all measured independently.

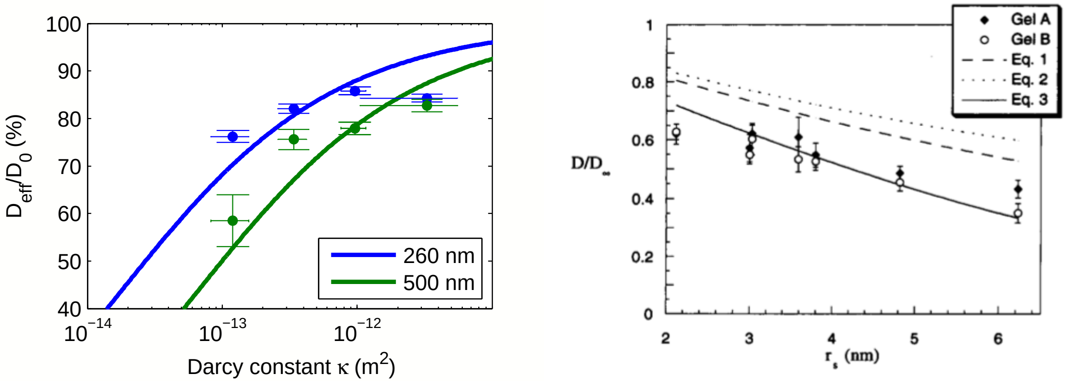

Figure 3.11: Left: My data (dots) for D_{eff} (from Figure 3.6) and κ (from Figure 3.10 validate the effective medium theory (lines). Diffusion and permeability were measured on clots made from 1 and 3 mg/mL fibrinogen with 10 nM thrombin, and 1 mg/mL fibrin with 5, 10, and 30 nM thrombin. Bars are 95% confidence intervals. Right: Results showing poor agreement between data and the effective medium theory (dashed line, labeled "eqn. 2") in agarose gels (Johnson et al., 1996). The theory that shows better agreement (solid line, labeled Eq. 3) uses Equation 2.13, but uses Equation 2.25 in place of F. The need for a steric term is not because the relative sizes of particles and fibers were different, but because the timescale of the measurement was too long.

My validation of the theory here contradicts the results of prior work in agarose gels (Johnson et al., 1996). In that study, the particles were 4–12 nm in diameter and the inter-fiber spacing of the gels was roughly 4–11 nm, using their estimation of $R = {}^{\sqrt{\kappa}}/_{2}$. In some cases, then, the relative sizes of particles and mesh size are similar to those of my results in fibrin (with, say, 500 nm particles and 1–5 μm fiber spacing). Yet their measurements show that the effective medium theory predicts 20–30% higher values for ${}^{D_{\text{eff}}}/_{D_0}$. The reason is that their diffusion measurement occurred over 20 μm, a distance over which a particle in agarose would have passed thousands of strands. Therefore, the measurement was clearly taken for longer than the steric-τ, or in region III of Figure 2.5.

Figure 3.12 clarifies this distinction for diffusion measurements in an arbitrary fibrous gel. I have scaled the axes by the length and timescales of the diffusion measurement, so that the steric effect should begin at position $(1, 1)$. To place the fibrin experiments of this work and the agarose experiments of Johnson *et. al.* in the context of this Figure, consider that for fibrin that $\tau_{\text{startup}} \sim 10$ s (as suggested by Figure 3.8), and my diffusion measurements were taken below $\tau = 1$ s, so ${}^{\tau}/_{\tau_{\text{steric}}} \sim {}^{1}/_{20}$—clearly in the hydrodynamic regime. By contrast, the agarose data have ${}^{\langle r^2 \rangle}/_{R^2} \sim {}^{20\ \mu\text{m}}/_{(10\ \text{nm})^2} \sim 10^6$—clearly in the steric regime.

3.2.2 Measuring permeability with effective medium theory

It is convenient that the effective medium model applies to fibrin, because a high throughput diffusion assay could measure clot permeability. However, there is an apparent difficulty: according to Equation 2.25, D_{eff} is determined both by the gel (through κ) and the viscosity and temperature of the solvent (through D_0). In clots—particularly

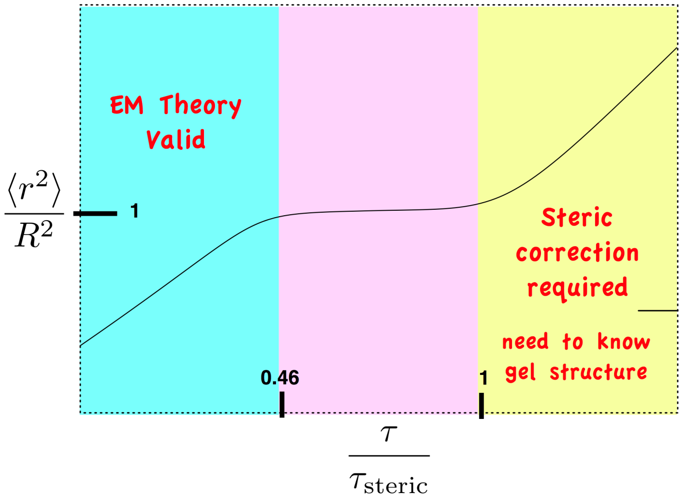

Figure 3.12: A scaled version of Figure 2.5 that clarifies this distinction for diffusion measurements in an arbitrary fibrous gel. I have scaled the y-axis by the length-scale of steric interactions R^2, and the x-axis by the timescale of steric interactions τ_{steric}, so that the steric effect should begin at position $(1,1)$. Critically, diffusion cannot be related to permeability in the steric region without knowing detailed gel structure (namely, ϕ and d_f), while in the hydrodynamic-only regime, the effective medium theory can be used for this purpose.

those of plasma or whole blood—the solvent is not well controlled, and may vary substantially from the viscosity of water. In fact, a higher viscosity is expected in PPP; a D_0 roughly 30% lower than that in water has been measured in PPP (Kirschenbaum et al., 2000), and the viscosity of blood is 2- to 100-fold $\eta_{\mathrm{H_20}}$ (Rand et al., 1964). Conceivably, this viscosity could be measured by eluting the solvent from the clot and measuring its viscosity independently, but this would be impractical in a high throughput protocol.

The solution is to determine the ratio of D_{eff} for two particle diameters

$$\frac{D_{d_1}}{D_{d_2}} = \frac{d_1}{d_2} \, \frac{12\kappa + 6d_2\sqrt{\kappa} + d_2^2}{12\kappa + 6d_1\sqrt{\kappa} + d_1^2}. \tag{3.2}$$

This normalizes away η_0, relieving the need to independently determine the solvent viscosity at the cost of a second, nearly identical diffusion measurement in each type of clot.

I can follow this prescription with the data above to find the ratio D_{d_1}/D_{d_2} in each clot type. The data show satisfying agreement with the theory, as shown in Figure 3.13. However, the sensitivity of this measurement is not good: small variations in $D_{200\ nm}/D_{500\ nm}$ result in sharp changes in κ. The sensitivity of this technique (essentially, the slope of the solid line in Figure 3.13) depends critically on the sizes of the particles relative to each other and to $\sqrt{\kappa}$. For comparison, I have also plotted $D_{100\ nm}/D_{800\ nm}$, which shows improved sensitivity. Unfortunately, 800 nm particles are not commercially available.

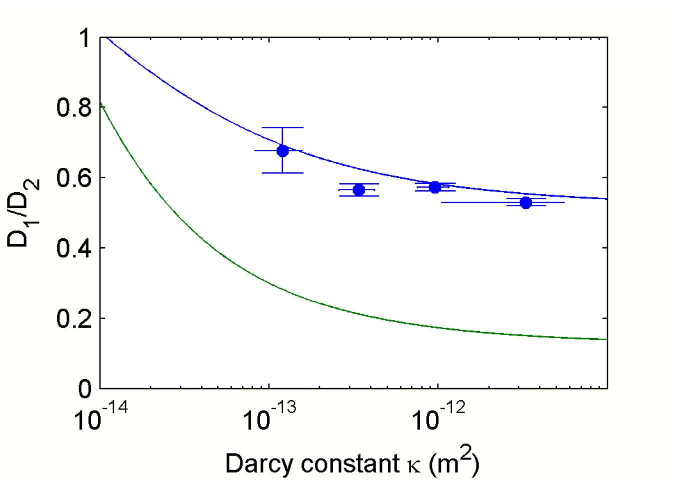

Figure 3.13: The ratio $D_{200\ nm}/D_{500\ nm}$ (dots) agrees well with theory (blue line) and normalizes out D_0, allowing measurement of κ when the solvent viscosity is unknown. However, the sensitivity of this measurement is not good. The ratio $D_{100\ nm}/D_{800\ nm}$ (green line) shows improved sensitivity, but as particle sizes approach 1 μm, steric effects will begin to manifest. This is cause for concern: I have not found theories relating D_{eff} and κ that account for steric effects without requiring additional structural information—namely, ϕ or d_f.

3.3 Discussion

3.3.1 Diffusion and permeability as a measurement of clot structure

Coagulation pharmacy is imminently preoccupied with the effect on clot structure of drugs such as low molecular weight heparin (LMWH), fondaparinux, polyphosphate, and acetylsalicylic acid (aspirin) on clot structure (Collen et al., 2000; Varin et al., 2007; Smith and Morrissey, 2008; He et al., 2009; Ajjan et al., 2009). This interest exists because of clot structure's correlation with various pathologies. However, electron or confocal microscopy of clots is low-throughput and relatively expensive, and not easily reduced to quantitative parameters. By comparison, free particle diffusion generates D_{eff}, a single-parameter indicator of clot structure.

Figure 3.6 shows that particle diffusion is correlated to clot structure over a physiologically relevant range of fibrinogen and thrombin concentrations. Diffusion also resolves structural differences in hemophilic clot structure, demonstrating that the analysis presented in this Chapter addresses physiologically relevant parameter spaces in clotting.

Beyond these qualitative observations, can I establish a quantitative path to determine clot structure from transport measurements, thanks to the $\kappa(\phi, d_f)$ equations of Sections 2.2 and 2.3. Given actual measurements of D_{eff} and κ, the models of diffusion suppression and permeability may be solved and plotted as $d_f(\phi)$. Two such plots—one for a fine clot (small d_f, high fiber number density), and one for a coarse clot (large d_f, low fiber number density)—are shown in Figure 3.14.

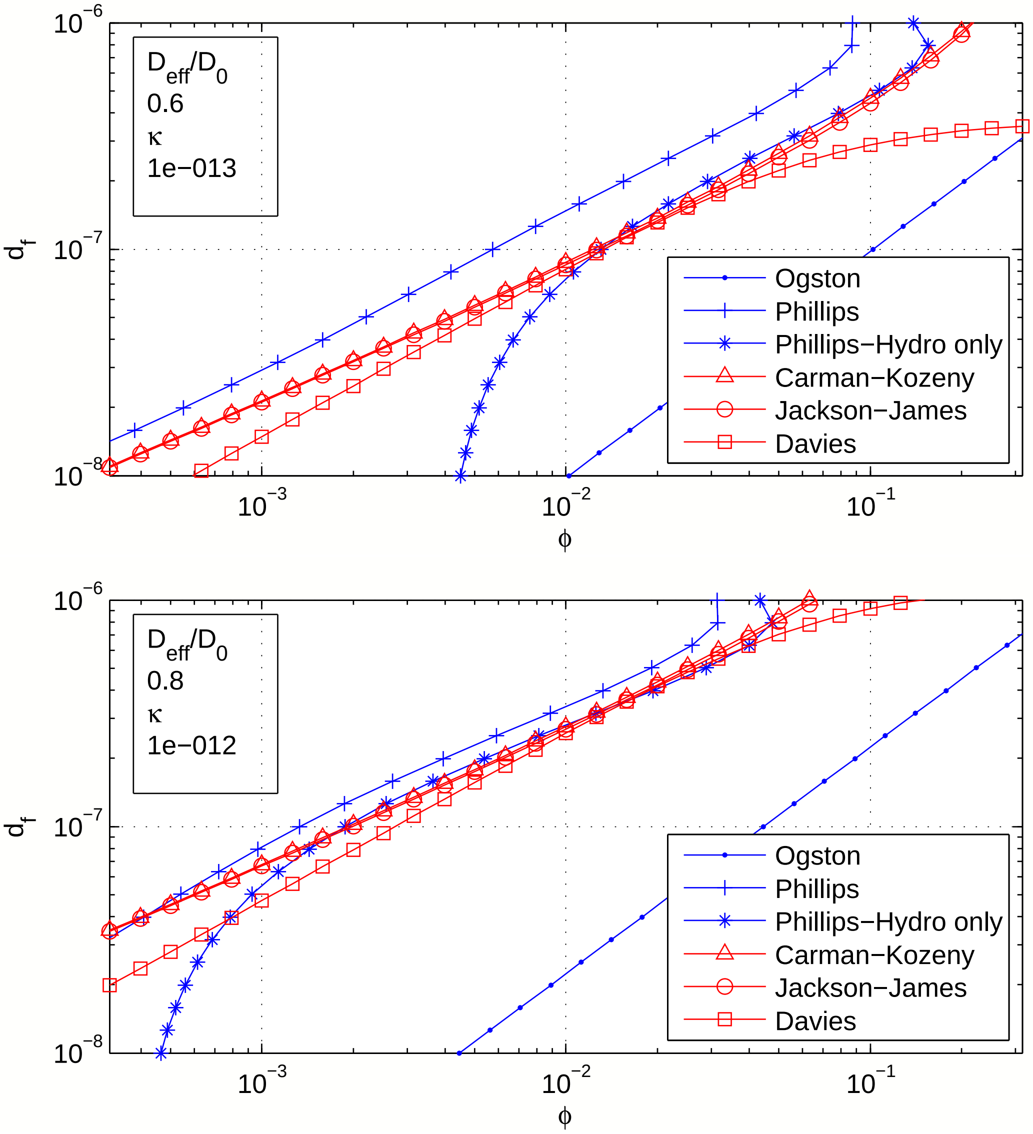

Figure 3.14: Using this Chapter's results for D_{eff} and κ, I have solved each model for $d_f(\phi)$. The theories predicting diffusion suppression are plotted in blue; the theories predicting permeability are plotted in red. The text argues that the Jackson-James, Davies, and hydrodynamics-only version of the Phillips model are correct. Note that only these three models simultaneously intersect in both fine (top chart) and coarse (bottom chart) clots.

This Figure can help us identify which models for $\frac{D_{d_1}}{D_{d_2}}$ and $\kappa(\phi)$ are correct. Note that *somewhere* on each plot there is one point (ϕ_0, d_{f0}) that represents the clot's *true* values of fiber diameter and volume fraction. As shown in Figure 2.7, the models expected to predict fibrin permeability (Jackson-James, Davies, and Carman-Kozeny relations) are all similar to one another in the relevant ranges of ϕ and d_f. Therefore, the true point of gel structure (ϕ_0, d_{f0}) is expected to lie along the area swept out by these lines.

Now consider the models treating diffusion. Because the (purely hydrodynamic) effective medium theory holds, I do not expect the Ogston model, which is completely steric, to be valid in fibrin. Figure 3.14 confirms this expectation: the Ogston model either predicts extremely small fiber diameters (10–20 nm, equivalent to fibers comprising only one or two protofibrils), or extremely large volume fraction (5–10% for 100 nm fibers, a ϕ more consisent with platelet-retracted clots (Diamond, 1999)). The Ogston model also never intersects the Davies and Jackson-James equations, which is consistent with the Ogston Model being inaccurate in this material.

The Phillips model, on the other hand, agrees with the Davies, Jackson-James, and Carman-Kozeny equations to within a factor of 2. Interestingly, ignoring the steric term of the Phillips model (setting $S(f) = 1$) produces a function that agrees with the $\kappa(\phi)$ models precisely at their location of closest approach. The intersection of these three models provides a plausible prediction of d_f and ϕ that uses permeability and diffusion.

This analysis raises two important questions. First, what does it mean to ignore the steric term of the Phillips model, and is this justified? Second, what is the justification for finding fiber diameter and volume fraction in this way, when for decades imaging has been used for the same purpose?

To the first question, steric effects will manifest only if diffusion is measured over timescales long enough to see particle collisions with the gel. Generally speaking, the long-time diffusion of Figure 3.8 shows no variation in diffusion coefficient as a function of τ, however, in the denser clots there is a gradual transition to a lower α for some of the particles. Physical barriers that knock the particle backward (or prevent it from advancing) can create such "sub-diffusive" behavior in $\langle r^2 \rangle$ curves. In these short-time (< 10 s) experiments, therefore, steric effects do not manifest. Using the language of Section 2.1.3, the transition τ to steric diffusion suppression is $\sim$ 1–10 s in high-fibrinogen clots. This result is consistent with the analysis of that Section.

In a lab of infinite resources, the answer to the second question is to do all the measurements. However, should resources be constrained, the technique presented above offers two advantages. Permeability, measured directly or with the prescription of Section 3.2.2, speaks specifically to issues of clot stability. Second, the diffusion and permeability can be measured to arbitrary precision by increasing the volume sampled and decreasing the head pressure, respectively. By contrast, confocal imaging has fundamental precision limitations due to the diffraction limit, and electron microscopy introduces uncertainty due to the required preparation. Therefore, the structure-from-transport method potentially offers greater precision than structure-from-imaging.

3.3.2 Diffusion as a guide for drug design

The results of this work offer insight into the desirable size range of fibrinolytic drugs, particularly with respect to the risk of hemorrhage. There is evidence that single-bolus fibrinolytics have advantages for early-response treatment of thrombosis, but a key risk in such treatment is lysis of hemostatic clots and intracranial hemorrhage (Llevadot, 2001; Giugliano et al., 2001).

The relevance of this work to drug delivery is somewhat subtle. Diffusion is rarely the primary mode of particle transport in an occlusive thrombus. Indeed, in all but the lowest-pressure venous clots, advection dominates fibrinolytic transport into an occlusive thrombus (Diamond and Anand, 1993). However, radial diffusion mediates dismantling of a non-occluding clot (Blinc and Francis, 1996). Furthermore, clots are apparently more dense near the cell surface (Wolberg and Campbell, 2008).

Therefore, there may exist an opportunity to design a nanoparticle fibrinolytic sufficiently small that it efficiently advects through clots, yet sufficiently large that its diffusion is hindered, as shown in the cartoon of Figure 3.15. I hypothesize that such a drug would be subject to advection through an occlusive thrombus, where it would hasten lysis and the restoration of blood flow, yet would be hindered in its lateral transport, reducing fibrinolytic activity and therefore the risk of hemorrhaging. Figure 3.6 suggests that particles as small as 200 nm are within the critical size range to exhibit suppressed diffusion. In denser environments, such as platelet-retracted clots, this range may begin at smaller size.

To operate in this fashion, a drug must advect efficiently, and I have not explicitly

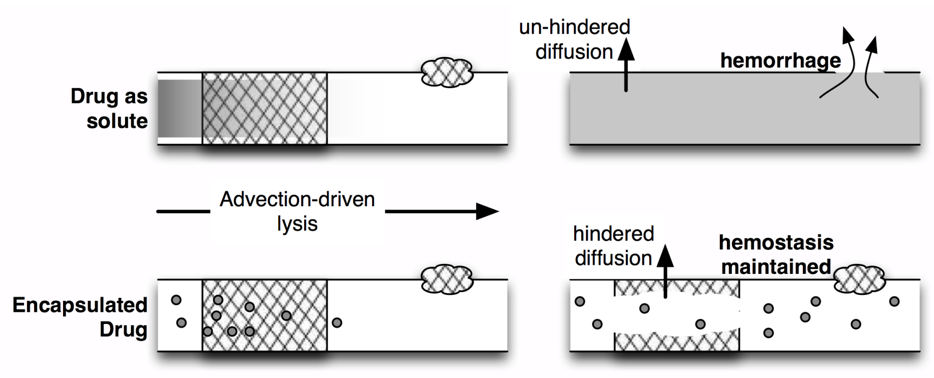

Figure 3.15: Concept for a diffusion-hindered fibrinolytic drug vector near a vessel boundary. An ideal particle would be large enough that its diffusion was hindered, yet small enough that it was not lodged in the fiber matrix, so that fluid flow could drive it down the vessel. This setup would be conducive to destroying occlusive clots, but leaving hemostatic clots intact.

measured advective transport of PEG particles in fibrin. Also, the static PEG particles merit further investigation, as the mechanism that prevents their diffusion is unclear. I further investigate these issues in Section 4.1.

Chapter 4

The Bead's-eye View

The preceding chapters explore the relationship between transport through and structure of fibrin gels. Those results have implications for clinical and research measurements of fibrin and plasma clots. Yet they also raise questions about the local environment experienced by the particles. In this chapter I will discuss additional experiments that help clarify the particles' local physical environment. In particular, I explore the force required to pull stuck particles free, and I determine whether the particles' mechanical environment carries information about the bulk elasticity of the gel.

4.1 Stuck particles

How stuck are the stuck particles—or, what force is required to pull them free? This is a key question for issues of drug delivery, as mentioned in Chapter 3. The relevant force range is determined by physiology, particularly by whether the flow of blood would exert sufficient force to avoid association of the particle with the gels.

I have used a Multiforce High Throughput System (Spero et al., 2008) to force PEG-coated magnetic particles through the gel. The experiment is summarized in Figure 4.1. Briefly, clots of fibrinogen concentrations 0.5–3 mg/mL were prepared (see Section 3.1), and plated into a magnetic microplate using the protocol of the above reference. Super-paramagnetic 2.8 μm particles with both PEG and carboxylate (COOH) surface chemistry were subjected to three force pulses that lasted 3 s each.

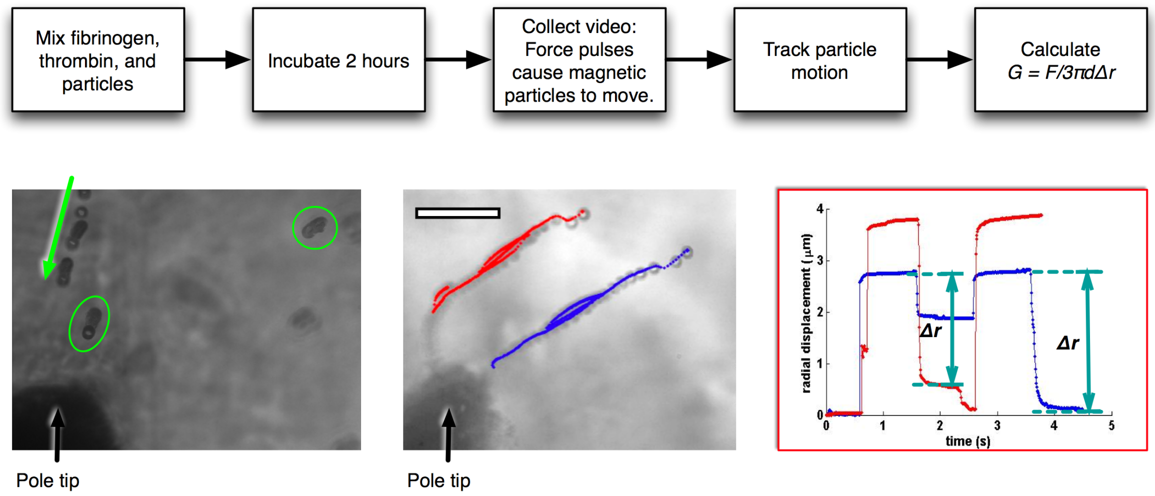

Figure 4.1: Top: experimental protocol for magnetic manipulation of 2.8 μm particles. Clot types tested were 0.5, 1, and 3 mg/mL fibrinogen with 10 nM thrombin. Bottom left: time lapse (minimum intensity projection) image of a typical PEG particle pulling experiment. Some particles oscillate back and forth (green ovals) while others jump long distances through the mesh, often coming into the field of view from far away. Bottom middle: particle tracking is performed with CISMM Video Spot Tracker except where otherwise noted. Scale bar in video image is 20 μm. Bottom right: radial displacement, $r(t)$, is shown plotted for two particles in fibrin. The quantity Δr, used in the section on fibrin elasticity, comes from the particle recovery after the magnets are turned off.

The motion of PEG and COOH particles is plotted in Figure 4.2. Because COOH particles stick to fibrin, they oscillate back and forth as the force is turned on and off, but ultimately travel short distances (0–26 μm). Some PEG particles, by contrast, can jump through the matrix of the gel, traveling more than 65 μm in even the least permeable clots. Many PEG particles traveled all the way across the field of view to collide with the pole tip. Due to the erratic motion of the pulls, videos were decimated from 120 Hz to 4 Hz so that I could hand-track them using ImageJ.

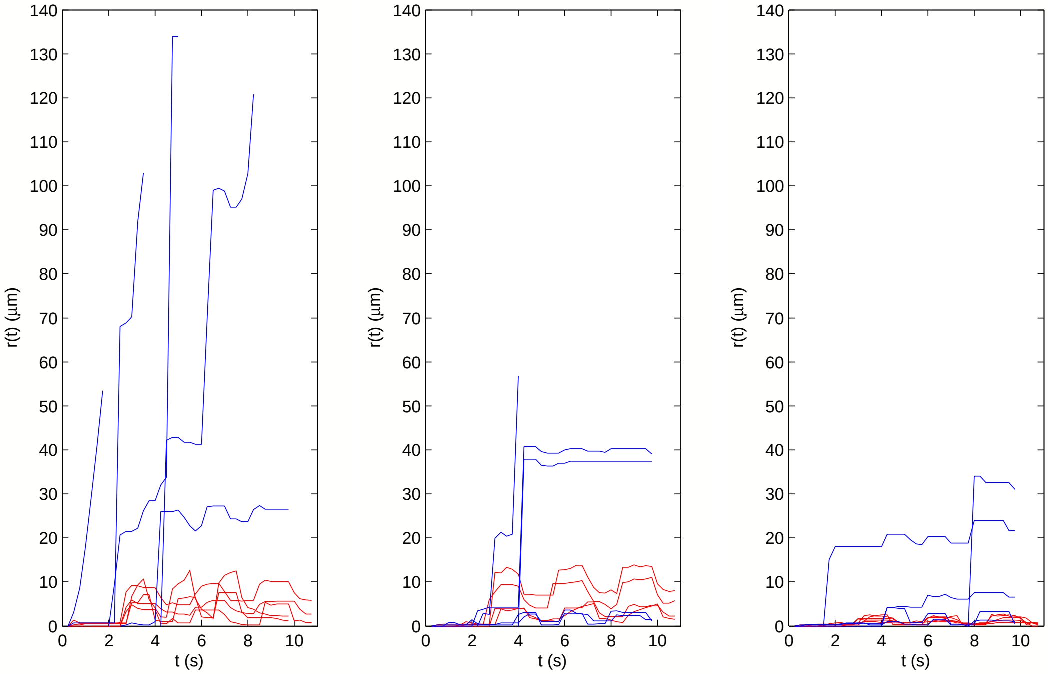

Figure 4.2: Particle trajectories $r(t)$ for PEG (blue) and COOH (red) particles in clots of increasing fibrinogen concentration: $0.5\ ^{mg}/_{mL}$ (left), $1\ ^{mg}/_{mL}$ (middle), and $3\ ^{mg}/_{mL}$ (right). All clots were formed with 10 nM thrombin. Magnets were degaussed, then pulsed three times (on for 1.5 s, off for 1.5 s). PEG particles clearly move farther than COOH particles, frequently jumping through the mesh. Many PEG particle tracks end early because the particles collide with the pole tip. Due to the erratic motion of the pulls, videos were decimated from 120 frames/s to 4 frames/s then hand-tracked. Therefore, the resolution is severely degraded, and pulls from different videos do not cleanly align with one another.

The net travel of PEG particles as compared with COOH particles are shown in shown in Figure 4.3. The mean distances traveled by PEG particles as reported in Figure 4.3 are lower bounds, because 31% (fine clots) to 44% (coarse clots) of particles entered the field of view from offscreen while the forces were being applied. By contrast, no COOH particles enter the field of view during the pulling except in the coarsest clots, in which 11% of particles entered from offscreen. The force applied to particles at the pole tip was 2 nN; at the edge of the field of view (~ 150 μm from the pole tip) the force was 0.1 nN; the force exerted on particles offscreen was less than 100 pN.

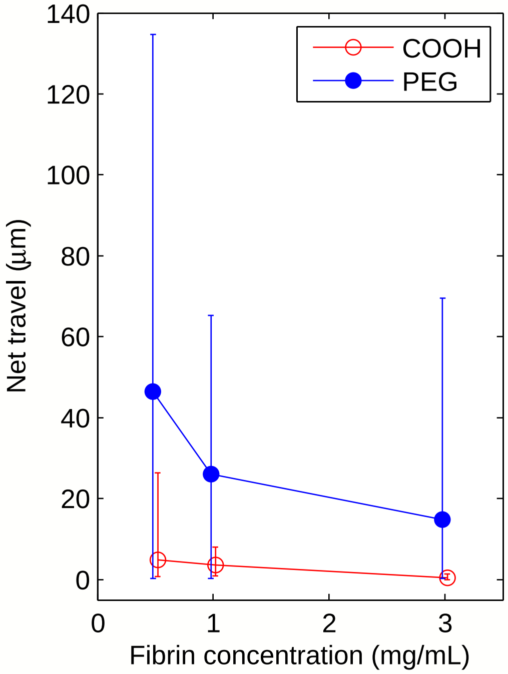

Figure 4.3: Net displacement of 2.8 μm PEG particles (dots) and COOH particles (circles) after three pulses of 1 second each. Points show mean displacement; bars show minimum and maximum displacement. Number of COOH particles N = 9, 10, 11 and number of PEG particles N = 39, 10, 13 for 0.5, 1, and 3 $^{mg}/_{mL}$ fibrinogen, respectively.

The heterogeneity of particle environments is responsible for the broad range of particle motion in Figure 4.3: some particles are easy to pull free, others are not.

However, large forces were not always required—indeed, the particles that traveled furthest started the greatest distance from the pole tip, and therefore experienced the smallest force. Forces < 100 pN (the force at the edge of the field of view) are adequate to drive PEGylated 2.8 μm particles long distances in these gels. A particle in water experiences this force at a flow rate of $v < 4$ cm$/s$. The higher viscosity of blood would further reduce the required flow rate. Arterial flow rates are about 75–110 mL/min (Knaapen et al., 2009), which for a typical artery lumen diameter of 4 mm (Dodge et al., 1992) corresponds to a fluid velocity of 10–15 cm/s. This result suggests that whatever the reason for the association between stuck PEG particles and fibrin, freely flowing blood may be able to prevent it from developing.

At this stage the mechanism of particle sticking remains unknown. However, I can speculate on the responsible phenomena. The moderate forces required to pull stuck PEG particles free suggests that there are no strong chemical associations between the particles and the fibrin. The entrapment may be purely mechanical, with particles captured among strands of fibrin. Physical entrapment is consistent with the result that larger particles diffuse less.

Particles might also stick to fibrin fibers because of depletion flocculation, an entropic effect where small solutes cause large colloids to aggregate. Depletion flocculation has been proposed as a mechanism for lateral aggregation of fibrin fibers (Gelder et al., 1996). Also, the higher concentration of macromolecules in PPP clots (the same ones responsible for raising plasma's background viscosity) could act as a crowding agent, explaining the observation that the percentage of static particles was higher in plasma clots than in purified gels.

4.2 Fibrin elasticity

Although this dissertation has focused primarily on transport, fibrin elasticity is also an important clot property. Clots form an essentially mechanical function—stemming the flow of blood—and it is well established that clot stiffness varies with clot structure (Ryan et al., 1999) and with risk of heart disease (Fatah et al., 1996). Clot rheometry is even used as a clinical diagnostic, in a cup-and-bob geometry often called thromboelastography (Evans et al., 2008).

The systems of Chapter 5 are well designed for high throughput characterization of fibrin clot stiffness. From Mason and Weitz (Mason and Weitz, 1995) to Crocker *et al* (Crocker et al., 2000) to Meehan and Cribb (Meehan et al., 2010), much work has been done to identify conditions under which the bulk viscoelastic properties of polymer media can be measured by nanoparticles. Magnetic microbead rheometry has even been used to measure clot stiffness during gel formation (Ajjan et al., 2008). Yet it remains unknown whether micro-scale techniques measure the same elastic modulus of fibrin as conventional macro-scale techniques such as cone-and-plate (CAP).

I have checked for this correspondence by comparing the data from Section 4.1 against cone-and-plate (CAP) results. To extract a storage modulus from the $r(t)$ results discussed above, I calculated $J(t) = 3\pi d r(t)/F$ (Ziemann et al., 1994). The data are plotted against strain, defined for driven micro-rheometry as $\gamma = 3\Delta r d$ (Cribb, 2010). To measure bulk G, clots were similarly prepared, except in 300 μL volumes, then loaded into a rheometer with a 1° cone. Recovery compliance was measured at four different initial strains. The results of both CAP and MHTS measurements are shown in Figure 4.4.

Figure 4.4 indicates that microrheometry does not measure bulk fibrin elasticity, because the MHTS data do not overlap the CAP results. For MHTS measurements (dots), I subjected particles in all three types of clots to a fixed range of forces, so the strain is greater in clots of low fibrinogen concentration. As fibrinogen concentration increases, the strain reduces, while the measured stiffness increases. Because the CAP can be operated in a strain-controlled fashion, those results (lines) show strain stiffening, a well-established characteristic of fibrin gels (Janmey et al., 1983). Higher strain measurements were not feasible in this geometry, because the gel pulled loose from the rheometer plate. At all concentrations, magnetic microrheometry under-predicts the bulk storage modulus.

The reason for this disagreement would seem to be that the particles are not large enough. In the limit of a very large (say, 1 cm) particle, one would expect complete agreement with macroscopic data, because, barring some unanticipated anisotropy, an applied stress of any geometry at a length scale comparable to that of the CAP should measure similar mechanical properties. By contrast, to judge from the confocals of Figure 2.2, a 2.8 μm particle could potentially be touching only one fiber at a time. In this situation, one would expect the micro-rheometry measurement to be lower than the bulk measurement, because the act of pulling on one fiber would be analagous to pulling on a single spring, while the act of pulling on the whole gel would be analogous to pulling on many springs in parallel; the latter case represents a stiffer material. If this hypothesis is correct, particles larger than the mesh size of the material—say, $> 10\ \mu$m—should measure bulk viscoelastic properties of fibrin. (Unfortunately, particles of sufficient magnetic loading are not available in that size.) In fact, the required size is somewhat larger; the reason for this is left to the detailed discussion of Section 5.4.2.

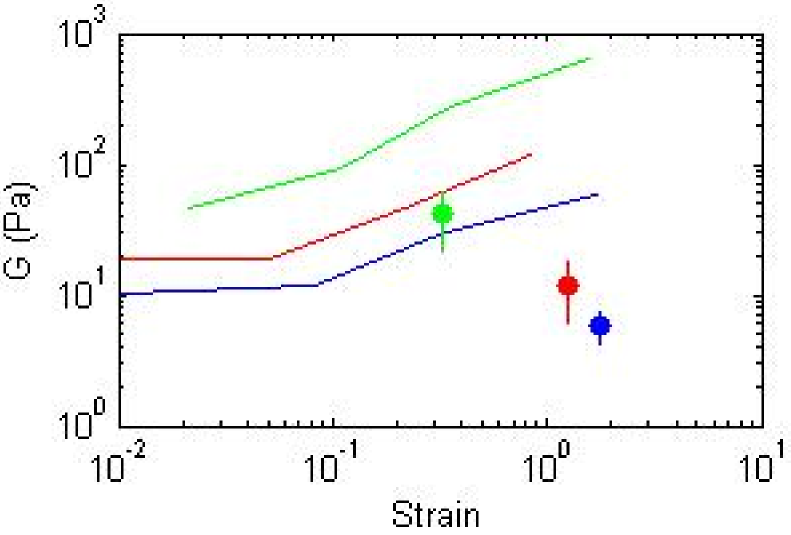

Figure 4.4: Storage modulus, measured by cone-and-plate (lines) and driven 4.5μm particles in the MHTS (circles). Clot types were 0.5 mg/mL (blue), 1 mg/mL (red), and 3 mg/mL (green) fibrinogen mixed with 10 nM thrombin.

Figure 4.4 does confirm that the MHTS can resolve the differences in elasticity among the three clot types, demonstrating its potential as a high throughput platform for evaluating the mechanical properties of clots. The measurement can be performed during the formation of the clot, producing a stiffness vs. time curve, shown in Figure 4.5 that may be adequate as a high-throughput counterpart to the clinically tested technique of thromboelastography. However, additional work remains to develop this assay. The fact that G continues to rise after the clot finishes forming (Figure 3.5 shows that polymerization for this type of clot finishes in under 20 minutes) suggests that the measurement is altering the gel, perhaps dragging the particle forward, piling material in front of it. Examination of the full "tuning fork" profile of G(t)—in which plasma is allowed to move through the whole process of clot formation and lysis—will be an additional step in developing this technique.

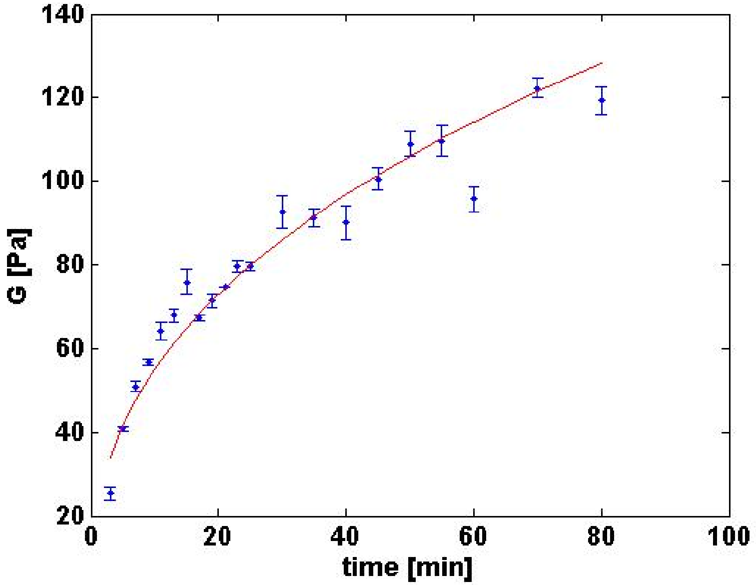

Figure 4.5: Storage modulus in 1 mg/mL fibrinogen, 10 nM thrombin measured over the course of the gel formation. The fact that G continues to rise after the clot finishes forming suggests that the measurement is not adequately developed; perhaps the particle is being dragged forward.

4.3 Future Directions

The diffusion and magnetic microrheometry measurements made in this dissertation have elucidated some of the specific phenomena relevant to particle transport in clots. It has also opened new areas for inquiry, particularly regarding the dynamics of stuck particles and the design of drug delivery vectors.

A new platform is required to fully characterize particle adhesion for vascular drug delivery, one that can simultaneously measure clot permeability, particle diffusion, and clot structure. A platform that better captures the geometry of a blood vessel is also desirable. Figure 4.6 presents a flowcell concept drawing that addresses these needs. The design of this device offers several benefits over a traditional permeability measurement. First, it is flow-controlled, meaning it can measure permeability at a much wider range of flow rates than practically achievable by gravity-driven (pressure-controlled) flow. Second, it provides a "four-point" measurement of flow resistance (analogous to the traditional four-point electronics measurement), eliminating errors due to the resistance of the rest of the flow system. Third, the system is compatible with high-NA microscopy, allowing permeability to be determined simultaneously with clot structure, fiber deformation under flow, and particle diffusion and advection.

4.4 Conclusions

Chapter 3 demonstrated that the local environment of nano-particles in fibrin appears to be purely hydrodynamic for freely diffusing nanoparticles. In this Chapter I

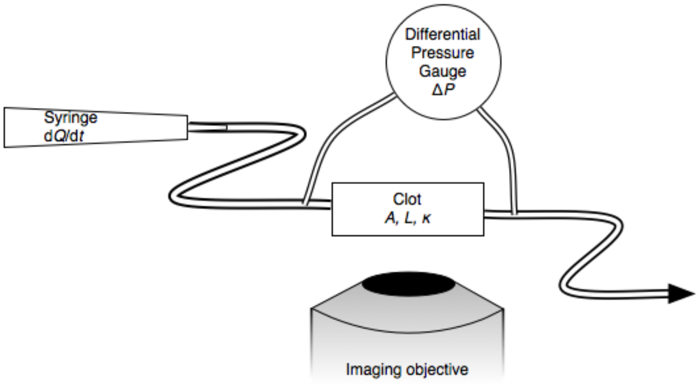

Figure 4.6: Schematic of a flowcell for measuring diffusion, particle-fibrin dynamics, and permeability. A syringe pump controls $\dot{Q}$, forcing a fluid with viscosity η through a clot with dimensions $A \times L$ and unknown permeability κ. The differential pressure gauge supplies ΔP, which provides the final required quantity to calculate κ from Equation 2.14. Using a microfluidic chamber for the clot permits high-NA microscopy of particles inside the clot.

demonstrated that larger (micro-scale) PEG-functionalized particles, though immobile, appear to be only loosely associated with the gel, suggesting that gravity, depletion interaction, or very weak chemical interactions are responsible for the existence of stuck particles.

I have also compared the elastic modulus of fibrin at the micro and macro length scales. Because micro-sized particles are on the order of, or smaller than the spacing between fibers, driven microrheology in the MHTS does not measure the bulk elasticity of the gel. However, the measurement does reveal the time-dependent stiffening of the gel during clot formation, and may therefore serve as a high throughput, small specimen volume replacement for thromboelastography.

Chapter 5

Toward High Throughput

My results have implications for coagulation research and drug design. But these experiments' long-term utility will be determined as much by the operational difficulty of making the measurement as by the scientific questions at hand. In this Chapter I present novel instrumentation for high-throughput characterization of clot transport and mechanics. These systems are a high throughput "multiscope" and a microplate-based force application system for biophysical experiments.

Biophysical experiments include more than diffusion and driven microrheology of fibrin. The systems presented in this Chapter are designed to accelerate data acquisition and processing for a wide range of measurements, including passive and driven microrheology of fibrin, mucus, DNA, extracellular matrix, and other polymers; single cell mechanics; cell migration and cytometry; and cell-substrate interaction using microscale post arrays.

Transitioning any of these experiments to high throughput would require automated microscopy, commonly called high content screening (HCS). The essential task in this growing field is to take more images, faster, with less human intervention. The benefits are evident in the wide range of results being acquired with HCS systems. These include results on the proteins (Shen et al., 2006) and genes (Simpson et al., 2008) involved in cell migration. Recent work used siRNA knockdown to identify every gene relevant to cell division (Neumann et al., 2010). High content cell screening is increasingly critical for drug discovery (Lang et al., 2006).

The benefit of an HCS system for the experiments in this dissertation are also apparent. The fibrin diffusion experiments of Chapter 3 used 10 minutes of video per specimen, assuming five videos per clot and two clots per preparation. The total from eight specimens and two bead sizes—using 32 wells in a microplate—is nearly three hours of video. Yet eight specimens is a tiny fraction of the parameter space we would ideally hope to explore. Consider the human genome siRNA study of genes involved in cell division, and consider a similar knockdown of the genes involved in clot formation above cells, using recent experiments (Wolberg and Campbell, 2008) as a template. One diffusion measurement would be required to test each gene (roughly 21,000) at each particle size (at least 2), against a range of clot types (perhaps 4 donors' worth of healthy plasma). This experiment alone represents 420 mL of plasma per donor (assuming 20 μL of plasma per well), and 168,000 measurements of D_{eff}. At 10 minutes of video per measurement, the experiment would last 28,000 hours, or 3.2 years, running day and night. Clearly, an automated, highly parallel system would be required.

While HCS has improved throughput for cell imaging, it has left microrheology behind. This is unfortunate, as microrheology shows promise as a tool for scientific and industrial high throughput screening (Breedveld and Pine, 2003). However, the specifications for a microrheology instrument are different in key ways. First, high bandwidth video is desirable to capture dynamic phenomena. Second, the specimens are not planar, because the particles are distributed through the material volume.

These specifications are not met by the various commercial HCS systems for imaging cytometry. The manufacturers (Beckman Coulter, GE, Perkin Elmer, Roche, and Thermo) provide software designed for snapshots, rather than high framerate (> 10 Hz) video microscopy. Their autofocus routines are designed to identify planar specimens. Their image processing software typically excels at cytometry (measuring cell area, circularity, migration), but lacks high-precision, automated particle tracking capability. These design decisions make existing HCS systems impractical for microrheology.

These systems' hardware designs also place limitations on experiments—both in cell imaging and microrheology—that are undesirable. They are not compatible (in hardware or software) with force application systems, including our magnetic microplate-based design (Spero et al., 2008). Also, the systems are all essentially a traditional microscope over which the specimen is systematically translated. Therefore, the length of an experiment in such a system can never be shorter than the product Nt_i, where N is the number of specimens and t_i is the time to acquire data from each specimen. In addition, the single-microscope design is incompatible with simultaneously imaging multiple wells, which may be desirable for recording dynamic phenomena such as time-dependent microrheology or cell migration; even if simultaneous imaging is not required, for any non-stationary process, the maximum sample rate is $1/Nt_i$.

To address these issues, I have collaborated with a team of scientists and engineers to design, develop, and qualify a microscope with multiple objectives that is also compatible with the MHTS. A “multiscope,” using m objectives, could shorten the experiment time to Nt_i/m, and increase the specimen sampling rate to m/Nt_i. With m = 12, the high throughput clotting experiment mentioned above, for example, would collapse from 3.2 years to 97 days, or about 3.3 months. The name of this multiscope project is “Panoptes,” after the never-sleeping, hundred-eyed god of Greek myth (Rose, 2001).

5.1 Panoptes: High Throughput Video Acquisition

Panoptes is envisioned as an array of microscopes, each fitting within a 1.8x2.8 cm footprint, allowing simultaneous imaging of up to 12 wells in a standard 96-specimen microplate. It is designed primarily to collect data for three client experiments: nano- and micro-particle diffusion (as in Chapter 3), image cytometry, and driven particle rheology in the MHTS (as in Chapter 4 and discussed in Section 5.3).

These experiments define Panoptes’s critical functionality:

1. Ability to resolve cells and nuclei. Image quality above this threshold is desirable.

2. Transmission brightfield and one or more channel of widefield epifluorescence.

3. Adequate signal-to-noise for client experiments, discussed in Section 5.1.3

5.1.1 Image quality: NA and z-focus

The quality of Panoptes' objectives will define the maximum potential imaging quality of the system. Numerical aperture (NA) is the parameter that defines the fundamental limit of a system's optical resolution; inexpensive objectives ($<$ \$500) with an NA above 0.7 are widely available. Unfortunately, higher NA also means a tighter depth-of-field, and as a result, greater sensitivity to tilt or curvature in the well plate. Therefore, we desire independent focus control for each microscope.

The traditional approach to z-focus is to mechanically translate the objective. While micro-manipulators of sufficient precision exist, they are expensive, starting at $>$ \$500, even before placing serious constraints on slew rate, backlash, mechanical smoothness, or package size. This coupled with our desire for high NA (and tight depth-of-field) would lead to a slow auto-focusing routine. Indeed, autofocus speed is well established in the field as a limiting parameter for experiment throughput. The speed is determined by both the algorithm and the time required to collect the data. The algorithm may be accelerated by creating a dedicated auto-focusing circuit (Bravo-Zanoguera et al., 1998), but this is costly and reduces the variety of algorithms (or autofocus targets) supported. Image acquisition time is limited by the required light collection, which is minimized when imaging in a bright mode such as phase contrast (Price and Gough, 1994). Image acquisition can also be accelerated by enabling continuous scanning during image acquisition (Bravo-Zanoguera et al., 2007). However, quantifying the speed of auto-focus alone can be distracting. The ultimate metric of throughput is the number of datapoints collected per unit time: for example, image cytometry is often quantified in cells imaged per hour. The state of the art for image cytometry systems is currently 100–1,000 cells per second, depending on the resolution and magnification of the system (Varga et al., 2009).

In Panoptes, we are pursuing a novel z-focus strategy. We have employed an electrowettable liquid lens (Hendriks et al., 2005). This technology uses immiscible fluids of different refractive indices, contained in a chamber whose wet-ability varies with voltage, to form an electronically controllable lens. The only commercially available liquid lens is the Varioptic Arctic 416. I am indebted to L. Vicci for her work mounting a Varioptic lens inside of an off-the-shelf 40x, NA 0.7 objective, creating an objective with electronic control of the object plane. The lens has a fast focusing response time (< 100 ms peak-to-peak), varies focus from 0–350 μm into water, and is mechanically silent. However, the Varioptic lens is NA-limiting, as its 2.4 mm aperture is the smallest in the optical system. This begs the question: why sacrifice NA for a focusing technology that was supposed to support high NA microscopy?

I offer two reasons. First, the Varioptic lens allows faster focusing than any other strategy. While the peak-to-peak response is 100 ms, the bandwidth of the control signal is about 10 ms, so for small voltage changes, the z-response may be much faster, suggesting we may be able to refocus the objective between successive frames. In this case, the data-stream for the autofocusing algorithm could be 3-dimensional, allowing algorithms that find parameters of whole image stacks, rather than individual slices (*e.g.*, net image intensity or the standard deviation of the intensity distribution). Such stack-based autofocus might be more computationally efficient than existing algorithms.

Second, the liquid lenses are a young technology. It is plausible that larger aperture lenses will become available over time. It is a strategic decision to develop Panoptes around the assumption of a voltage-controlled z-focus, with the expectation that improved imaging will become feasible in the future. Indeed, a larger aperture liquid lens is sufficiently desirable that future development plans could include designing such a component in-house.

I must also stress two important caveats in the use of a tunable lens element. First, the liquid surface used for lensing is spherical; this necessarily introduces spherical aberration as the lens power increases. The only way to correct this aberration is with other tunable lenses, leading to a custom-designed objective of tunable lens elements. Second, changing the objective's focal length[1] without adjusting its tube length[2] will lead to a change in magnification[3]. The solution to this issue is to build a look-up table for magnification as a function of lens state.

5.1.2 Imaging modes: brightfield and fluorescence

Fluorescence is used as a marker of gene expression or cell function. It also provides the highest-contrast mode to image sub-micron particles in experiments such as those of Chapter 3. Brightfield illumination proves ideal for experiments involving magnetics and particles where $d > 1$ μm, as it is provides high contrast images of the pole tip and magnetic particles. Furthermore, brightfield is not light-limited, making it the prefered

---

[1] focal length: distance between the objective and the specimen plane

[2] tube length: distance between the objective and camera

[3] Magnification: ratio of object distance to image distance, $M = z_o/z_i$

choice for capturing high-bandwidth phenomena. In this Section I discuss the design and validation of Panoptes's fluorescence and brightfield optical trains[4].

Figure 5.1 shows Panoptes's optical path, which provides Khöler illumination for both transmission brightfield and single-channel epifluorescence. All components of this optical train are small enough to be arrayed in a multiscope system. A detailed bill of materials is provided in Appendix B.

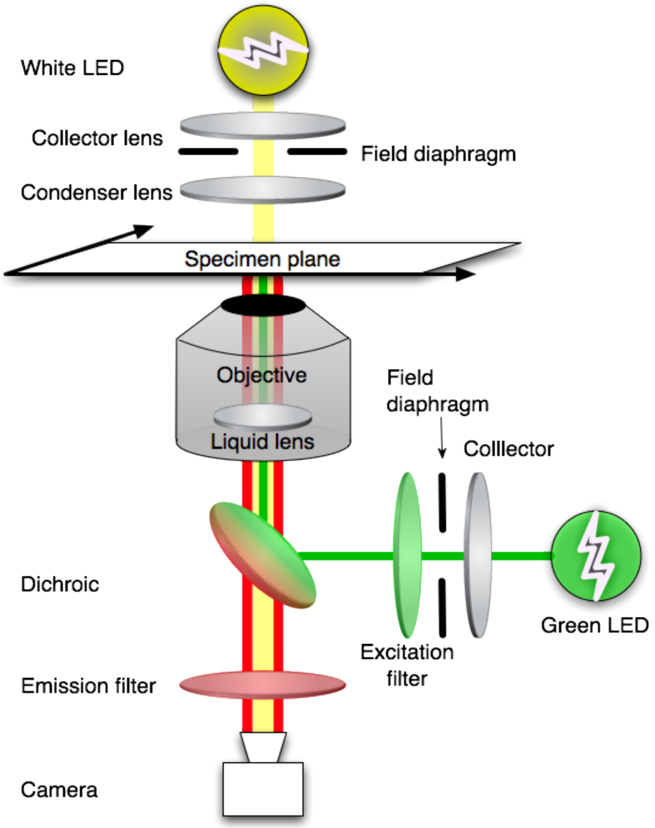

Figure 5.1: Panoptes optical path. The system supports transmission brightfield and epifluorescence.

---

[4] I am indebted to Jeffery Cohen, who contributed to the work of this Section

5.1.2.1 Single-channel widefield epifluorescence design

For epifluorescence, the condenser lens is also the imaging objective, and therefore the back focal plane is not usually known. However, an image at a lens's back focal plane corresponds to a conjugate image at infinity in front of the lens. Therefore, we can conveniently verify that we have achieved Khöler illumination by projecting the image of the LED onto a screen placed at the objective's far-field. The optimal collector lens selection and position would ensure that the image of the LED at the objective's back focal plane is small enough to fit within the Varioptic lens aperture, and that the solid angle collected from the LED captures as much light as possible.

Figure 5.2 helps clarify which adjustments can be made to optimize the fluorescence illumination. Consider the objective location to be fixed. It is best to keep the collector lens close to the objective, to minimize the magnification of the LED; the minimum separation is set by the physical size of the objective and the need to place a dichroic between these two elements. Reducing the collector lens aperture can improve contrast by reducing the illumination intensity above and below the imaging plane while preserving the illumination intensity across the field of view. However, the smaller the aperture, the smaller the solid angle collected from the LED, which reduces the overall intensity and therefore the overall signal. The LED is moved into the correct position behind the collector to achieve a focus at infinity on the far side of the objective.

To obtain the best possible illumination field, a small aperture, short focal length collector lens is desirable, allowing minimum separation between the LED, collector, and the objective. This maximizes contrast, maximizes the captured solid angle of

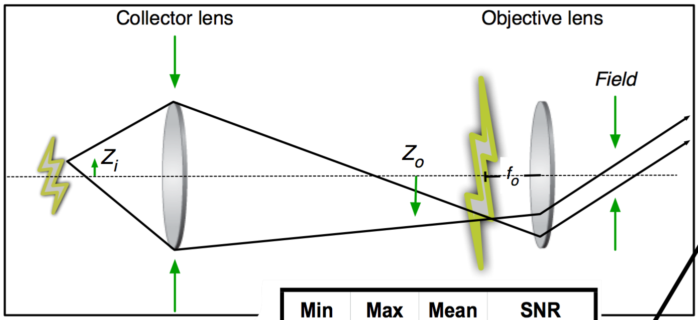

Aperture Test	Min	Max	Mean	SNR (Max:Avg)
5mm Aperture	0	199	5	44
4mm Aperture	0	196	4	48
3mm Aperture	0	194	4	53
2mm Aperture	0	156	3	51
1mm Aperture	0	38	3	13
Filters Test				
All Filters	0	208	5	39
No Emission	182	206	189	1
No Excitation	34	216	47	5
Controls				
All Filters - No Sample	0	11	1	9
All Filters - Blank Cover Slip	0	11	1	9
All Filters - No Light	0	11	1	9
No Ex. Filter - No Sample	0	23	7	3
No Ex. Filter - Blank Glass	1	35	17	2
No Ex. Filter - No Light	0	11	1	9

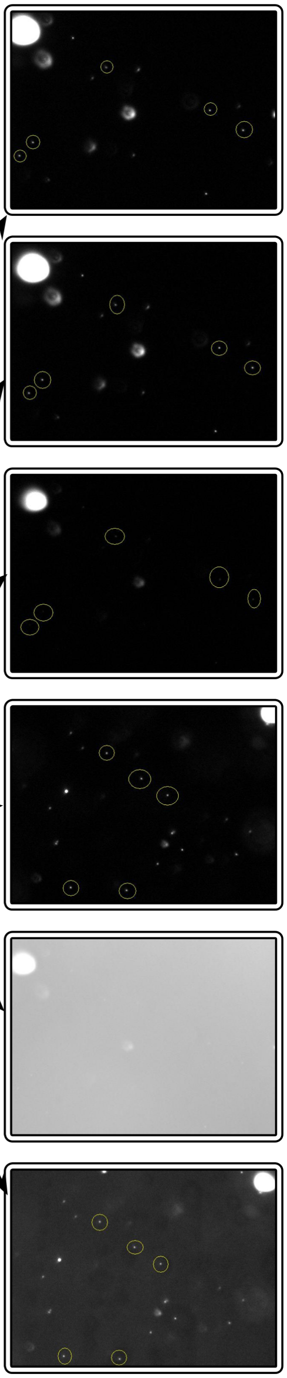

Figure 5.2: Top left: optics schematic for Panotes's epifluorescence illumination train. Bottom left: Results for contrast measurements of fluorescent particles. Reducing the collector lens aperture improves the contrast of the fluorescence signal by decreasing the illumination field, and the imaging quality is far superior when all fluorescence filters are installed. Right: Sample images showing regions where min, max, and average pixel values were calculated.

light from the LED, and minimizes overfilling of the back-aperture of the objective. Currently, we are using an LED with an emitting diameter of 0.5 mm and half-cone angle emission of 80°, and a collector lens with an aperture of 15 mm and a focal length f of 12 mm. To measure the contrast of this illumination arrangement, line scans of 200 and 500 nm particles were compared with and without a 4 mm aperture in front of the collector lens. The data are shown in Figure 5.2. As anticipated, reducing the collector lens aperture improves the contrast, at the expense of the total fluorescence signal. In the next build of Panoptes, we will have a custom-cut dichroic that will allow a shorter total optical path, and permit us to capture more solid angle from the LED, while still improving image contrast.

5.1.2.2 Brightfield design

For brightfield, the condenser lens must focus light through the MHTS magnetics block, which places a lower bound on its focal length (16 mm) and, thanks to the 1/8" annulus, an upper bound on its NA (0.21). The images shown below use 1" optics; we have deferred selection of final illumination optics until after the construction of the inverted microscope. However, a wide range of LEDs and inexpensive, injection-molded lenses are available.

We have chosen to not pursue phase contrast microscopy in this design, but I will note that an interference imaging mode would be a minor modification to this design. The traditional phase contrast microscope uses an amplitude mask on the illumination side and a phase mask behind the imaging objective; newer approaches use so-called "common-path" interference, where all the phase filtering is handled entirely behind the objective (Glückstad and Palima, 2009). The latter approach is recommended in this application for two reasons. First, it relies on NA= 0 illumination, which is convenient, given the low-NA limit placed by the MHTS block. Second, the phase arrangement can be placed entirely behind the microscope camera, increasing design flexibility, and suggesting a modular approach where phase filtering need not always be applied.

5.1.3 Image quality and particle tracking signal-to-noise

It is a natural first step to qualitatively evaluate the imaging of familiar specimens. Figure 5.3 shows ovarian cancer cells in both brightfield and fluorescence. The cells' and particles' locations and shapes can be easily identified. Fluorescence appears to provide better contrast but less detail, particularly in the interior of the cells.

In its envisioned operating modes, however, Panoptes's video output will be viewed rarely. More common will be the extraction of particle trajectories from the video. The quantity $\langle r^2 \rangle$ of particles on a rigid substrate is the noise floor for diffusion experiment and provides insight into the tracking resolution. Figure 5.4 shows the noise floor measured for particles on glass, with a flat, or non-scattering background. It is important to note that particles viewed over cells, through mucus, or in other scattering environments would have a higher noise floor.

Fluorescence is particularly useful for minimizing the noise from scattering environments. For this reason, I take the fluorescence noise floor as the standard by which to measure Panoptes's promise for particle tracking. Figure 5.4 compares these noise

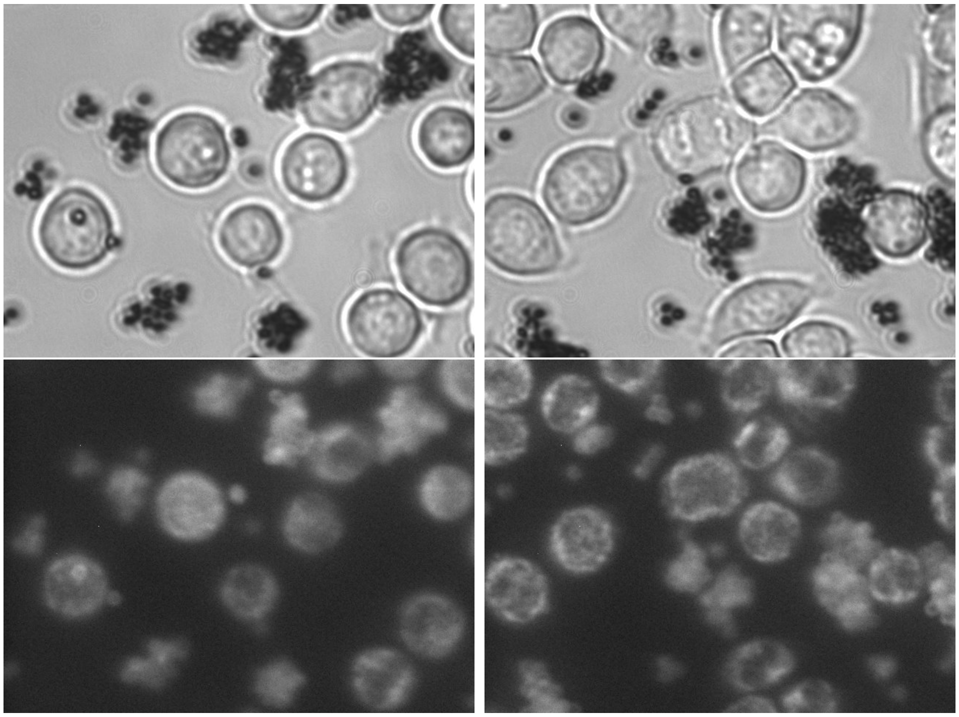

Figure 5.3: Mitotracker red-stained ovarian cancer cells with 2.8 μm magnetic particles in Panoptes. The cells' and particles' locations and shapes can be easily identified. The particles are clearly differentiable from the cells in brightfield, but not fluorescence. Some cell texture is adequately resolved, including the chromosomes of one cell in anaphase in the upper right image.

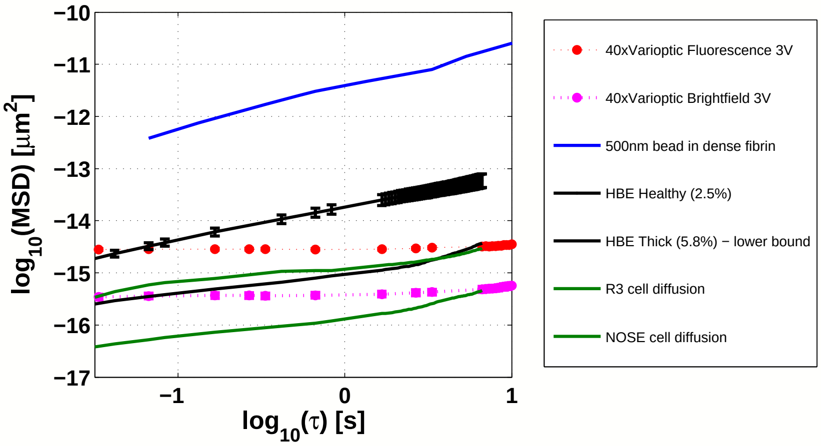

Figure 5.4: Panoptes noise characterization. The brightfield line (magenta) suggests ability to resolve 20 nm excursions; the fluorescence line (red) suggests the ability to measure 50 nm excursions. These noise floors are valid at 10 ms $< \tau <$ 10 s.

floors with three types of diffusion experiments: the fibrin diffusion experiments of Chapter 2, passive mucus microrheology, and diffusion of particles on cells. Fibrin experiments clearly avoid the noise floor, implying that if Panoptes can see 500 nm particles, then the particles can be accurately tracked. CF-like (5.8% solids pig gastrine) mucus can be below the fluorescence noise floor until $\tau = 10$ s; therefore, long data acquisition times at low framerate (~ 10 minutes) are required to get good statistics (two decades beyond the τ used) for the calculation of $\langle r^2 \rangle$. Cell diffusion is clearly below Panoptes's tracking resolution.

Figure 5.4 provides insight into other potential experiments. The noise floor of $\langle r^2 \rangle = 10^{-14.3}$ m^2 implies typical excursions ~ 100 nm. This helps identify whether Panoptes can be used for experiments in addition to diffusion. For example, typical cell compliance and fibrin elasticity measurements involve particle excursions of > 100 nm, indicating a signal-to-noise of at least 2 for fluorescence imaging. The signal-to-noise of mucus viscometry, by contrast, is limited primarily by data acquisition time, because pulling longer will always make the particles move farther. Figure 5.5 summarizes these observations, along with signal-to-noise values for diffusion experiments.

The Panoptes prototype enables a fully high throughput diffusion experiment. I have used this optics train, along with control software developed by R. Schubert, to automatically acquire diffusion data from plated fibrin clots. Automation relieves the technician of book-keeping burdens, so acquiring data in more fields of view for shorter periods of time becomes the preferred strategy. For example, 15 seconds of video in 10 fields of view might be captured in each well. If two wells are used for each type of

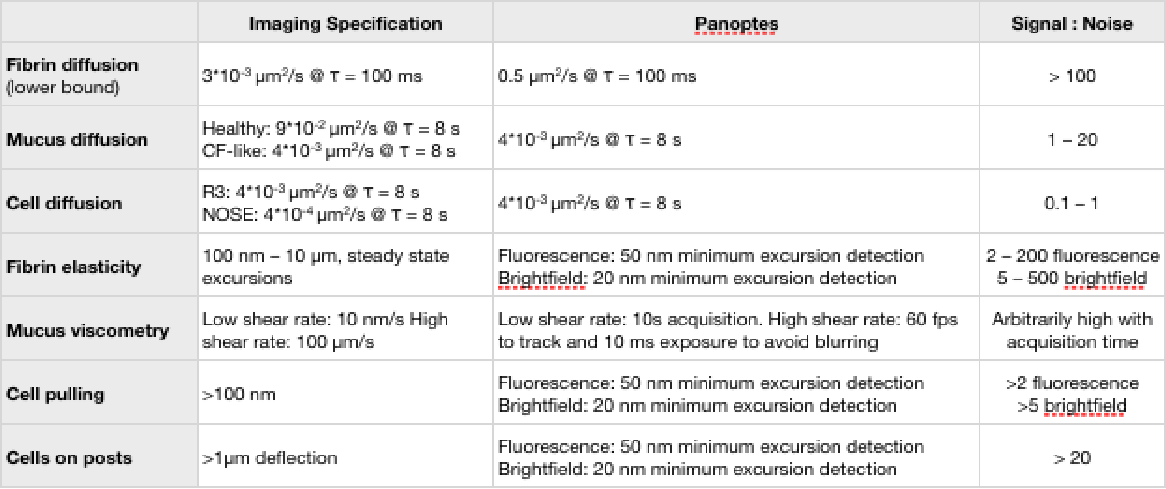

	Imaging Specification	Panoptes	Signal : Noise
Fibrin diffusion (lower bound)	$3*10^{-3}$ µm^2/s @ τ = 100 ms	0.5 µm^2/s @ τ = 100 ms	> 100
Mucus diffusion	Healthy: $9*10^{-2}$ µm^2/s @ τ = 8 s CF-like: $4*10^{-3}$ µm^2/s @ τ = 8 s	$4*10^{-3}$ µm^2/s @ τ = 8 s	1 – 20
Cell diffusion	R3: $4*10^{-3}$ µm^2/s @ τ = 8 s NOSE: $4*10^{-4}$ µm^2/s @ τ = 8 s	$4*10^{-3}$ µm^2/s @ τ = 8 s	0.1 – 1
Fibrin elasticity	100 nm – 10 µm, steady state excursions	Fluorescence: 50 nm minimum excursion detection Brightfield: 20 nm minimum excursion detection	2 – 200 fluorescence 5 – 500 brightfield
Mucus viscometry	Low shear rate: 10 nm/s High shear rate: 100 µm/s	Low shear rate: 10s acquisition. High shear rate: 60 fps to track and 10 ms exposure to avoid blurring	Arbitrarily high with acquisition time
Cell pulling	>100 nm	Fluorescence: 50 nm minimum excursion detection Brightfield: 20 nm minimum excursion detection	>2 fluorescence >5 brightfield
Cells on posts	>1µm deflection	Fluorescence: 50 nm minimum excursion detection Brightfield: 20 nm minimum excursion detection	> 20

Figure 5.5: Experiment checklist. Required specifications and Panoptes's performance are listed above. For cell pulling, the signal-to-noise ratio for brightfield is probably optimistic, because noise floor data were taken on clear glass. Because cells add background texture, they will likely degrade particle tracking, reducing the noise floor. Therefore, fluorescence is likely the preferable imaging mode for cell pulling experiments.

clot, then each type requires 2.5 minutes of data collection.

5.2 Transitioning to High Throughput Protocols

In this section, I address the data processing issues that, as with many modern experiments, throttle diffusion measurements. The first task in bringing any experiment to high throughput is to chase the bottleneck. For many modern experiments, this bottleneck is in the data processing. For diffusion measurements, the bottleneck is particle tracking. The auto-tracking algorithm used in this work effectively eliminates that bottleneck: though it might take 10-20 hours to track all the particles in a dataset, the algorithm, developed by R. Schubert and R.M. Taylor II, can run without supervision, relieving the technician of a tremendous burden.

Relieving the bottleneck, however, creates a flood of new data. Suddenly, instead of tens of particle traces, the technician can collect thousands. Where previously he could review each particle trace for tracking errors, he is now constrained to review a small percentage. Techniques to spot-check data quality become critical.

As with any automated routine, failure modes for auto-tracking are inevitable. Through spot-checking, the technician can notice common types of "bad traces," and he can create filters to remove these traces from the data before analysis.

As the technician builds confidence in the data pipeline for an experiment, he will become curious about the sensitivity of the measurement to video quality, tracking parameters, filters, and analysis parameters. The technician's goal will be to make his experiment as insensitive as possible to variations in the analysis pipeline, as this is surely one indicator of the robustness of the measurement.

In the case of fibrin diffusion, these issues are captured in the experimental workflow, which is charted in Figure 5.6. The central column of tasks—clot creation, data acquisition, tracking, filtering, and analysis—are straightforward. The difficulty in creating a robust pipeline lies largely in the feedback to earlier stages of the workflow through the sensitivity testing step.

5.2.1 Data pathologies in fibrin diffusion measurements

I now highlight specific issues regarding data quality in high throughput fibrin diffusion measurements. Figure 3.2 exhibits some clear outlier traces. Figure 5.7 demon-

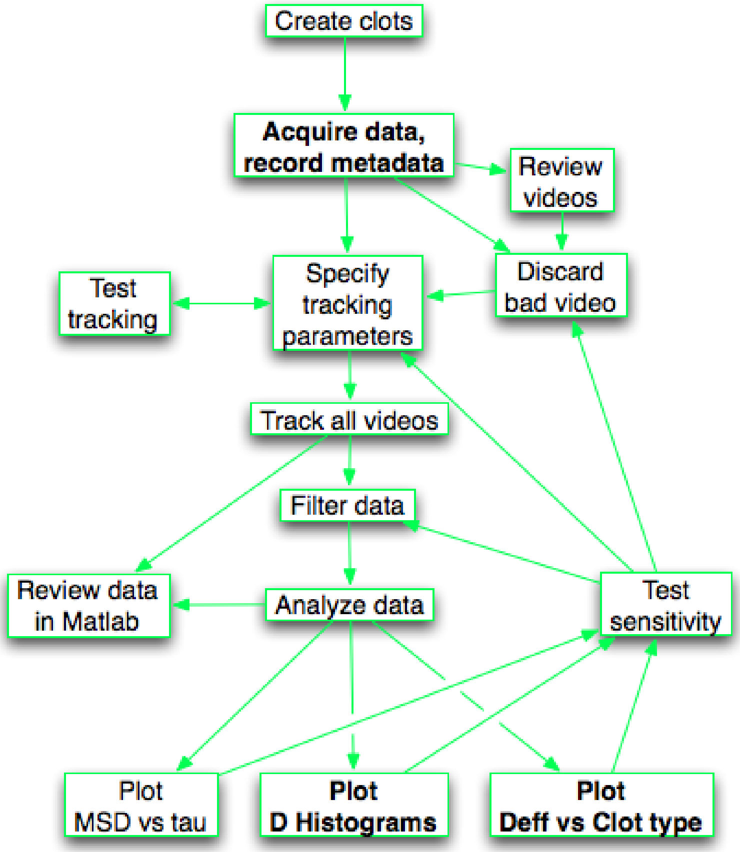

Figure 5.6: Flowchart showing a workflow for preparing D_{eff} experiments in fibrin.

strates that these are failure modes of automatic particle tracking. The most common error is the "ghost tracker," a bad decision of the auto-tracking algorithm to place a tracker on nothing. Also an issue is an image-boundary effect, where the algorithm will continue to track along one axis even though it can go no further in the other. Pop-off is where a tracker loses the particle a frame (or two, or three) before the algorithm deletes the tracker. The least common, but most troubling pathology is two-particle confusion, where a tracker on a moving particle will pass close to a static particle, and get stuck.

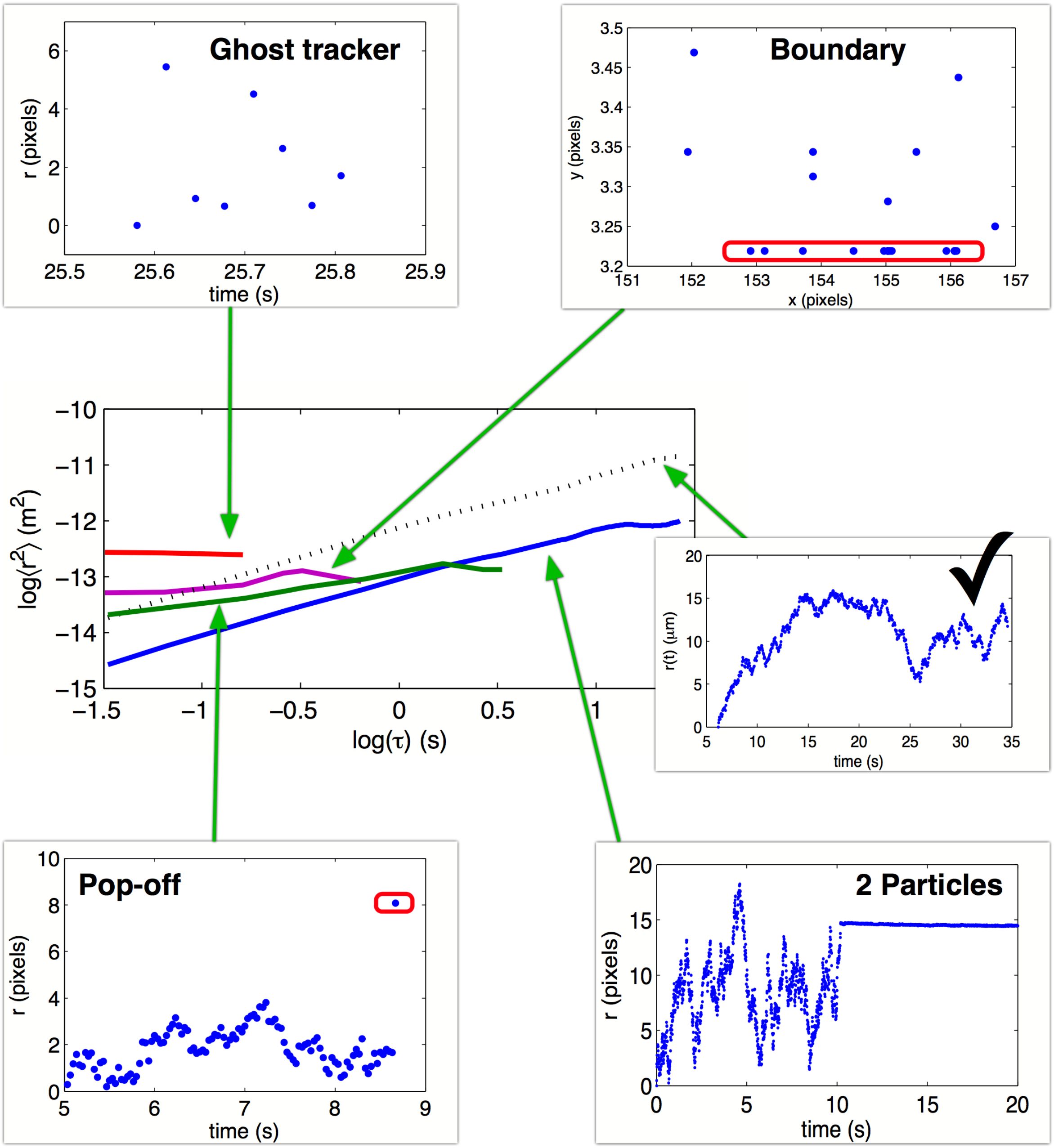

Figure 5.7: Pathological $\langle r^2 \rangle$ and the auto-tracking errors that generate them. Clockwise from the top-left: ghost trackers, image boundary effect, an accurately tracked particle, two-particle confusion, and pop-off.

There are simple measures to filter each of these outlying trace types. Ghost trackers are typically short-lived, and filtering trackers that last less than 2 seconds appears to eliminate all of them. Wall-effect tracking errors occur at the extreme edge of the image, and filtering trackers that come to the image boundary eliminates all of them. Pop-on or pop-off trackers show sharp transitions in r^2 at short timescales, so filtering for non-stationary statistics would eliminate these trackers.

I contend that this experience in developing a high throughput fibrin diffusion experiment has elements universal to bringing any experiment to a high throughput format. Equally important, every new individual who decides to perform the measurement must go through some version of this process. Skepticism of a new measurement will flourish naturally; its natural predator is the ability to test the sensitivity of the measurement against acquisition and processing parameters. The instrumentation designers' responsibility, above all else, is to build a user interface hostile to the prey.

5.2.2 DataBrowser

I have designed a software interface to facilitate the process of experiment development for high throughput microrheometry. I have based the interface around the workflow of Figure 5.6. A mock-up is shown in Figure 5.8. The leftmost column of interface elements provides a convenient environment to browse an experiment's videos and associated metadata. The types of metadata used in our experiments are catalogued in Appendix D.

The interface's layout conforms to the central workflow of tracking, filtering, and

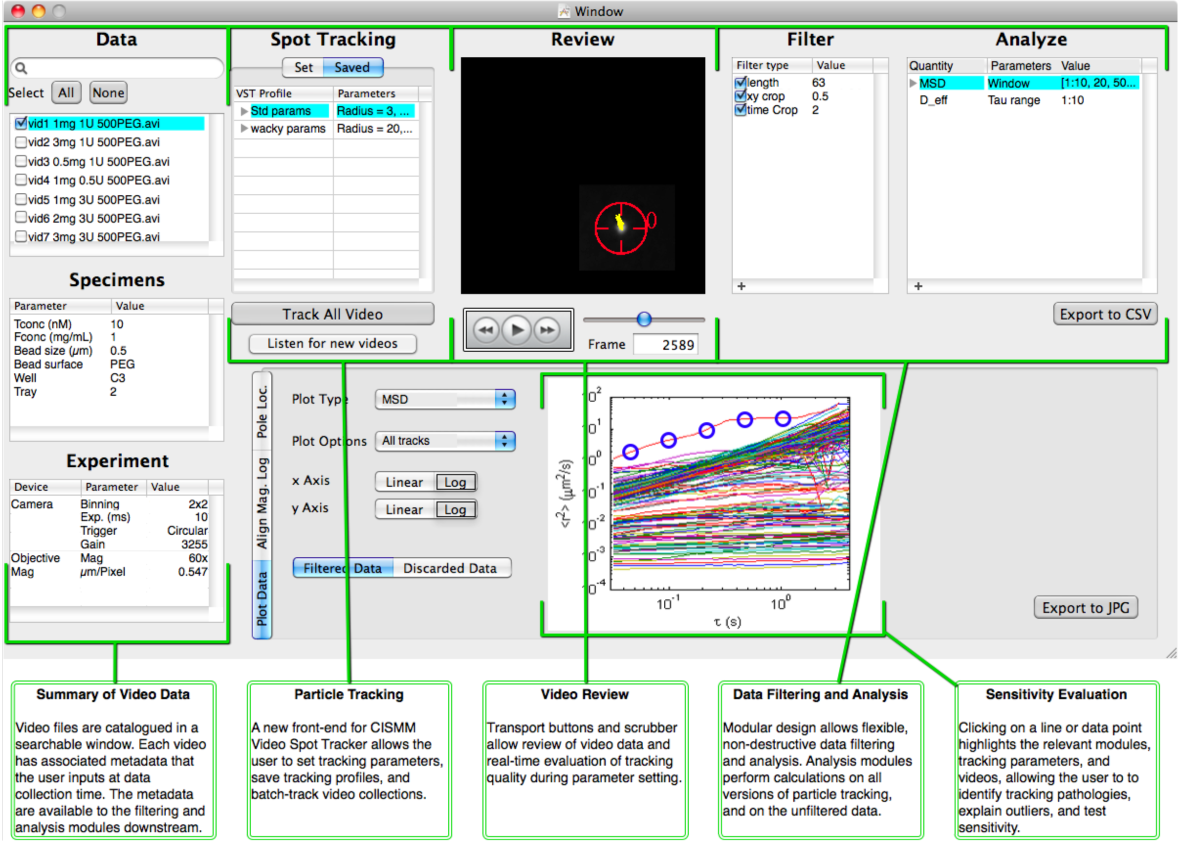

☑ vid1 1mg 1U 500PEG.avi
☐ vid2 3mg 1U 500PEG.avi
☐ vid3 0.5mg 1U 500PEG.avi
☐ vid4 1mg 0.5U 500PEG.avi
☐ vid5 1mg 3U 500PEG.avi
☐ vid6 2mg 3U 500PEG.avi
☐ vid7 3mg 3U 500PEG.avi

VST Profile	Parameters
Std params	Radius = 3, ...
wacky params	Radius = 20,...

Parameter	Value
Tconc (nM)	10
Fconc (mg/mL)	1
Bead size (μm)	0.5
Bead surface	PEG
Well	C3
Tray	2

Device	Parameter	Value
Camera	Binning	2x2
	Exp. (ms)	10
	Trigger	Circular
	Gain	3255
Objective	Mag	60x
Mag	μm/Pixel	0.547

Frame 2589

Filter type	Value
☑ length	63
☑ xy crop	0.5
☑ time Crop	2

Quantity	Parameters	Value
MSD	Window	[1:10, 20, 50...
D_eff	Tau range	1:10

Plot Type: MSD

Plot Options: All tracks

Summary of Video Data

Video files are catalogued in a searchable window. Each video has associated metadata that the user inputs at data collection time. The metadata are available to the filtering and analysis modules downstream.

Particle Tracking

A new front-end for CISMM Video Spot Tracker allows the user to set tracking parameters, save tracking profiles, and batch-track video collections.

Video Review

Transport buttons and scrubber allow review of video data and real-time evaluation of tracking quality during parameter setting.

Data Filtering and Analysis

Modular design allows flexible, non-destructive data filtering and analysis. Analysis modules perform calculations on all versions of particle tracking, and on the unfiltered data.

Sensitivity Evaluation

Clicking on a line or data point highlights the relevant modules, tracking parameters, and videos, allowing the user to to identify tracking pathologies, explain outliers, and test sensitivity.

Figure 5.8: Mockup of a data processing application, DataBrowser. The layout assumes a central workflow of tracking, filtering, and analysis. In addition, the $\langle r^2 \rangle$ plot in window's inset is active, allowing, for example, quick evaluation of whether a tracking failure is responsible for an outlying $\langle r^2 \rangle$ curve.

analysis. The filter and analysis functionality is modular. The catalogue of filter modules might include filtering by trace length or minimum particle motion. Analysis modules might include $\langle r^2 \rangle$ or D_{eff}. A modular design for filtering and analysis would make DataBrowser more flexible, and potentially position the application to address the needs of a wide variety of high throughput microscopy experiments beyond the scope of this dissertation.

The interface also enables the feedback loop of testing sensitivity to refine tracking and filtering parameters through interactive plotting. Clicking on one $\langle r^2 \rangle$ curve would allow the user to quickly review the raw video from which the tracking data were collected. If the tracking were deemed faulty, the user could add a new filter intended to eliminate that type of tracking error and immediately see whether it eliminates the offending data.

Similarly, a module that calculated D_{eff} would produce a plot similar to those in Figures 3.6, and would support clicking on an individual datapoint. This action would highlight the applied filters and the videos that compose the final datapoint. Unchecking a video would trigger re-plotting without including that video's data; the user could then observe the sensitivity of the datapoint to that video—for example, the unchecking of a bad video might cause the error bars of the datapoint to shrink.

The DataBrowser interface is intended to be extensible to other types of experiments we perform in our research group, and potentially to a wide range of high throughput microscopy experiments. Discussions with other scientists have revealed potential areas for improvement or expansion of the DataBrowser interface. These include a step in the pipeline for image analysis or processing (presumably before particle tracking), the ability to import simulated tracking data, and the ability to append imaging data (for example, quantities extracted from confocal images of clots) to the metadata of a video.

5.3 MHTS: High Throughput Manipulation

High throughput microbead rheology consists of more than diffusion measurements. In particular, forcibly manipulating microparticles can provide a wealth of additional information, including information about individual cell mechanics (Bausch et al., 1998) and nonlinear polymer rheology (Meehan et al., 2010).

There has been little intersection between the high throughput trend and mechanical study of biological systems. One high throughput nano-manipulation device, IBM's "Millipede" multi-tip AFM (Dürig et al., 2000), is a notable exception, but its primary application has been in data storage.

Among the systems for nano-manipulation, techniques using microbeads (particles $\sim 0.1 - 10\mu m$) have been widely applied. Microbeads are used to measure mechanical properties of cells (Hubmayr et al., 1996; Bausch et al., 1999; Fabry et al., 2001; Lele et al., 2007; Lenormand et al., 2007). Drug delivery strategies are being developed using magnetic micro- and nano-particles (Dobson, 2006). Transfection efficiency has been improved using "magnetofection," where vectors are attached to magnetic particles that are pushed against cells by magnetic fields (Plank et al., 2003).

Among microbead techniques, the "active," or "driven" techniques, where an external force is applied to a bead, can measure a wider range of moduli and are generally more flexible than the passive techniques, where the bead motion is due to thermal diffusion. Driven microrheology instrumentation includes laser traps ("optical tweezers") and paramagnetic attraction ("magnetic tweezers"). A laser trap offers high spatial resolution and can be precisely calibrated (Neuman and Block, 2004). A magnetic system can drive multiple beads simultaneously, produce higher forces at a given bead size, and will neither heat nor otherwise interact with most biological specimens (Fisher et al., 2006). The benefits of a driven system are apparent in this dissertation, as well, as the results of Chapter 4 demonstrate.

In pursuit of HTS nano-manipulation, I have collaborated with a diverse team of engineers and scientists to design, implement, and qualify a magnetics system for microparticle manipulation that is compatible with high throughput screening standards (Spero et al., 2008). Briefly, the Magnetic High Throughput System (MHTS) can apply forces $\sim 1pN$–$10nN$. It is based on standard microplate geometry, and is designed to be scalable to 96 wells. The force calibration is uniform from well to well within a factor of two. The magnetic crosstalk among wells is $< 5\%$. The temperature is controllable by a fluid recirculation system, and maintains $< 4°$C temperature rise under the most pessimistic conditions. The MHTS has measured non-linear mucus viscosity. Finally, cells have been successfully plated and their compliance has been measured using the system.

5.3.1 MHTS Design

The present instrument, a Magnetic High Throughput System (MHTS) consists of two components: 1) a *magnetics block*, which generates magnetic flux for each well, and 2) a *magnetic microplate*, a custom-designed high throughput tray that incorporates a pole-flat in each specimen well. The arrangement of these components is summarized in Figure 5.9. The magnetics block contains a system of drive cores and drive coils; we report here on a 16-well prototype with a design that is scalable to 96 wells.

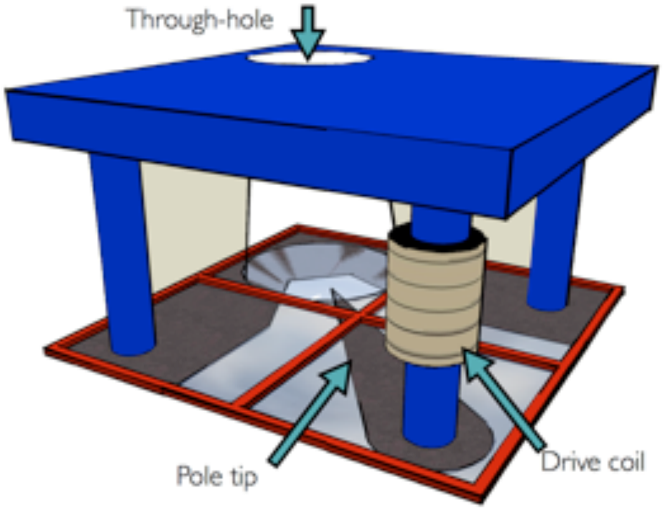

Figure 5.9: A cartoon of a single well's magnetic system. The substrate is a pole-flat affixed to glass. The quadrants on the substrate show the footprint of a 2 x 2 section of the 384-well tray. The three-legged structure is the corresponding section of the magnetics block. A magnetic circuit begins in the drive coil (front well), where current creates magnetic flux directed by the drive core into the pole. Flux jumps the specimen gap (back well) to the flat, which is connected by two return path ears (left and right wells) to the back of the coil. By changing the etching pattern in the specimen gap (back well), the force field can be changed. A through-hole above the specimen gap provides access for dosing of the specimen during an experiment, and illumination for brightfield transmission microscopy.

5.3.1.1 The Magnetics Block

Generating magnetic forces requires a complete magnetics system: drive coil, drive core, and magnetic return path. Figure 5.10 demonstrates how a complete magnetics system can fit within the area of one Society for Biomolecular Screening (SBS) microplate well[5]. Each of the 16 magnetics systems includes a drive core and two *ears*

---

[5] The geometry of the magnetics block is the result of close collaboration with L. Vicci; I am indebted to her for implementing this geometry in a manufacturable block.

that provide the magnetic return path. The magnetics block also has 16 through-holes for brightfield illumination of the wells. To direct magnetic flux to the poles, the drive cores and ears extend past the bottom of the coils, so that when the magnetics block drops into the microplate, the drive cores and ears contact the pole-flats at the bottom of the wells.

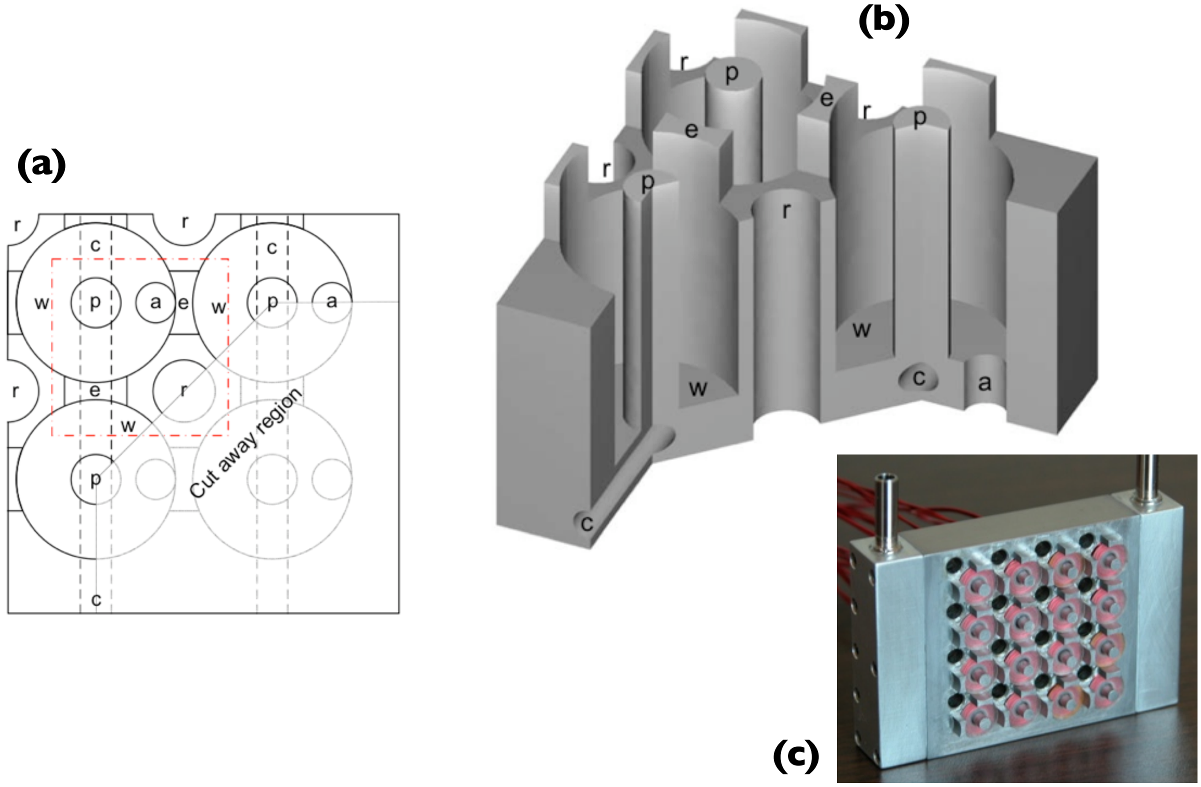

Figure 5.10: Schematics and a picture of the magnetics block; compare with the cartoon presented in Figure 5.9. A magnetic system for a single well is outlined by dashed square in schematic view (a). A cut-away perspective view is shown in (b). Within the area of one well in a 96-specimen microplate, the magnetics block houses two return path ears `e`, an optical relief `r`, a drive coil well `w`, and drive pole core `p`. Arranging the drive core on a diagonal from the specimen well and optical relief maximizes the volume for the drive coil. Heat transfer fluid channels `c` are drilled transversely to the optical paths, avoiding the coil wire access holes `a`. The 16-well prototype magnetics block, is shown in (c), populated with drive coils, and with aluminum manifolds mounted. The manifolds interface with a heat exchanger and recirculation pump.

5.3.1.2 Fabrication of a biocompatible magnetic microplate

While we can place the magnetics above the specimen, the poles must be built into the HTS microplate. This constraint has three motivations. First, the force on beads increases with the pole tip's proximity to the specimen. Second, when using a pole-flat, forces are applied in the plane of the pole tip, which to record bead motion must to be parallel to the imaging plane. (For experiments requiring forces parallel to the imaging axis, alternate pole geometries may be implemented.) Third, a magnetic microplate can be washed and reused. It is relatively inexpensive, and so can be produced in quantity to allow for simultaneous preparation of many different experiments.

I assembled the magnetic microplate by adhering a *pole plate* underneath a bottomless plastic 384-well superstructure (Thermo Fisher Scientific, Portsmouth NH). The pole plate is an of array 16 pole-flats fixed to a 4.33″x2.93″ #1-thickness coverglass. I summarize the process in Figure 5.11.

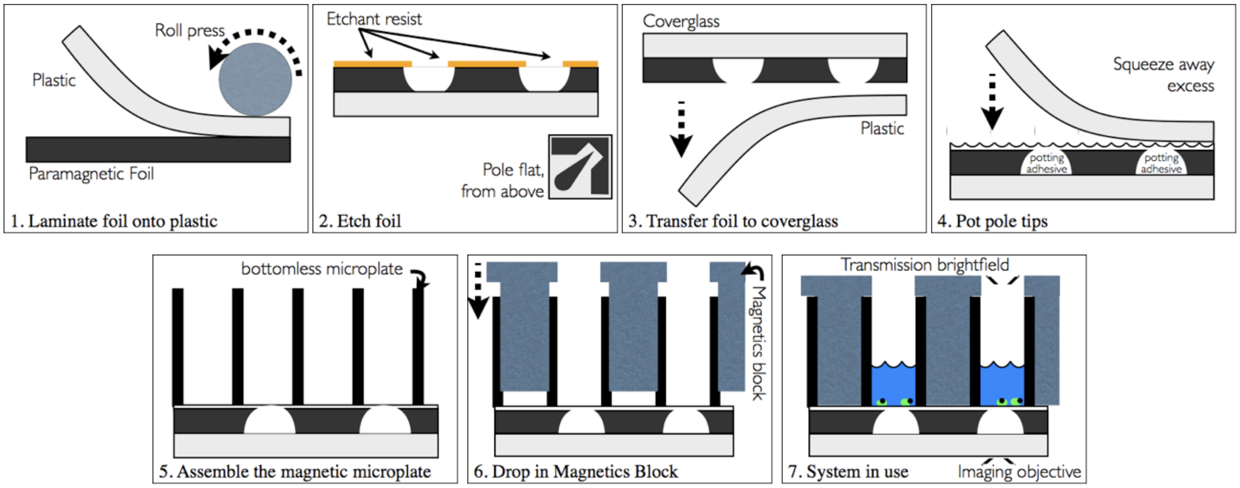

Figure 5.11: Magnetic microplate fabrication.

We use a commercial photolithographic etching process (Fotofab Corporation, Chicago IL) to manufacture the pole plate pattern. The poles must be isolated from any surrounding magnetic material. Therefore, to maintain registration of these "floating" poles relative to the flats, we bond the 0.004″-thick foil (Magnetic Shield Corporation, Bensenville IL) to a sacrificial sheet of 0.005″-thick polycarbonate backing (K-mac Plastics, Wyoming MI). Here I report on an array of pole flats (see the inset of Figure 5.11, step 2), but any shape of pole tip may be specified at this stage. The pole plate pattern is etched from the metal side of the foil-on-plastic.

To transfer the patterned foil to an optically clear substrate while maintaining the registration of the poles, we roll UV-curable adhesive NOA 81 (Norland Optical Adhesives, Cranburg NJ) onto the etched foil, cover it with #1-thickness coverglass, press flat with a glass plate and cure, then remove the plastic backing. This orientation places the sharp tip edge $\sim 100\mu m$ above the surface of the coverslip. A layer of parylene, vapor-deposited at this stage, inhibits pole degradation.

The highest force is in the plane of the pole edge, where the force ranges as high as $\sim 1nN$ (see Figure 5.12) on a $4.5\mu m$ bead. This geometry is desirable for some applications, including rheometry of biomaterials. For other applications, including cell force experiments, it is desirable to have the bottom of the well level with the pole. To raise the cells to this height, we pot the foil in NOA 81, creating an optically clear surface within $10\mu m$ of the plane of the poles. To create a surface conducive to cell adhesion, we vapor-deposit 3-Aminopropyltriethoxysilane (Sigma-Aldrich, St. Louis MO) solution onto the layer of NOA 81.

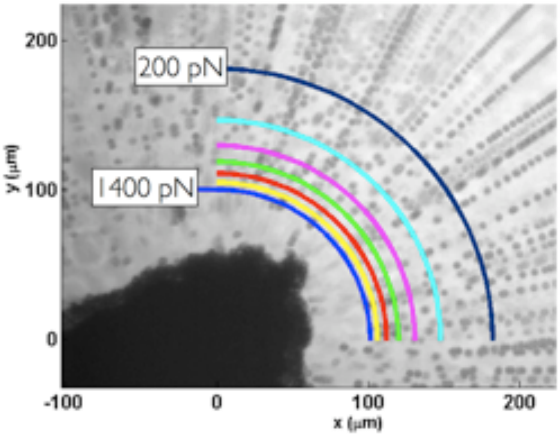

Figure 5.12: A contour plot of force on a $4.5\mu m$ bead, overlayed on a time-lapse image of a force calibration video. The contour step is $200pN$. The pole tip (bottom left) is attracting beads from the surrounding solution, which are apparent as streaks in the timelapse image. Each contour line is the average force measured on all beads at that distance from the pole tip, within 30° of the pole's axis of symmetry.

In the final step, five-minute epoxy bonds the potted pole plate to the 384-well superstructure such that the wells will not leak. The result is a 384-well microplate where three-quarters of the wells are used for the drive cores and ears, leaving 96 wells for specimens.

5.3.2 MHTS Calibration

I have used Variable Force Calibration (VFC) (Cribb, 2010) to characterize the forces in the MHTS[6]. Of greatest interest are the maximum force and crosstalk force. Figure 5.14 demonstrates that the maximum forces are $\sim 1nN$, and with 15 wells on and one well off, the crosstalk is $3 \pm 1\%$.

---

[6] I am indebted to David Bober for his work collecting this force calibration data.

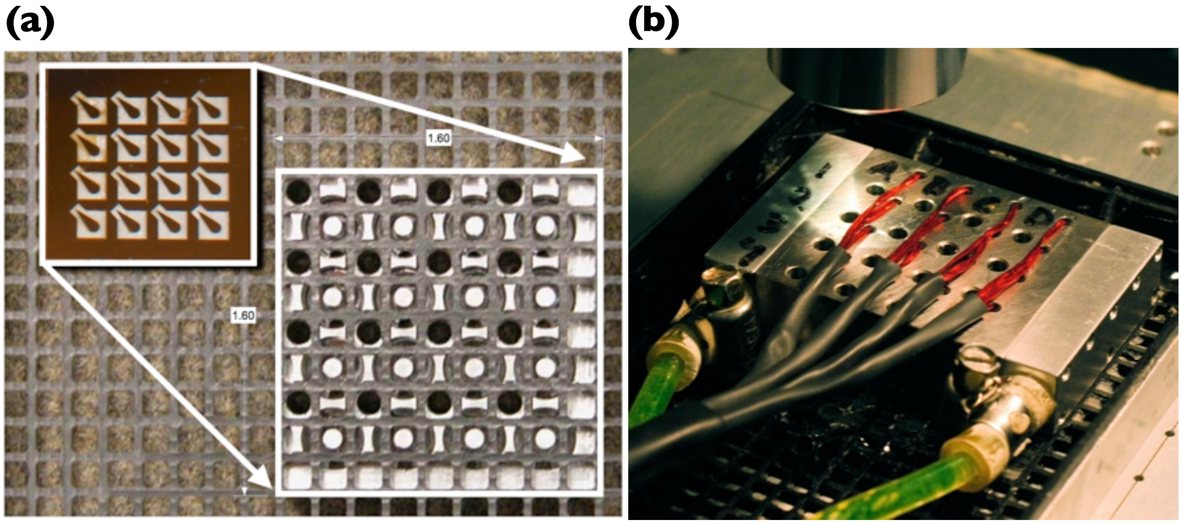

Figure 5.13: The fully assembled MHTS prototype. (a) Seen from below, the magnetics block drops into the 384 well microplate from above, and the pole plate creates the bottom of the specimen wells. (b) In operation, tubing provides fluid flow for temperature control, and a condenser objective provides transmission brightfield illumination from above. The imaging objective is below, obscured by the microplate.

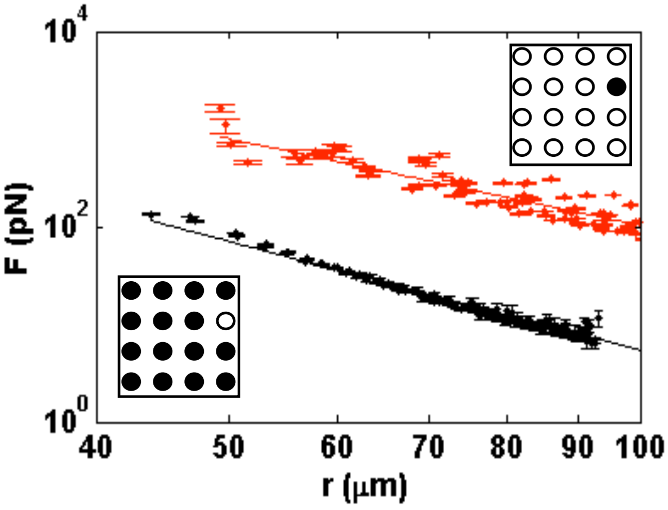

Figure 5.14: A representative calibration set for maximum force (top curve) and a calibration set showing crosstalk force (bottom curve) for a single well in the MHTS. The insets show the drive current configuration for each curve. For the maximum force calibration, the magnet in the active well is on and the other fifteen are off; for the crosstalk measurement, the active well's magnet is off and the other fifteen are on.

Ideally, the pole tips would be uniform from well to well, ensuring identical force fields in all wells. However, the etching process that produces the pole plate pattern has not proven reliable in producing uniformly sized poles, and therefore the calibration varies from well to well by ±40%, as shown in Figure 5.15. If this uncertainty is tolerable for the application, then a single calibration may be applied to data collected in all wells. This situation may be tolerable particularly in circumstances where relative measurements are of interest—for example, of sample closer to the pole tip *versus* sample farther away, or the sample before and after the well is dosed with something that might alter its mechanical properties. In specific mechanical experiments, the material property may be independent of the applied stress—for example, the relaxation time of a linear viscoelastic material. If greater accuracy is desired, each well can be calibrated individually, resulting in a variation of ±10%.

Calibration of a single well typically takes three minutes for data acquisition, 15 minutes for particle tracking, and 20 minutes for data analysis.

5.3.3 MHTS Application: Cell Mechanics

There is potential for a high throughput force system to have a dramatic impact on studies in cell mechanics and motility. A recent trend in biological studies has been the development of libraries of small molecules, proteins and RNAi for gene expression manipulation. It was a motivation for our development of the MHTS technology to explore gene expression-inhibited and ligand-mediated cell mechanical responses of Drosophila (fruit fly) cell systems using a previously developed RNAi library (Rogers

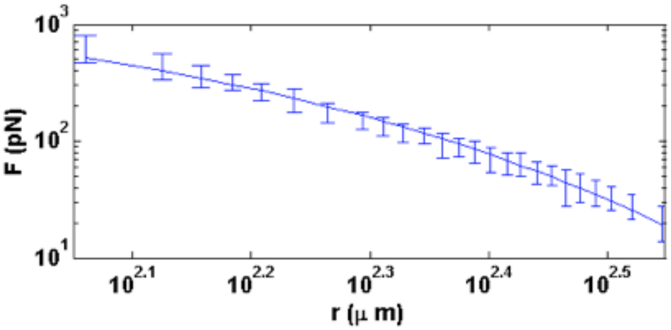

Figure 5.15: F(r) averaged over 15 wells in an MHTS magnetic microplate. One calibration set was collected at maximum drive current in each well (d = 1). The forces in each well are uniform to within ±40%, which is adequate for some applications, including order-of-magnitude rheometry experiments.

and Rogers, 2008). Understanding these pathways will help reveal the genetic origins of diseases such as cancer, hypertension and inflammatory disorders.

We have used the MHTS to study the mechanical response of cells under varying biochemistry. Drosophila derived cells (SR2+) were grown in SF 900 medium on potted, APTES treated, and Conconavalin A-washed magnetic microplates[7]. That cell cultures grow in a magnetic microplate demonstrates MHTS biocompatibility; a representative well is shown in Figure 5.16. Half of the wells with cells in them were treated with a Protein Tyrosine Phosphatase (PTPase) inhibitor cocktail (Calbiochem, San Diego CA), final concentration $0.5\mu M$. Tyrosine Phosphatases have been known to play an important role in force sensing in cells (Giannone and Sheetz, 2006), but there have

---

[7] I am indebted to David Bober, Vinay Swaminathan, and E. Timothy O'Brien, who all contributed to this experiment. The text in this section is based on writing by V. Swaminathan.

been no quantitative studies on the changes in the mechanical properties of the cell due to the inhibition of PTPases.

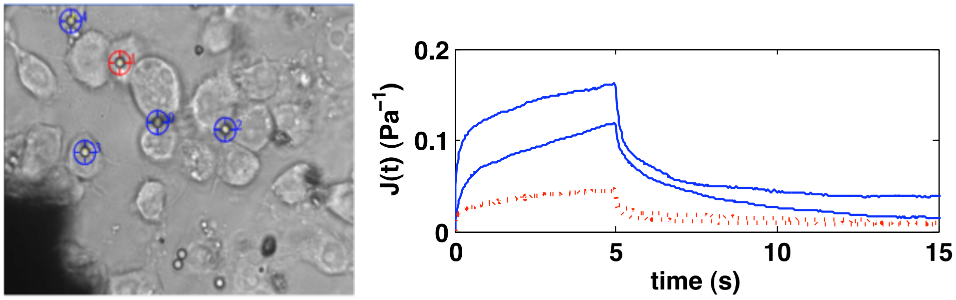

Figure 5.16: Left: The magnetic microplate is compatible with cell cultures. The shadow of the pole tip is visible, bottom left. Shown is a brightfield transmission image of the Drosophila cells in the multiwell plate, 60x, 1.2 NA water immersion objective. Magnetic beads ($d = 2.8\mu m$) are observed on the cells and their trajectory is tracked using the CISMM Video Spot tracker software. Right: Compliance $J(t) = \frac{3\pi d r(t)}{F(r,I)}$ of individual Drosophila cells under control (dotted curves) and PTPase inhibited conditions (solid curves). Each curve represents a single bead on a single cell averaged over two pulls. All four beads were on cells in separate wells. The forces acting on the beads ranges from $250 - 350pN$.

Figure 5.16 also compares the compliance of treated and untreated cells, as measured from bead displacements. The spring constant for a cell was found in a manner similar to that used in Chapter 4. The spring constant for untreated drosophila cells was $756 \pm 67 \times 10^{-6} N/m$. SR2+ cells which were treated with the PTPase inhibitor showed greater compliance. The spring constant for cells treated with the PTPase inhibitor was found to be $240 \pm 53 \times 10^{-6} N/m$.

Using the MHTS technology, a single experiment enabled mechanical measurements on cells in four independent cell cultures. The PTPase-treated SR2+ Drosophila cells exhibited thrice the compliance of control conditions; this difference is outside the uncertainty in the calibration of each well. Studies using the MHTS to study cell mechanoresponse under varying biochemical conditions are ongoing.

5.3.4 MHTS Application: Mucus Viscometry

The MHTS is the first technology for rheometry that we know to be high-throughput compatible. As an example of its use as a microrheometer, I have used the MHTS to measure rheology of mucus[8] (Cribb, 2010).

Broadly defined, mucus refers to a family of soft, viscoelastic materials secreted at the cellular and tissue scales by a wide variety of organisms, vertebrates and invertebrates alike. Its persistence through the evolutionary record speaks to its success in coating, protecting, and/or lubricating cells and cell surfaces often found at interfaces with epithelial cells (Desseyn et al., 2000). In the airways, mucus serves as the first line of defense against the inhalation of pollutants or pathogens during breathing. In pathologies such as cystic fibrosis, changes in mucus rheology can have a catastrophic effect on muco-cilliary clearance.

Figure 5.17 demonstrates that the MHTS can be used to measure mucus viscosity. In particular, the data demonstrate that driven microrheology can see shear-thinning of a polymer system, and can capture bulk viscosity of the material in a manner that single particle diffusion cannot.

---

[8] I operated the MHTS to collect the data of this Section. I am indebted to J. Cribb for his work analyzing and publishing these data, and the text in this Section is based on his work.

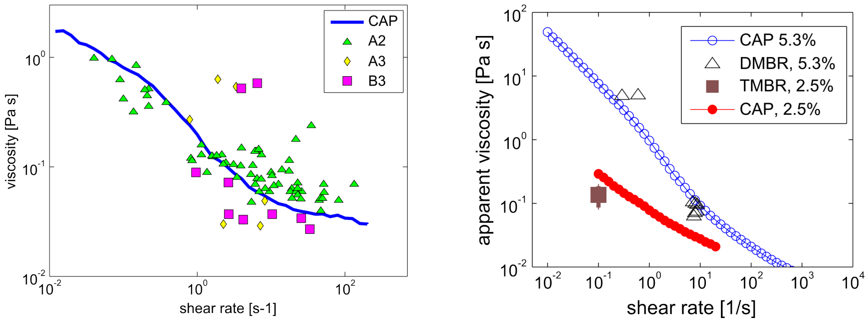

Figure 5.17: Left: Shear thinning response curve for 4% PGM measured with cone-and-plate (CAP) (solid line). The steady state viscosity values as measured by MHTS (scatter) originate from three different specimens tested by three different calibrated pole tips. All wells report viscosities similar to one another, implying the spread in the data is due to sample heterogeneity. Right: Shear thinning response curve for two specimens of HBE mucus measured with CAP (solid lines). Diffusive measurements (squares) for 2.5% mucus are lower than the CAP data by about 50%. However, MHTS measurements (triangles) for 5.3% mucus agree with CAP and exhibit shear thinning, with error in each measurement being <15%.

5.4 Governing Equations for MHTS Operation

To expand on this previously published work, I examine below three operation modes for the MHTS: calibration, a shear thinning measurement, and a strain hardening measurement. I derive the governing equations for what drive parameters and bead sizes should be used to resolve desired material properties. The section on calibration planning also highlights the data storage challenge created by the MHTS.

5.4.1 Calibration planning

In the interest of developing a smoothly operating MHTS, I propose a method to programmatically plan a calibration.

Forces are calculated from the velocity of beads pulled through a fluid of known viscosity. For Newtonian fluids with a low Reynolds number ($Re < 10^{-4}$), the force on a spherical object is equal to the Stokes drag multiplied by the particle's velocity,

$$F = 3\pi d\eta v, \tag{5.1}$$

where d is the sphere diameter, η is the dynamic viscosity of the fluid, and v is the sphere's velocity. Given fluid viscosity and the bead radius, the bead's velocity uniquely determines the force at a given position and drive current. Calibration is typically performed using $2.5M$ sucrose ($\eta = 0.12Pa\ s$). Corn syrup (ACH Food Companies, Memphis TN), a higher viscosity fluid ($\eta = 3.4Pa\ s$, verified using CAP), can be used to calibrate higher force regimes.

The inputs from the user are the vector of drive currents $\boldsymbol{I}$ and the fields of view to be calibrated[9]. The new work presented below can be summarized as determining the vector of dwell times $\boldsymbol{t}_{\mathrm{FOV}}$ and the number of times to repeat the pulse sequence p_{FOV} in each field of view.

Step 1: Find the coordinate system origin $r(x_0, y_0) = 0$. The force on a bead is a function of distance from the pole tip, r. Within a 30° cone of the pole tip there is little azimuthal variation in the force, and it can be assumed to be dependent only on the radial coordinate r. In this step, image analysis algorithms would determine the location of the pole tip, define the origin of this coordinate system, and translate all bead positions into this coordinate system. These algorithms are under development,

---

[9] For a thorough calibration, $\boldsymbol{I} = [0, 0.1, 0.25, 0.5, 0.75, 1, 1.5, 2, 2.5]$ is typical.

and are outside the scope of the present work.

The step will offer a major advantage over the current system. If the data are collected in a location known relative to $r = 0$, then calibration and experiment data may be collected in fields of view that do not include the pole tip. This dramatically relaxes the field of view constraint for the multiscope, permitting higher magnification without sacrificing force range, bead sparseness, and distance from boundaries (namely, the pole tip). The remainder of this discussion will assume the need to calibrate multiple fields of view.

Step 2: Determine the dwell time vector in each field of view, $\boldsymbol{t}_{\mathrm{FOV}}$. It is critical that t_i, the dwell time at each drive current, be optimized. For dwell times that are too short, the bead will not move far enough to make a measurement; for dwell times that are too long, the bead will move too far, reducing the spacial resolution of calibration.

The proper $\boldsymbol{t}$ depends on how fast the bead moves, as determined by Equation 5.1. This velocity cannot be known without knowing the force that that the pole tip applies—precisely the quantity that calibration is used to determine. Thus we must begin with a predicted calibration,

$$\mathrm{F}'_I(r) = \alpha'_I r^{\beta'_I}, \tag{5.2}$$

where α'_I, and β'_I are predicted fitting parameters at each drive current I. To calibrate each field of view, it is sufficient to use the position of the center of the field relative to the pole tip, r_{FOV}. In the following calculation I will refer to the average force predicted at a particular current, for a particular bead, in a given field of view, $< \mathrm{F}'_I(r_{\mathrm{FOV}}) >$.

The following constraints exist on any given dwell time, t_i. First, it must be more than ten frames long for a good velocity measurement (the slope of a linear fit to $r(t)$). Second, the bead must move ten times the imaging resolution $\Delta x_{\min}$. Third, the bead must move more than ten times the root-mean-squared distance expected from thermal diffusion. The third condition may be expressed as

$$\Delta r = v t_i = \frac{< \mathrm{F}'_I(r_{\mathrm{FOV}}) > t_i}{3\pi\eta d} \geq 10\sqrt{< r_{\mathrm{D}}^2 >} = 10\sqrt{4t_i\frac{k_{\mathrm{B}}T}{3\pi\eta d}}$$

where r_{D} is the position of the bead due to diffusion, and $k_{\mathrm{B}}T$ is the thermal energy. After solving for t_i above, the constraints on the dwell times may be summarized:

$$\begin{aligned} t_i &\geq 10\ t_{\mathrm{frame}} \\ t_i &\geq 10\ \frac{3\pi\eta d\Delta x_{\min}}{< \mathrm{F}'_I(r_{\mathrm{FOV}}) >} \\ t_i &\geq 10^2\ \frac{12\pi\eta d k_{\mathrm{B}}T}{< \mathrm{F}'_I(r_{\mathrm{FOV}}) >^2}. \end{aligned} \tag{5.3}$$

For spacial resolution and calibration speed, t_i should be as small as possible. Thus, t_i will equal the largest of the three constraints. (In the zero-current case, $\mathrm{F} \to 0$, and t_i can be taken as twice the the longest time for the non-zero current cases. These must be calculated for each drive current I and each field of view r_{FOV} to generate $\boldsymbol{t}_{\mathrm{FOV}}$

Step 3: Determine the number of current pulses per field of view, p_{FOV}. The pulse sequence, consisting of the drive currents $\boldsymbol{I}$ applied for dwell times $\boldsymbol{t}$, must be repeated at least enough times that a bead at one edge of the field of view be pulled. Namely,

$$\Delta r \geq l_{\text{frame}} \tag{5.4}$$

where l_{frame} is the real-space length of the frame's diagonal. Each pulse sequence has a vector of speeds approximated by

$$\boldsymbol{v}_{\text{FOV}} = \frac{< \mathbf{F}'_{\boldsymbol{I}}(r_{\text{FOV}}) >}{3\pi\eta d} = \frac{\alpha'}{3\pi\eta d\ l_{\text{frame}}\ (\beta'+1)}\ r^{\beta'+1}\Big|_{r_{FOV}-\frac{l_{\text{frame}}}{2}}^{r_{FOV}+\frac{l_{\text{frame}}}{2}}, \tag{5.5}$$

where $< \mathbf{F}'_{\boldsymbol{I}}(r_{\text{FOV}}) >$ is the vector of estimated average forces at the currents $\boldsymbol{I}$ for each field of view. The average force, substituted explicitly in the far right term above, was found using the classical calculus, $< f >= \frac{1}{b-a}\int_a^b f$. The total motion over a pulse sequence is therefore

$$\Delta r_{\text{FOV}} = p_{\text{FOV}}(\boldsymbol{v}_{\text{FOV}} \cdot \boldsymbol{t}_{\text{FOV}}), \tag{5.6}$$

where p_{FOV} is the number of pulse sequence repeats for a given field of view, and is solved for by combining Equations 5.4, 5.5 and 5.6:

$$p_{\text{FOV}} \geq l_{\text{FOV}} \frac{3\pi\eta d}{< \mathbf{F}'_{\boldsymbol{I}}(r_{\text{FOV}}) > \cdot\ \boldsymbol{t}_{\text{FOV}}} \tag{5.7}$$

The calibration plan developed in steps 2 and 3 is summarized in Figure 5.18. Note that as the forces get smaller, whether by reducing the drive current or moving farther from the pole tip, the time required to apply the force increases. The number of pulse sequences in each field of view peaks at the intermediate distances from the pole tip, where the imaging resolution Δx_{min} determines most t_i. Farther away from the pole tip, diffusion interferes with the force measurement, requiring longer-distance pulls, and therefore reducing the number of pulse sequences per field of view.

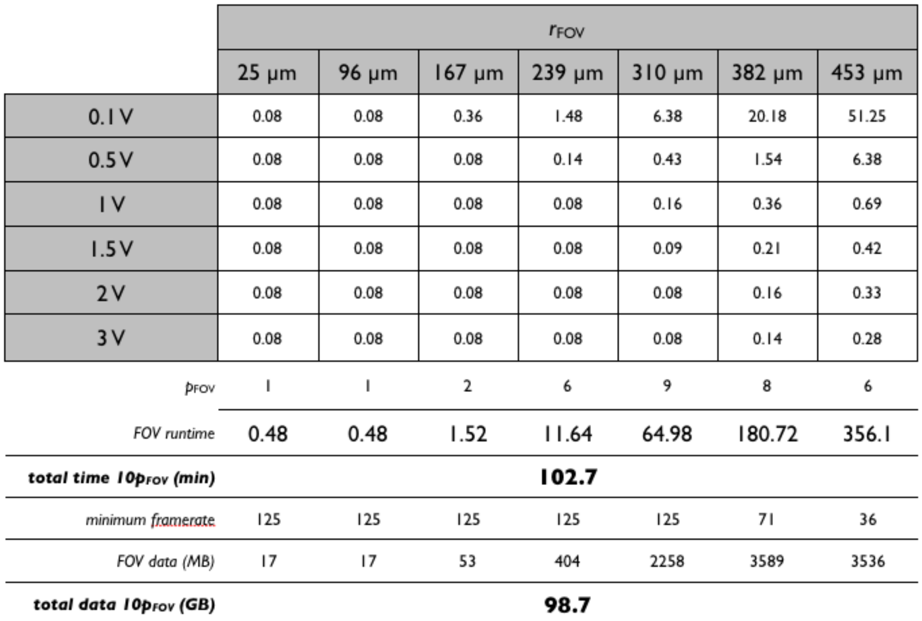

	r_{FOV}						
	25 µm	96 µm	167 µm	239 µm	310 µm	382 µm	453 µm
0.1 V	0.08	0.08	0.36	1.48	6.38	20.18	51.25
0.5 V	0.08	0.08	0.08	0.14	0.43	1.54	6.38
1 V	0.08	0.08	0.08	0.08	0.16	0.36	0.69
1.5 V	0.08	0.08	0.08	0.08	0.09	0.21	0.42
2 V	0.08	0.08	0.08	0.08	0.08	0.16	0.33
3 V	0.08	0.08	0.08	0.08	0.08	0.14	0.28
p_{FOV}	1	1	2	6	9	8	6
FOV runtime	0.48	0.48	1.52	11.64	64.98	180.72	356.1
total time 10p_{FOV} (min)				**102.7**			
minimum framerate	125	125	125	125	125	71	36
FOV data (MB)	17	17	53	404	2258	3589	3536
total data 10p_{FOV} (GB)				**98.7**			

Figure 5.18: Plan for a single well calibration. Pulse times t_i get longer as the forces get smaller (upper-right corner of table). A full well calibration takes $\sim 100GB$, about $70GB$ of which is collected when calibrating the final two fields of view.

Step 4: Calibrate. In this step, the pulse sequences run in each field of view. The first field of view should be the one closest to the pole tip, where beads are depleted most rapidly. Subsequent fields of view may be observed, moving progressively away from the pole tip, until data have been collected over the full range of r. Software must be developed to track the beads and convert their position data into the coordinate system of the pole tip. The data analysis then proceeds as in the existing variable force calibration.

Step 5: Verify $\boldsymbol{t}$ *and re-calibrate if necessary.* Because the preceding steps use a predicted calibration for the drive magnet planning, there is the possibility that the collected data will not meet the constraints 5.3. The easiest solution is to check each datum of calibration at analysis runtime. If if any of the conditions

$$\begin{aligned} n_{\text{frames}} &< 10 \\ \Delta r &\leq 10\Delta x_{\min} \\ \Delta r &\leq 10\sqrt{< r_{\mathrm{D}}^2 >} = 10\sqrt{4t_i\frac{k_{\mathrm{B}}T}{3\pi\eta d}}, \end{aligned} \tag{5.8}$$

are met, then the datum should be excluded from the calibration as it will distort the fit to the calibration data. If the amount of excluded data is great enough to cause concern, the output of the analysis—a new family of force equations $\mathrm{F}_I(r)$—may be used in Equation 5.2 to repeat the calibration planning, generating a more satisfactory vector of dwell times $\boldsymbol{t}$.

It is critical that the plate calibration is consistent from run to run. Harm to the pole tip is the most common way to change a well's calibration, whether by chipping, bending, or rusting. All three manifest in direct imaging of the pole tip; therefore, it is advisable to record an image of the pole tip shape on each experimental run, for comparison to the image of the tip during calibration.

5.4.2 Planning strain stiffening measurements

Similar attention is merited for the planning of strain stiffening measurements. Here, the governing equations are

$$\mathrm{G}(\gamma), \tag{5.9}$$

$$\mathrm{F}_{(I,d)}(r) = \alpha_{(I,d)} r^{\beta_{(I,d)}}, \tag{5.10}$$

$$\Delta x(F, \mathrm{G}) = \frac{\mathrm{F}}{3\pi \mathrm{G} d}, \tag{5.11}$$

where Δx is the recovery displacement of the bead and G is the storage modulus of the material. For a microbead, we take $\gamma = \Delta x/d$.

Substituting γ for Equation 5.11, solving for F, and using a prediction of the strain stiffening equation $\mathrm{G}'(\gamma)$[10], we find

$$\mathrm{F} = 3\pi d^2 \gamma \mathrm{G}'(\gamma). \tag{5.12}$$

As with the shear thinning case, this can be plotted to determine which beads should be used to obtain which forces. However, there is a second constraint, imposed by the optical system, analogous to Equation 5.14 from the shear thinning experiment. When probing viscous (velocity dependent) properties, the signal-to-noise ratio will improve by pulling longer; not so with elastic (displacement dependent) properties. For any given bead, the measurement is limited at $\gamma_{\text{min}} = \Delta x_{\text{min}}/d$. A planning plot for a

---

[10] The prediction of the nonlinear storage modulus $\mathrm{G}'(\gamma)$ should not be confused with $G'(\omega)$, which is the real part of the complex modulus $G^*(\omega)$, and is defined only in the material's linear regime.

strain stiffening experiment on a theoretical specimen, shown in Figure 5.19, reveals how larger beads are required to make measurements at lower strains.

I should note that the particle size issue here adds to the particle size constraints discussed in Chapter 4. Here, all particles are assumed to be big enough that they measure bulk elastic properties. In addition, Figure 5.19 shows that in order to measure a wide range of strains, additional constraints are placed on the particle size—namely, because of the nature of the strain equation $\gamma = \Delta x/d$, the particles must be bigger.

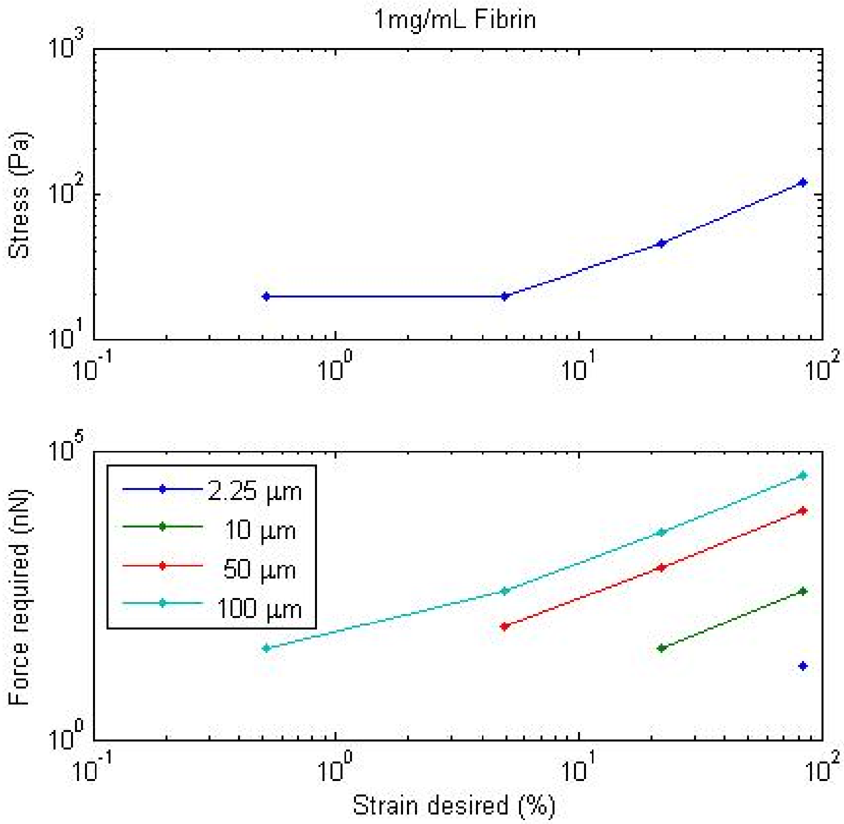

Figure 5.19: A planning plot for a strain stiffening experiment. The predicted G$'(\gamma)$ is taken from a real measurement of fibrin elasticity, the $1\ ^{mg}/_{mL}$ specimen in Figure 4.4. The plots for each bead truncate at the left due to the measurement constraint $\Delta x_{\min}$, taken here to be $1\ \mu m$.

5.4.3 Planning shear thinning measurements

The stress geometry of the MHTS is best expressed in polar coordinates. This is not the natural system for viscometry experiments, and as such, the experimental design is critical to achieving a successful measurement. Prior work (Cribb, 2010) has noted that the force required to see a given shear rate is

$$\mathrm{F} = \pi \ \dot{\gamma} \ d^2 \ \eta'(\dot{\gamma}). \tag{5.13}$$

where $\dot{\gamma}$ is the shear rate, and $\eta'(\dot{\gamma})$ is the predicted shear thinning curve.

To this I add a prescription for determining the time that force should be applied, Δt. The imaging resolution, Δx_{min}, sets one constraint, which paired with the minimum time, Δt_{min}, implies a velocity that can be entered into Stoke's Law, $v(F, \eta) = \frac{\mathrm{F}}{3\pi\eta d}$, to find

$$\Delta t_{min} \geq 3\pi d \ \Delta x_{min} \ \frac{\eta'(\dot{\gamma})}{\mathrm{F}_{(I,d)}(r)}. \tag{5.14}$$

A good rule of thumb sets $\Delta x_{min} = d$. I also note we wish to avoid any force strong enough that $\Delta t \ < \ t_{frame}$. Without this latter condition, the bead may move more than its diameter in a single frame, making it difficult to track.

5.5 High Throughput Data Collection

With the experimental systems, MHTS and Panoptes, well-envisioned, and with the analysis pipeline well defined, the pieces are in place to begin designing the user environment for high throughput data collection.

A workflow for preparing experiments is shown in Figure 5.20. As with the data analysis workflow, the steps that involve feedback are critical to creating an effective solution. In particular, I highlight the need to fine-tune the imaging parameters, and to "double-check" the metadata. The former is key to ensuring good data quality, and the latter is key to avoiding disastrous book-keeping confusion. Because we have limited experience automatically collecting large volumes of data, I will defer on proposing a complete interface for the experimental UI. The layout and functionality of this environment should remain an active area of discussion as this system's development continues.

5.6 Conclusions

It is an overarching goal of our research group to develop a high throughput system that supports preparation of multiple specimens in industry standard microplates, measure diffusion in and apply forces to particles added to those specimens, and track the motion of the particles as efficiently as possible. In this chapter I have documented the challenges facing high throughput passive and driven microrheology, and detailed system designs that address many of the issues.

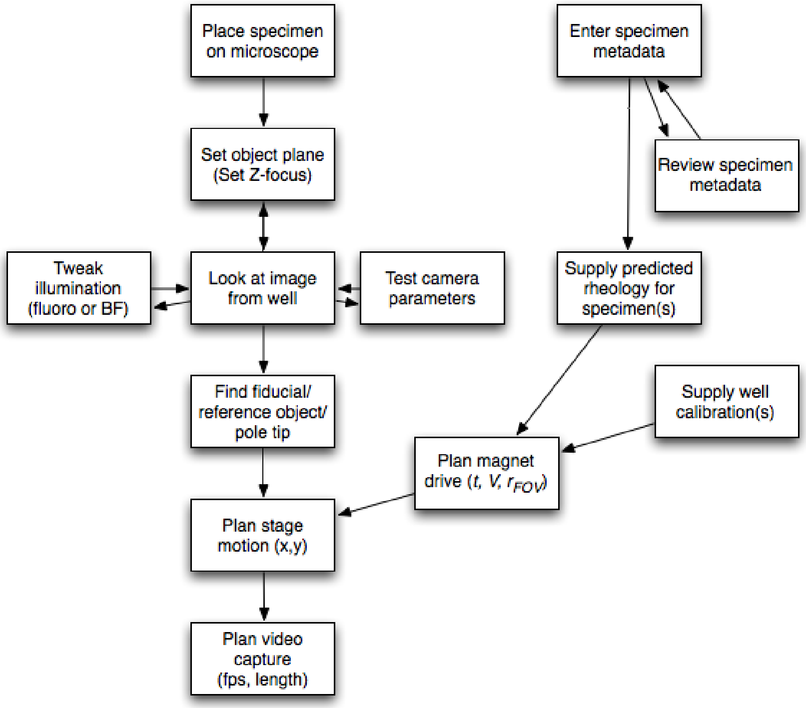

Figure 5.20: Workflow for taking high throughput MHTS data.

This development effort may be summarized as a collection of subsystems with specific functionality, summarized in Figure 5.21. It also summarizes how the functionality of the various subsystems is encapsulated in various development projects, namely the MHTS, Panoptes, the experimental UI, and DataBrowser.

While supersystem considerations are the least critical for creating a functioning instrument, they are the most critical for creating a usable one. I am indebted to the work of previous students (Cribb, 2010), especially with regard to physical layout, metadata handling, and methods for synchronizing video and magnet logs. Yet the existing system remains difficult to comprehend, laborious to operate, and easy to misuse. New users still have great difficulty learning to plan experiments and keeping

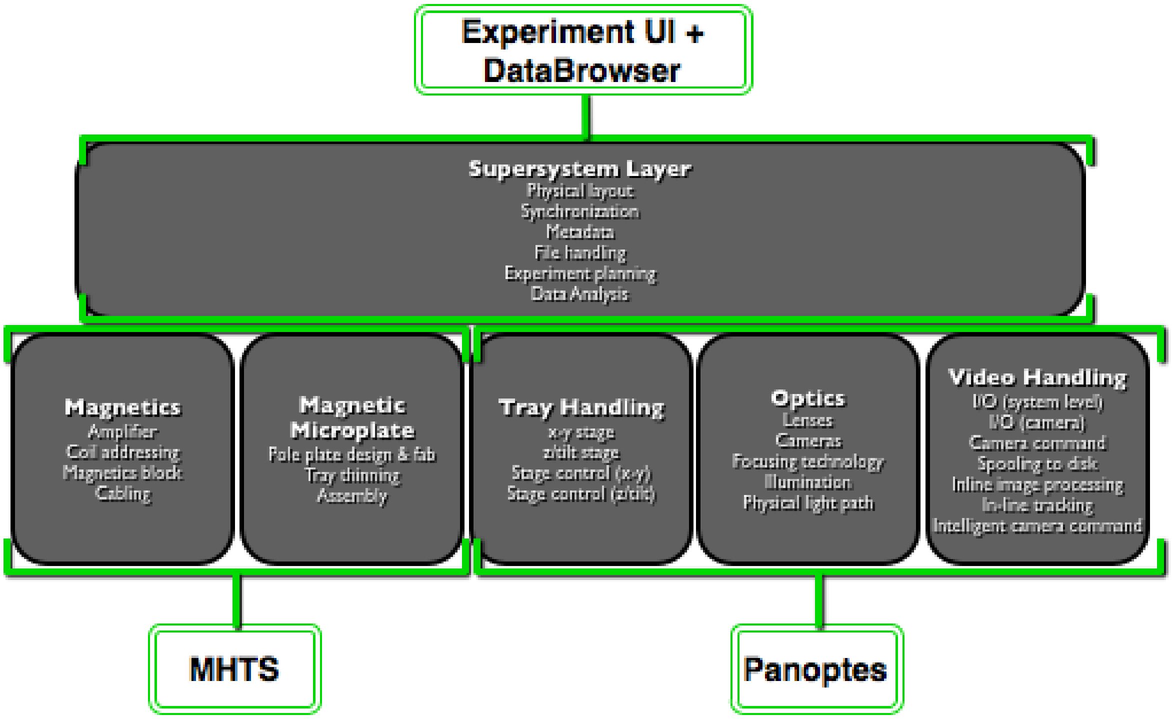

Figure 5.21: Systems overview of the MHTS. The functionality can be broken into six projects (grey boxes), while the user experiences four modular products: experimental UI, DataBrowser, MHTS, and Panoptes.

track of files generated by data collection. The former consideration was the motivation behind the experimental planning sections of this chapter; the latter was the motivation for DataBrowser. With their adoption, I believe the system will improve dramatically in usability.

Appendix A

Experimental Protocols for Diffusion, Structure, and Permeability

A.1 Clot preparation and Video Acquisition

Reagent handling, storage, thawing, and mixing. Particle concentrations were planned to obtain sufficient number density $n < 10^{-4}\mu\text{m}^{-3}$ ($\phi < 7 \times 10^{-6}$).

Clots were formed in a glass-bottom 96-well microplate (NUNC, Rochester NY), which was plasma cleaned to ensure uniform clotting and meniscus in all wells. Clots were allowed to incubate for two hours, which was the time before the level section of the slowest turbidity curve. For experiments where the particles diffused into the clot from outside, particles were added after this two hour incubation. Clots were sealed to prevent evaporation and diffusion proceeded at room temperature.

Video of nanoparticle diffusion was acquired on a inverted microscope (Nikon USA, Melville NY) with a 60x, 1.2 NA water immersion objective (Olympus, Center Valley

PA), and a high-sensitivity EMCCD camera (Photometrics, Tucson AZ). Videos were captured in at least five well-distributed fields of view, at a constant height of 50-70 μm from the glass substrate, at rates of 24-31 frames per second, for at least 60 seconds.

A.2 Automatic particle tracking and data filtering

Particles were automatically tracked using CISMM Video Spot Tracker. Some false positive particle tracks were inevitable; data were filtered to eliminate any tracks lasting less than two seconds. There is a risk of biasing diffusion results by filtering in this fashion, as it could asymmetrically trim the natural diffusion distribution. However, a track of a real particle can be expected to last for the first passage time across the imaging system's depth of field of about 5 μm. For the smallest particles used the average expected residence time in buffer is 3.4 seconds. After this filtering, the greatest damage to data fidelity were due to trackers that lost a particle but continued to log data. These "pop-offs" were pruned by hand in several datasets, and resulted in corrections to D_{eff} of under 5%.

A.3 Calculation of diffusion coefficient

Calculated $\langle r^2 \rangle$ from tracking data $(x(t), y(t))$. Calculated α by linear fit to $\langle r^2 \rangle$ over the range $0.1 < \tau < 1$. Filtered by $0.8 < \alpha < 1.2$. Computed $D_{\text{eff}} = \langle r^2 \rangle / 4\tau$ for each tracker. Computed mean and standard error for D_{eff} for each clot type.

A.4 PEG Particle Preparation

Carboxylate nanoparticles were functionalized as in (Lai et al., 2007). In an effort to evaluate the sensitivity of our diffusion measurement, we compared the size of the PEG- and COOH-functionalized particles. The presence of PEG at the surface of a nanoparticle should increase its hydrodynamic size. Particle diameters were determined by dynamic light scattering (DLS) (Malvern Instruments, Worcestershire UK) and from particle diffusion in water. These data imply a corona around the particles that is 5 nm (250 nm initial size) and 12 nm (490 nm initial size).

A.5 Structure and Permeability

Clotting time measured with turbidity. Gel structure was measured using confocal microscopy of fluorescent fibrinogen. Alexa-fluor fibrinogen (AFF) was prepared by Robert Campbell. Fibrin gels were prepared with plasma-purified fibrinogen doped with 3% AFF. Stacks were acquired on an inverted microscope (Nikon USA, Melville NY) with a 60x, 1.2 NA water immersion objective (Olympus, Center Valley PA), a spinning disk, confocal fluorescence system (Yokogawa, Atlanta GA), and a CCD camera (Photometrics, Tucson AZ). For each clot type, at least two stacks were taken in different locations of the clot.

Clot permeability was measured for purified fibrin gels. Results agreed with established values of $\kappa = 10^{-13} - 10^{-12}$ m^2 (Diamond, 1999), with finer clots exhibiting lower Darcy constants.

Appendix B

Panoptes Bill of Materials

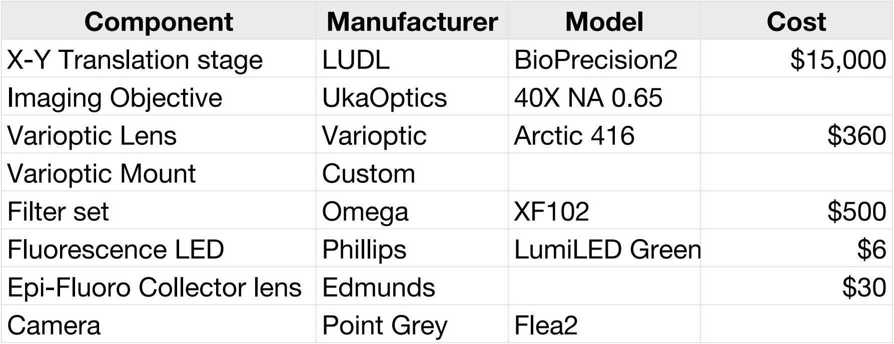

Component	Manufacturer	Model	Cost
X-Y Translation stage	LUDL	BioPrecision2	$15,000
Imaging Objective	UkaOptics	40X NA 0.65	
Varioptic Lens	Varioptic	Arctic 416	$360
Varioptic Mount	Custom		
Filter set	Omega	XF102	$500
Fluorescence LED	Phillips	LumiLED Green	$6
Epi-Fluoro Collector lens	Edmunds		$30
Camera	Point Grey	Flea2	

Figure B.1: Bill of materials for chosen parts. Designs for some components have not been finalized, so their costs are not yet known.

Appendix C

Panoptes Parts Schematics

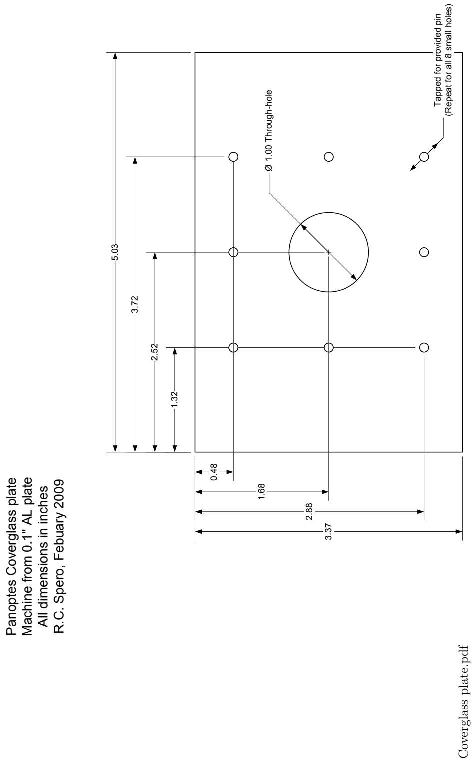

Figure C.1:

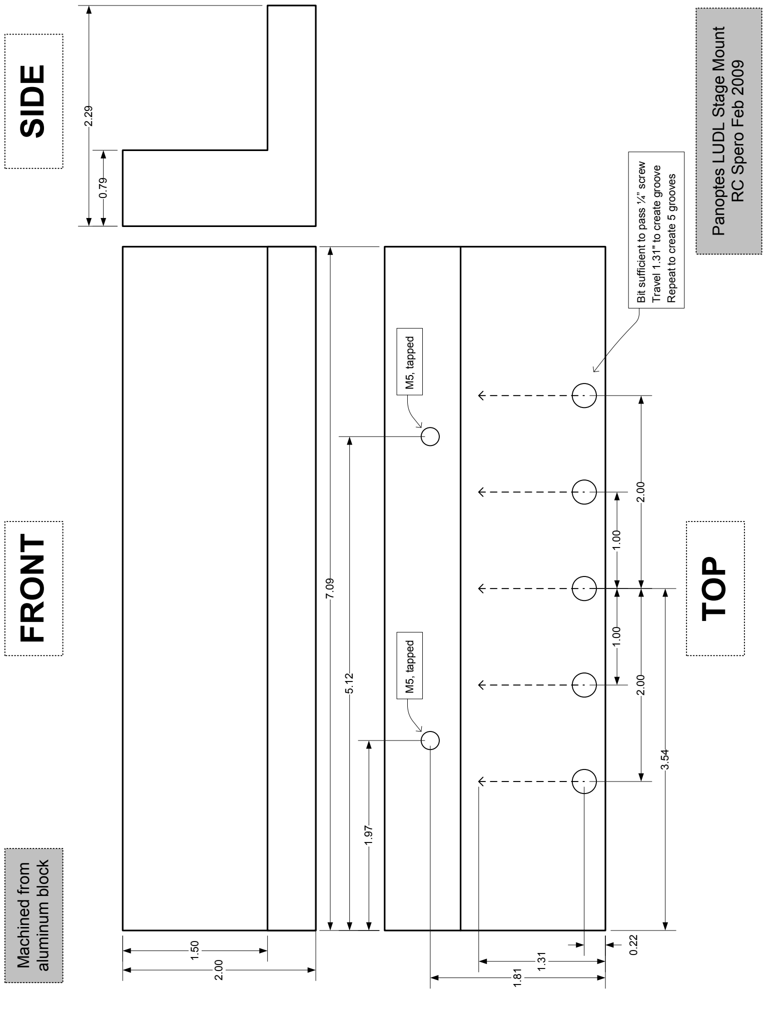

LUDL Mount.pdf

Figure C.2:

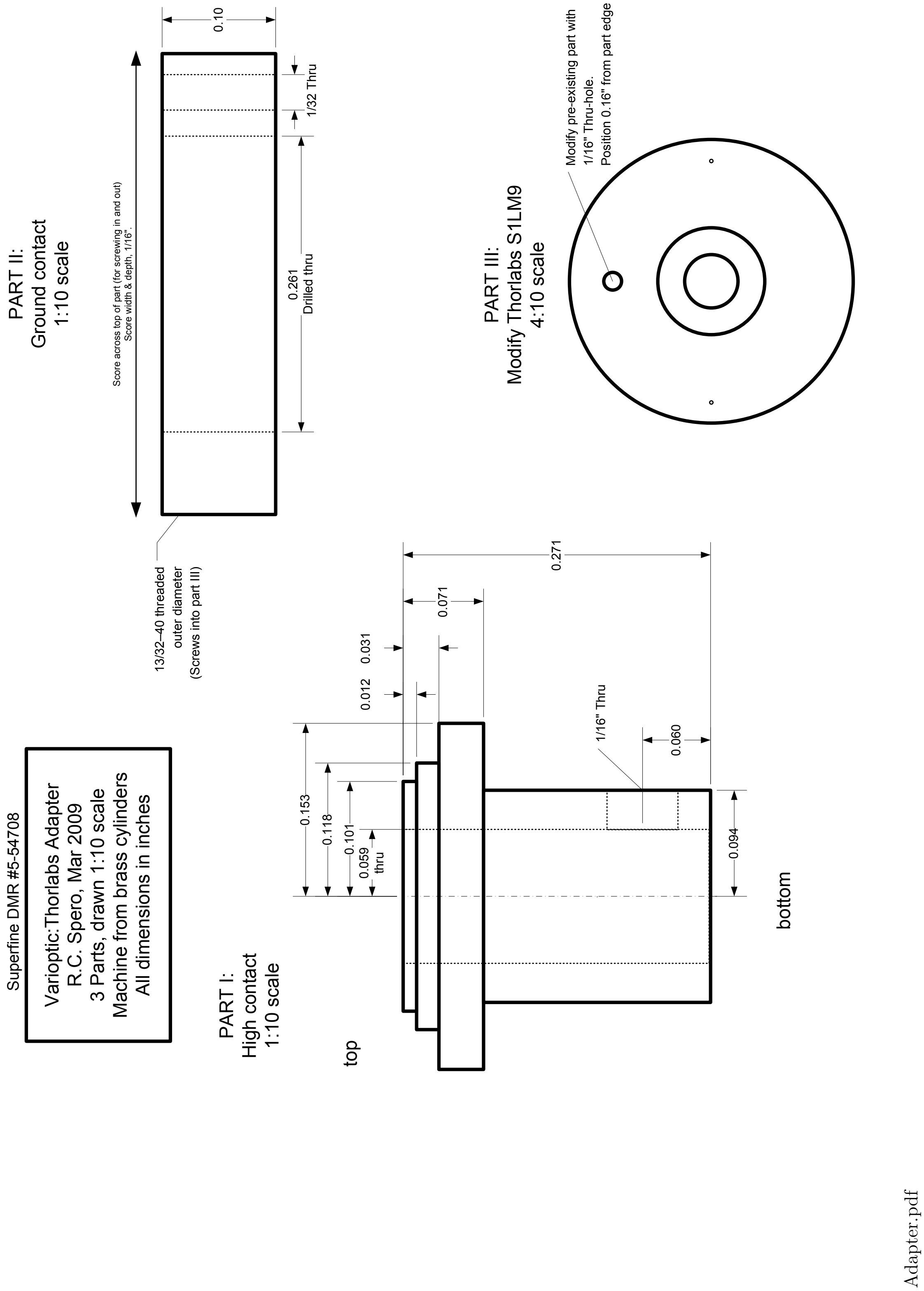
Superfine DMR #5-54708
Varioptic:Thorlabs Adapter
R.C. Spero, Mar 2009
3 Parts, drawn 1:10 scale
Machine from brass cylinders
All dimensions in inches
PART I:
High contact
1:10 scale
top
bottom
0.153
0.118
0.101
0.059
thru
0.012
0.031
0.071
0.271
1/16" Thru
0.060
0.094
PART II:
Ground contact
1:10 scale
Score across top of part (for screwing in and out)
Score width & depth, 1/16".
13/32–40 threaded
outer diameter
(Screws into part III)
0.10
1/32 Thru
0.261
Drilled thru
PART III:
Modify Thorlabs S1LM9
4:10 scale
Modify pre-existing part with
1/16" Thru-hole.
Position 0.16" from part edge
Adapter.pdf

Figure C.3:

Appendix D

Metadata Types

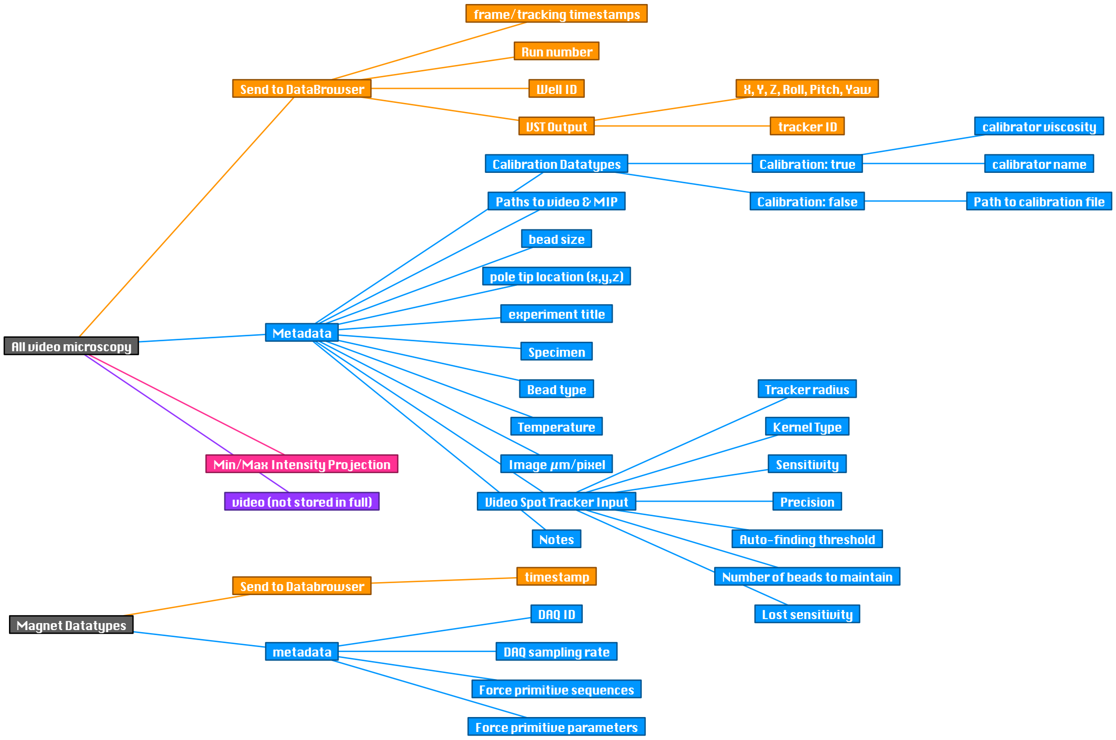

Figure D.1:

Bibliography

Ajjan, R., Lim, B. C. B., Standeven, K. F., Harrand, R., Dolling, S., Phoenix, F., Greaves, R., Abou-Saleh, R. H., Connell, S., Smith, D. A. M., Weisel, J. W., Grant, P. J., and Ariëns, R. A. S. (2008). Common variation in the c-terminal region of the fibrinogen beta-chain: effects on fibrin structure, fibrinolysis and clot rigidity. *Blood*, 111(2):643–50.

Ajjan, R. A., Standeven, K. F., Khanbhai, M., Phoenix, F., Gersh, K. C., Weisel, J. W., Kearney, M. T., Ariëns, R. A. S., and Grant, P. J. (2009). Effects of aspirin on clot structure and fibrinolysis using a novel in vitro cellular system. *Arterioscler Thromb Vasc Biol*, 29(5):712–7.

Astrom, B., Pipes, R., and Advani, S. (1992). On flow through aligned fiber beds and its application to composites processing. *Journal of Composite Materials*, 26(9):1351–1373. 10.1177/002199839202600907.

Bausch, A., Möller, W., and Sackmann, E. (1999). Measurement of local viscoelasticity and forces in living cells by magnetic tweezers. *Biophysical Journal*, 76(1):573–579.

Bausch, A., Ziemann, F., Boulbitch, A., Jacobson, K., and Sackmann, E. (1998). Local measurements of viscoelastic parameters of adherent cell surfaces by magnetic bead microrheometry. *BIOPHYSICAL JOURNAL*, 75(4):2038–2049.

Bear, J. (1988). Dynamics of fluids in porous media. page 764.

Blinc, A. and Francis, C. (1996). Transport processes in fibrinolysis and fibrinolytic therapy. *Thromb Haemostasis*, 76(4):481–491.

Blombäck, B., Carlsson, K., Fatah, K., Hessel, B., and Procyk, R. (1994). Fibrin in human plasma: gel architectures governed by rate and nature of fibrinogen activation. *Thrombosis research*, 75(5):521.

Blombäck, B., Carlsson, K., Hessel, B., Liljeborg, A., Procyk, R., and Aslund, N. (1989). Native fibrin gel networks observed by 3d microscopy, permeation and turbidity. *Biochimica et biophysica acta*, 997(1-2):96.

Blombäck, B. and Okada, M. (1982). Fibrin gel structure and clotting time. *Thrombosis research*, 25(1-2):51.

Bravo-Zanoguera, M., Massenbach, B., and Kellner, A. (1998). High-performance autofocus circuit for biological microscopy. *Review of Scientific ...*.

Bravo-Zanoguera, M. E., Laris, C. A., Nguyen, L. K., Oliva, M., and Price, J. H. (2007). Dynamic autofocus for continuous-scanning time-delay-and-integration image acquisition in automated microscopy. *Journal of biomedical optics*, 12(3):034011. Most recent continuous scanning autofocus paper.

Breedveld, V. and Pine, D. (2003). Microrheology as a tool for high-throughput screening. *Journal of Materials Science*, 38(22):4461–4470.

Brinkman, H. (1949). A calculation of the viscous force exerted by a flowing fluid on a dense swarm of particles. *Applied Scientific Research*.

Campbell, R. A., Overmyer, K. A., Bagnell, C. R., and Wolberg, A. S. (2008). Cellular procoagulant activity dictates clot structure and stability as a function of distance from the cell surface. *Arterioscler Thromb Vasc Biol*, 28(12):2247–54.

Carman, P. (1937). Fluid flow through granular beds. *Chemical Engineering Research and Design*.

Carr, M. E. J., Shen, L., and Hermans, J. (2004). Mass-length ratio of fibrin fibers from gel permeation and light scattering. *Biopolymers*.

Carr, M. J. and Hermans, J. (1978). Size and density of fibrin fibers from turbidity. *Macromolecules*.

Choi, C., Margraves, C., and Kihm, K. (2007). Examination of near-wall hindered brownian diffusion of nanoparticles: Experimental comparison to theories by brenner (1961) and goldman et al.(1967). *Physics of Fluids*, 19:103305.

Cicuta, P. and Donald, A. (2007). Microrheology: a review of the method and applications. *Soft Matter*, 3(12):1449–1455.

Clague, D. and Phillips, R. (1996). Hindered diffusion of spherical macromolecules through dilute fibrous media. *Physics of Fluids*, 8(7):1720–1731.

Collen, A., Smorenburg, S., Peters, E., and Lupu, F. (2000). Unfractionated and low molecular weight heparin affect fibrin structure and angiogenesis in vitro 1. *Cancer Research*.

Collet, J.-P., Lesty, C., Montalescot, G., and Weisel, J. W. (2003). Dynamic changes of fibrin architecture during fibrin formation and intrinsic fibrinolysis of fibrin-rich clots. *J Biol Chem*, 278(24):21331–5.

Cribb, J. (2010). Driven and thermal microparticle rheology of complex biopolymer systems. *Thesis*.

Crocker, J. C., Valentine, M. T., Weeks, E. R., Gisler, T., Kaplan, P. D., Yodh, A. G., and Weitz, D. A. (2000). Two-point microrheology of inhomogeneous soft materials. *Physical Review Letters*, 85(4):888–91.

Cussler, E. L. (1997). Diffusion: mass transfer in fluid systems. page 580.

Darcy, H. (1856). Les fontaines publiques de la ville de dijon: exposition et application des .... page 641.

Desseyn, J. L., Aubert, J. P., Porchet, N., and Laine, A. (2000). Evolution of the large secreted gel-forming mucins. *Mol Biol Evol*, 17(8):1175–84.

Diamond, S. L. (1999). Engineering design of optimal strategies for blood clot dissolution. *Annu Rev Biomed Eng*, 1:427–462.

Diamond, S. L. and Anand, S. (1993). Inner clot diffusion and permeation during fibrinolysis. *BIOPHYSICAL JOURNAL*, 65(6):2622–43.

Dobson, J. (2006). Magnetic micro-and nano-particle-based targeting for drug and gene delivery. *Nanomedicine*.

Dodge, J. T., Brown, B. G., Bolson, E. L., and Dodge, H. T. (1992). Lumen diameter of normal human coronary arteries. influence of age, sex, anatomic variation, and left ventricular hypertrophy or dilation. *Circulation*, 86(1):232–46.

Drummond, J. and Tahir, M. (1984). Laminar viscous flow through regular arrays of parallel solid cylinders. *International Journal of Multiphase Flow*.

Dullien, F. A. L. (1992). Porous media: fluid transport and pore structure. page 574.

Dunn, E. J., Ariëns, R. A. S., and Grant, P. J. (2005). The influence of type 2 diabetes on fibrin structure and function. *Diabetologia*, 48(6):1198–206.

Dürig, U., Cross, G., Despont, M., Drechsler, U., Häberle, W., Lutwyche, M., Rothuizen, H., Stutz, R., Widmer, R., Vettiger, P., Binnig, G., King, W., and Goodson, K. (2000). “millipede” – an afm data storage system at the frontier of nanotribology. *Tribology Letters*, 9(1):25–32.

Einstein, A. (1905). On the movement of small particles suspended in stationary liquids required by the molecular-kinetic theory of heat. *Annalen der Physik*.

Evans, P. A., Hawkins, K., Lawrence, M., Williams, R. L., Barrow, M. S., Thirumalai, N., and Williams, P. R. (2008). Rheometry and associated techniques for blood coagulation studies. *Med Eng Phys*, 30(6):671–9.

Fabry, B., Maksym, G., Butler, J., Glogauer, M., Navajas, D., and Fredberg, J. (2001). Scaling the microrheology of living cells. *Physical review letters*, 87(14):148102.

Fatah, K., Hamsten, A., Blombäck, B., and Blombäck, M. (1992). Fibrin gel network characteristics and coronary heart disease: relations to plasma fibrinogen .... *Thromb Haemostasis*.

Fatah, K., Silveira, A., Tornvall, P., and Karpe, F. (1996). Proneness to formation of tight and rigid fibrin gel structures in men with myocardial infarction at a young age. *Thromb Haemostasis*.

Ferry, J. D. (1980). Viscoelastic properties of polymers. page 641.

Fisher, J. K., Vicci, L., Cribb, J., O'Brien, E. T., Taylor, R. M., and Superfine, R. (2006). Magnetic force micromanipulation systems for the biological sciences. *Nano*, 1(3):191–205.

Fowler, J. and Hertel, K. (1940). Flow of a gas through porous media. *Journal of Applied Physics*.

Gelder, J. V., Nair, C., and Dhall, D. (1996). Colloid determination of fibrin network permeability. *Blood Coagulation and Fibrinolysis*.

Giannone, G. and Sheetz, M. P. (2006). Substrate rigidity and force define form through tyrosine phosphatase and kinase pathways. *Trends Cell Biol*, 16(4):213–23.

Giugliano, R., McCabe, C., Antman, E., and Cannon, C. (2001). Lower-dose heparin with fibrinolysis is associated with lower rates of intracranial hemorrhage. *American Heart Journal*.

Glückstad, J. and Palima, D. (2009). Generalized phase contrast: Applications in optics and photonics. page 315.

Guthold, M., Liu, W., Sparks, E. A., Jawerth, L. M., Peng, L., Falvo, M., Superfine, R., Hantgan, R. R., and Lord, S. T. (2007). A comparison of the mechanical and structural properties of fibrin fibers with other protein fibers. *Cell Biochem Biophys*, 49(3):165–81.

Hamamoto, S., Moldrup, P., Kawamoto, K., Komatsu, T., and Rolston, D. (2009). Unified measurement system for the gas dispersion coefficient, air permeability, and gas diffusion coefficient in variably saturated soil. *SOIL SCIENCE SOCIETY OF AMERICA JOURNAL*, 73(6):1921.

Happel, J. and Brenner, H. (1983). Low reynolds number hydrodynamics: with special applications to particulate media. page 553.

He, S., Bark, N., Wang, H., Svensson, J., and Blombäck, M. (2009). Effects of acetylsalicylic acid on increase of fibrin network porosity and the consequent upregulation of fibrinolysis. *Journal of Cardiovascular Pharmacology.*

Hendriks, B., Kuiper, S., As, M. V., Renders, C., and Tukker, T. (2005). Electrowetting-based variable-focus lens for miniature systems. *Optical Review*, 12(3):255–259.

Hubmayr, R., Shore, S., Fredberg, J., Planus, E., Panettieri, R., Moller, W., Heyder, J., and Wang, N. (1996). Pharmacological activation changes stiffness of cultured human airway smooth muscle cells. *Am J Physiol Cell Physiol*, 271(5):C1660–1668.

Jackson, G. and James, D. (1986). The permeability of fibrous porous media. *Canadian journal of chemical engineering.*

Jahnel, M., Waigh, T. A., and Lu, J. R. (2008). Thermal fluctuations of fibrin fibres at short time scales. *Soft Matter*, 4(7):1438.

Janmey, P., Amis, E., and Ferry, J. (1983). Rheology of fibrin clots. vi. stress relaxation, creep, and differential dynamic modulus of fine clots in large shearing deformations. *Journal of Rheology*, 27:135.

Johansson, L. and Lofroth, J. (1993). Diffusion and interaction in gels and solutions 4. hard-sphere brownian dynamics simulations. *JOURNAL OF CHEMICAL PHYSICS*, 98(9):7471–7479.

Johnson, E., Berk, D., Jain, R., and Deen, W. (1996). Hindered diffusion in agarose gels: test of effective medium model. *BIOPHYSICAL JOURNAL*, 70(2):1017–1023.

Kihm, K., Banerjee, A., Choi, C., and Takagi, T. (2004). Near-wall hindered brownian diffusion of nanoparticles examined by three-dimensional ratiometric total internal reflection fluorescence microscopy (3-d r-tirfm). *Exp Fluids*, 37(6):811–824.

Kimura, Y. (2009). Microrheology of soft matter. *Journal of the Physical Society of Japan*, 78(4):041005.

Kirschenbaum, L. A., Aziz, M., Astiz, M. E., Saha, D. C., and Rackow, E. C. (2000). Influence of rheologic changes and platelet-neutrophil interactions on cell filtration in sepsis. *Am J Respir Crit Care Med*, 161(5):1602–7.

Knaapen, P., Camici, P. G., Marques, K. M., Nijveldt, R., Bax, J. J., Westerhof, N., Götte, M. J. W., Jerosch-Herold, M., Schelbert, H. R., Lammertsma, A. A., and van Rossum, A. C. (2009). Coronary microvascular resistance: methods for its quantification in humans. *Basic Res Cardiol*, 104(5):485–98.

Lai, S., O'Hanlon, D., Harrold, S., Man, S., Wang, Y., Cone, R., and Hanes, J. (2007). Rapid transport of large polymeric nanoparticles in fresh undiluted human mucus. *Proceedings of the National Academy of Sciences*, 104(5):1482.

Lang, P., Yeow, K., Nichols, A., and Scheer, A. (2006). Cellular imaging in drug discovery. *Nature Reviews Drug Discovery*, 5(4):343–356.

Lee, J. and Ladd, A. (2005). Axial segregation of a settling suspension in a rotating cylinder. *Physical Review Letters*, 95(4):048001.

Lele, T., Sero, J., Matthews, B., Kumar, S., Xia, S., (true graphic)]Zavala, M. M., Polte, T., Overby, D., Wang, N., and Ingber, D. (2007). Methods in cell biology. Volume 83:441, 443–472.

Lenormand, G., Bursac, P., Butler, J., and Fredberg, J. (2007). Out-of-equilibrium dynamics in the cytoskeleton of the living cell. *Physical review letters*, 76(4):041901.

Levick, J. (1987). Flow through interstitium and other fibrous matrices. *Experimental Physiology*.

Llevadot, J. (2001). Bolus fibrinolytic therapy in acute myocardial infarction. *JAMA: The Journal of the American Medical Association*, 286(4):442–449.

Mason, T. and Weitz, D. (1995). Linear viscoelasticity of colloidal hard sphere suspensions near the glass transition. *Physical Review Letters*.

Meehan, T., Cribb, J., Skinner, K., and Superfine, R. (2010). Cylinder vs spheres: Biofluid shear thinning in nanoparticle transport. *Annals of Biomedical Engineering*.

Mickel, W., Münster, S., Jawerth, L. M., Vader, D. A., Weitz, D. A., Sheppard, A. P., Mecke, K., Fabry, B., and Schröder-Turk, G. E. (2008). Robust pore size analysis of filamentous networks from three-dimensional confocal microscopy. *BIOPHYSICAL JOURNAL*, 95(12):6072–80.

Neuman, K. and Block, S. (2004). Optical trapping. *Review of Scientific Instruments*.

Neumann, B., Walter, T., Hériché, J.-K., Bulkescher, J., Erfle, H., Conrad, C., Rogers, P., Poser, I., Held, M., Liebel, U., Cetin, C., Sieckmann, F., Pau, G., Kabbe, R., Wünsche, A., Satagopam, V., Schmitz, M. H. A., Chapuis, C., Gerlich, D. W., Schneider, R., Eils, R., Huber, W., Peters, J.-M., Hyman, A. A., Durbin, R., Pepperkok, R., and Ellenberg, J. (2010). Phenotypic profiling of the human genome by time-lapse microscopy reveals cell division genes. *Nature*, 464(7289):721–7.

Ogston, A., Preston, B., and Wells, J. (1973). On the transport of compact particles through solutions of chain-polymers. *Proceedings of the Royal Society of London. Series A*.

Pedersen, J., Boschetti, F., and Swartz, M. (2007). Effects of extracellular fiber architecture on cell membrane shear stress in a 3d fibrous matrix. *Journal of biomechanics*, 40(7):1484–1492.

Phillips, R. (2000). A hydrodynamic model for hindered diffusion of proteins and micelles in hydrogels. *BIOPHYSICAL JOURNAL*.

Phillips, R., Deen, W., and Brady, J. (1989). Hindered transport of spherical macromolecules in fibrous membranes and gels. *AIChE Journal*.

Plank, C., Schillinger, U., Scherer, F., Bergemann, C., Rémy, J.-S., Krötz, F., Anton, M., Lausier, J., and Rosenecker, J. (2003). The magnetofection method: using magnetic force to enhance gene delivery. *Biol Chem*, 384(5):737–47.

Pluen, A., Netti, P. A., Jain, R. K., and Berk, D. A. (1999). Diffusion of macromolecules in agarose gels: comparison of linear and globular configurations. *BIOPHYSICAL JOURNAL*, 77(1):542–52.

Price, J. H. and Gough, D. A. (1994). Comparison of phase-contrast and fluorescence digital autofocus for scanning microscopy. *Cytometry*, 16(4):283–97.

Ramanujan, S., Pluen, A., Mckee, T. D., Brown, E. B., Boucher, Y., and Jain, R. K. (2008). Diffusion and convection in collagen gels: Implications for transport in the tumor interstitium. *BIOPHYSICAL JOURNAL*, 83(3):1650–1660.

Rand, P., Lacombe, E., Hunt, H., and Austin, W. (1964). Viscosity of normal human blood under normothermic and hypothermic conditions. *journal of applied physiology*.

Roberts, W., Kramer, O., Rosser, R., Nestler, F., and Ferry, J. (1974). Rheology of fibrin clots. i. dynamic viscoelastic properties and fluid permeation. *Biophysical chemistry*, 1(3):152.

Rodriguez-Merchan, E. C., Goddard, N. J., and Lee, C. A. (2000). Musculoskeletal aspects of haemophilia. page 236.

Rogers, S. L. and Rogers, G. C. (2008). Culture of drosophila s2 cells and their use for rnai-mediated loss-of-function studies and immunofluorescence microscopy. *Nat Protoc*, 3(4):606–11.

Rose, C. (2001). Giants, monsters, and dragons: an encyclopedia of folklore, legend, and myth. page 428.

Rubinstein, M. and Colby, R. H. (2003). Polymer physics. page 440.

Ryan, E., Mockros, L., Weisel, J., and Lorand, L. (1999). Structural origins of fibrin clot rheology. *BIOPHYSICAL JOURNAL*.

Sangani, A. and Acrivos, A. (1982). Slow flow past periodic arrays of cylinders with application to heat transfer. *International Journal of Multiphase Flow*.

Saxena, S., Jain, P., and Shukla, J. (2003). Preparation of two component fibrin glue and its clinical evaluation in skin grafts and flaps. *Indian Journal of Plastic Surgery*.

Shen, F., Hodgson, L., Rabinovich, A., Pertz, O., Hahn, K., and Price, J. H. (2006). Functional proteometrics for cell migration. *Cytometry A*, 69(7):563–72.

Simpson, K., Selfors, L., Bui, J., Reynolds, A., Leake, D., Khvorova, A., and Brugge, J. (2008). Identification of genes that regulate epithelial cell migration using an sirna screening approach. *Nat Cell Biol*.

Smith, S. A. and Morrissey, J. H. (2008). Polyphosphate enhances fibrin clot structure. *Blood*, 112(7):2810–6.

Spero, R., Vicci, L., Cribb, J., Bober, D., Swaminathan, V., O'Brien, E., Rogers, S., and Superfine, R. (2008). High throughput system for magnetic manipulation of cells, polymers, and biomaterials. *Review of Scientific Instruments*, 79:083707.

Srebnik, S. and Sheintuch, M. (2009). Diffusion enhancement in composites of nanotubes and porous structures. *MOLECULAR SIMULATION*, 35(1):100–108.

Szymczyk, A. and Fievet, P. (2005). Investigating transport properties of nanofiltration membranes by means of a steric, electric and dielectric exclusion model. *Journal of membrane science*, 252(1-2):77–88.

Thornton, D., Rousseau, K., and McGuckin, M. (2008). Structure and function of the polymeric mucins in airways mucus. *Annual Reviews*.

Valentine, M., Perlman, Z., Gardel, M., Shin, J., Matsudaira, P., Mitchison, T., and Weitz, D. (2004). Colloid surface chemistry critically affects multiple particle tracking measurements of biomaterials. *BIOPHYSICAL JOURNAL*, 86(6):4004–4014.

Varga, V. S., Ficsor, L., Kamarás, V., Jónás, V., Virág, T., Tulassay, Z., and Molnár, B. (2009). Automated multichannel fluorescent whole slide imaging and its application for cytometry. *Cytometry A*, 75(12):1020–30.

Varin, R., Mirshahi, S., Mirshahi, P., Kierzek, G., Sebaoun, D., Mishal, Z., Vannier, J.-P., Borg, J. Y., Simoneau, G., Soria, C., and Soria, J. (2007). Clot structure modification by fondaparinux and consequence on fibrinolysis: a new mechanism of antithrombotic activity. *Thromb Haemostasis*, 97(1):27–31.

Veklich, Y., Francis, C. W., White, J., and Weisel, J. W. (1998). Structural studies of fibrinolysis by electron microscopy. *Blood*, 92(12):4721–9.

Waigh, T. (2005). Microrheology of complex fluids. *Reports on Progress in Physics*, 68(3):685–742.

Wang, B., Anthony, S. M., Bae, S. C., and Granick, S. (2009). Anomalous yet brownian. *Proc Natl Acad Sci USA*, 106(36):15160–4.

Weisel, J. (2004). The mechanical properties of fibrin for basic scientists and clinicians. *Biophysical chemistry*.

Weisel, J. (2005). Fibrinogen and fibrin. *Advances in protein chemistry*.

WHO (2004). The global burden of disease. pages 1–160.

Wicky, S. (2009). Acute deep vein thrombosis and thrombolysis. *Techniques in Vascular and Interventional Radiology*, 12(2):148–153.

Wijmans, J. and Baker, R. (1995). The solution-diffusion model: a review. *Journal of membrane science*, 107(1-2):1–21.

Williams, J. C., Mark, L. A., and Eichholtz, S. (1998). Partition and permeation of dextran in polyacrylamide gel. *BIOPHYSICAL JOURNAL*, 75(1):493–502.

Wolberg, A. S., Allen, G. A., Monroe, D. M., Hedner, U., Roberts, H. R., and Hoffman, M. (2005). High dose factor viia improves clot structure and stability in a model of haemophilia b. *Br J Haematol*, 131(5):645–55.

Wolberg, A. S. and Campbell, R. A. (2008). Thrombin generation, fibrin clot formation and hemostasis. *Transfus Apher Sci*, 38(1):15–23.

Wolberg, A. S., Gabriel, D. A., and Hoffman, M. (2002). Analyzing fibrin clot structure using a microplate reader. *Blood Coagul Fibrinolysis*, 13(6):533–9.

Wong, I., Gardel, M., Reichman, D., Weeks, E., Valentine, M., Bausch, A., and Weitz, D. (2004). Anomalous diffusion probes microstructure dynamics of entangled f-actin networks. *Physical Review Letters*, 92(17):178101.

Zamani, A. and Maini, B. (2009). Flow of dispersed particles through porous media–deep bed filtration. *JOURNAL OF PETROLEUM SCIENCE AND ENGINEERING*.

Zhong, J., Wen, W., and Jones, A. (2003). Enhancement of diffusion in a high-permeability polymer by the addition of . . . . *Macromolecules*.

Ziemann, F., Rädler, J., and Sackmann, E. (1994). Local measurements of viscoelastic moduli of entangled actin networks using an oscillating magnetic bead micro-rheometer. *BIOPHYSICAL JOURNAL*, 66(6):2210–2216.